Special Heusler Compounds for Spintronic Applications

Dissertation
zur Erlangung des Grades
"Doktor der Naturwissenschaften"
am Fachbereich Chemie, Pharmazie und Geowissenschaften
der Johannes Gutenberg-Universität Mainz

vorgelegt von
Benjamin Balke
geboren in Lemgo

Mainz, 2007

Für Ruth

Dekan: Prof. Dr. Peter Langguth

Tag der mündlichen Prüfung: 14. Januar 2008

Die vorliegende Arbeit wurde in der Zeit von Juli 2004 bis Juli 2007 am Institut für Anorganische und Analytische Chemie im Fachbereich Chemie, Pharmazie und Geowissenschaften der Johannes Gutenberg-Universität, Mainz unter der Leitung von Frau Prof. Dr. Claudia Felser angefertigt.

Mainz, Juli 2007

Hiermit versichere ich, dass ich die vorliegende Dissertation selbstständig verfasst und keine anderen als die angegebenen Hilfsmittel benutzt habe. Alle der Literatur entnommenen Stellen sind als solche gekennzeichnet.

Mainz, Juli 2007

Contents

1 Introduction

Spintronics is a multidisciplinary field and a new research area for solid state scientists. New materials must be found for satisfying the different types of demands. The search for ferromagnetic semiconductors and stable half-metallic ferromagnets with Curie temperatures higher than room temperature is still a challenge for solid state chemists. A general understanding of how structures are related to properties is a necessary prerequisite for material design. This work presents some parts of the materials research for the field of spin electronics and the related area magnetoelectronics. Spin electronic, or short spintronic, covers the field of devices that make use not only of the charge of the electrons but also of their spin. Magnetoelectronic comprises the devices making use of ferromagnetic materials. For example, the probably most oftenly used magnetoelectronic device is nowadays the read-write head of hard-discs in computers. Spintronics includes additionally the semiconductor based devices. The spin-valve transistor is thought to be most promising for future applications and quantum computing. The borderline between the two disciplines is flexible. In particular, the magnetic tunnelling phenomena are the connecting link between magnetoelectronics and spintronics.

1.1 Magnetoelectronics

For the last 40 years, the semiconductor industry has been able to continually shrink the size of electronic components on silicon chips, packing ever more performance into computers. The fundamental physical limits of the current technology have now been reached, namely the sizes of the structures. Within the last decade, a new approach appears to be capable of revolutionising the market for electronic devices. Some predicted advantages of the new technologies arising from spintronics are the non-volatile storage of data, increased data processing speeds, high storage density and low energy consumption.

In order to make use of the full potential of spintronics, new magnetic materials, magnetic semiconductors and so-called half-metallic ferromagnets (HFM) are needed. Half-metallic ferromagnets seem to be a suitable class of materials which meet all requirements of spintronics. One reason is their exceptional electronic structure: They behave like metals for majority electrons and like semiconductors for minority electrons. CrO_2, Manganites and Heusler compounds are half-metallic ferromagnets. Ferromagnetic semiconductors with Curie temperatures higher than room temperature are not known up to now.

In the following, a short explanation of the basic spintronic and magnetoelectronic effects will be given to introduce the reader in this interesting field and to make him the demand on the materials transparent.

1.1.1 Spin Current

All currently available spin-based devices are memory devices that use the spin to store information. Just as conventional electronic devices require charge currents, spin-based electronic (spintronic) devices such as transistors require spin currents [1].Unfortunately, it is very difficult to generate and transport spin currents. Sharma gave an easily understandable explanation of what is meant by a spin current [2]. Consider an electron current that flows through a wire and contains only electrons of one spin, say spin-up polarised electrons. Add to this a similar current in which all electrons are polarised spin-down that flows in the opposite direction. The result is a current of spins only; there is no net particle transfer across any cross section of the wire (see Figure 1.1).

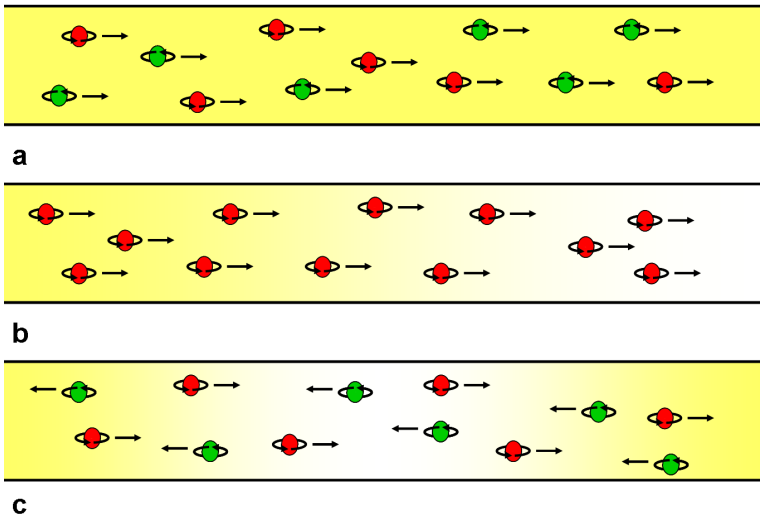

Figure 1.1: Current through a wire: the upper part shows a regular charge current (charges of both spin move), the middle part a single spin and charge current (charges of a single spin move), and the lower part a pure spin current (no charges but only spins move.

A spin current (Figure 1.1 (c)) differs from a charge current (Figure 1.1 (a)) in some important ways. For a spin current, the ohmic resistivity is suppressed as no electrons and thus no charges are moved. In addition, the spin current is invariant under time reversal: if a clock ran backwards, the spin current would still flow in the same direction. Furthermore, the spin current is associated with a spin flow that is a vector quantity (angular momentum). This allows quantum information to be sent across semiconducting structures, just as in quantum optics using polarised light states.
A current that does not only use the electron charge but also the spin as transport property will need new types of materials that are completely spin polarised. In 1983, de Groot defined a fully spin polarised compound as a half-metallic ferromagnet [3]. Half-metallic ferromagnets (HMFs) are expected to have a gap at ϵ_F for the spin density in one direction (e.g., down) while the opposite spin density is metallic (see Figure 1.2).

This allows a completely polarised current [3].

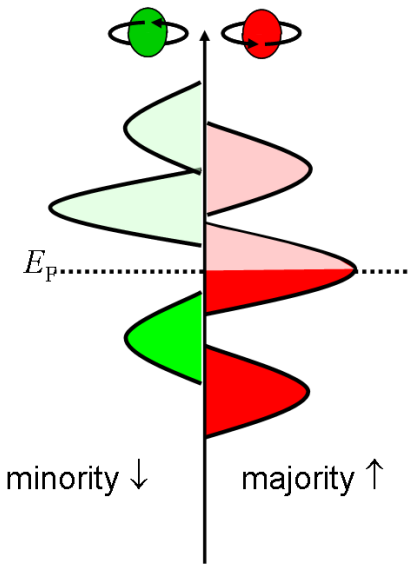

Figure 1.2: Schematic density of states of a half-metallic ferromagnet. In this case, the gap appears in the minority states (left).

1.1.2 Magnetoresistance

A basic effect in spintronics is the magnetoresistance (MR), which is generally defined as the ratio of the resistance of a material without a magnetic field to the resistance of a material in a magnetic field. A large change in the electrical resistivity in response to an applied magnetic field is of technological relevance for the development of magnetic switching devices and magnetic memories. The search for new systems is important because improvements are still needed for applications.

There are two definitions used in the literature. The magnetoresistance, which can not exceed 100%, is defined as

$$\frac{\Delta R}{R} = \frac{R\uparrow\uparrow - R\uparrow\downarrow}{R\uparrow\downarrow} \tag{1.1}$$

$R\uparrow\downarrow$ and $R\uparrow\uparrow$ are the resistivities for the antiparallel and the parallel alignment of the magnetisation in two adjacent magnetic layers (see Figure 1.3). The optimistic definition of magnetoresistance is sometimes useful for comparing small values: it becomes infinite for fully polarised electrodes and is given by

$$\frac{\Delta R}{R} = \frac{R\uparrow\uparrow - R\uparrow\downarrow}{R\uparrow\uparrow} \tag{1.2}$$

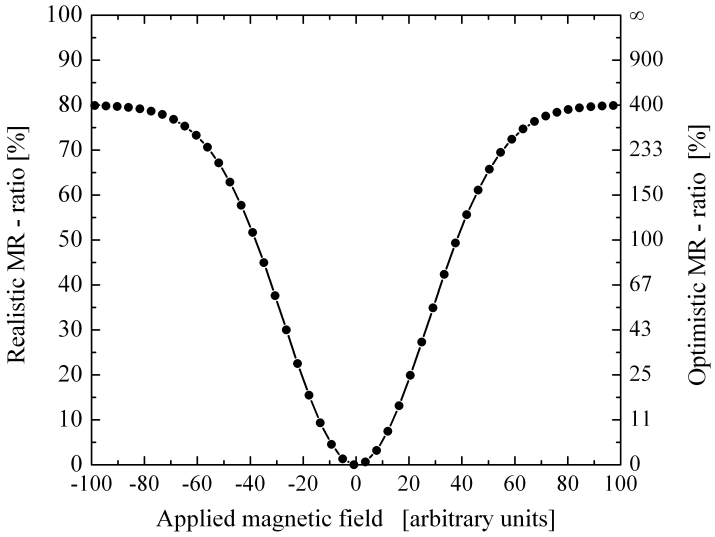

Figure 1.3: Schematic magnetoresistance of a multilayer device, with different scaling for the MR ratio $\Delta R/R$, realistic and optimistic.

Anisotropic magnetoresistance (AMR), the first magnetoresistive effect reported, was discovered in 1857 by W. Thomson (Lord Kelvin)[4]. This anisotropic effect is small ($\approx 3\%$), and depends on the Fermi surface of the material. From the time of its discovery until 1988, AMR remained the most important contribution to the magnetoresistance of ferromagnets. The AMR effect has been applied in making magnetic sensors and readout heads for magnetic disks.

Giant Magnetoresistance (GMR)

A breakthrough occurred in 1988 when the Grünberg [5] and Fert [6] groups each independently discovered the so-called giant magnetoresistance (GMR), which is ten times larger than the anisotropic effect. Similar to the high temperature superconductor area, many research activities have started in this field. The Giant magnetoresistive effect is observed in multilayer systems consisting of interleaved magnetic and non-magnetic layers, and is used in magnetic sensors and in nearly every hard disc read head. Figure 1.4 shows an example of such a multilayer Fe–Cr–Fe system [6].

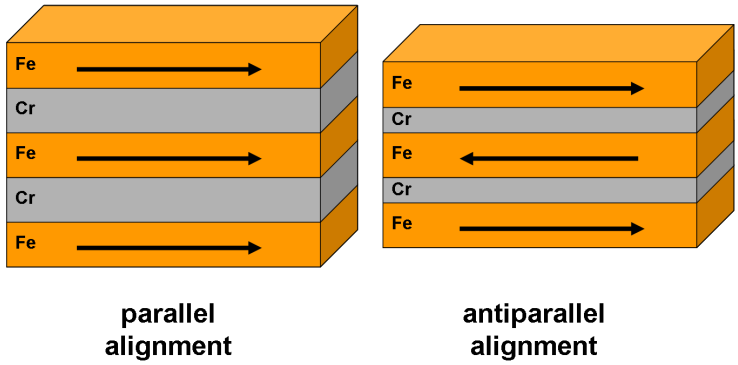

Figure 1.4: A multilayer system Fe–Cr–Fe with ferromagnetic (left) and with antiferromagnetic (right) exchange coupling between the iron layers.

By applying a magnetic field, the resistivity of some samples can be suppressed by orders of magnitude. Depending on the thickness of the Cr interlayers, the interlayer exchange coupling between the Fe layers changes from ferromagnetic (parallel) to antiferromagnetic (antiparallel). Measurements of the electrical resistance show that where the exchange is antiferromagnetic, the resistance is high and can be changed by applying large magnetic fields. The resistivity drops as the configuration of the magnetisation in neighbouring Fe layers goes from antiparallel to parallel. When an electrical field is applied, the spin oriented electrons of the Fe layers accelerate until they encounter a scattering centre. Provided that the interlayer thickness is less than the coherence length, the electron arrives at the interface of the neighbouring ferromagnetic layer still carrying its initial spin orientation. In the case of ferromagnetically coupled Fe layers, the arriving electron has a high probability of entering the adjacent layer because its spin orientation matches that of the layer. If the exchange coupling is antiferromagnetic, the electrons suffer strong scattering at the interface, resulting in a high resistance. The magnetoresistance ratio of a Fe–Cr–Fe multilayer system reaches 79% at 4 K and small fields, and is still 20% at room temperature for a sample with a 9 Å thick Cr layer [6].

The read head or the magnetic sensor device consists of an artificial multilayer thin film material consisting of alternate ferromagnetic and non-magnetic metals. IBM introduced these devices in 1997 and the market for them is now one billion dollars per year [7]. Figure 1.5 shows a typical geometry for GMR measurements. The current can either be perpendicular to the interfaces (CPP, current-perpendicular-to-plane) or can be parallel to the interfaces (CIP, current-in-plane). The GMR was originally discovered in a CIP configuration; however the CPP configuration shows an even larger effect. A spin valve consists of two ferromagnetic layers sandwiching a thin non-magnetic metal layer. One of the magnetic layers is "pinned", insensitive to moderate magnetic fields; the second is "free" and its magnetisation can be changed by applying small magnetic fields.

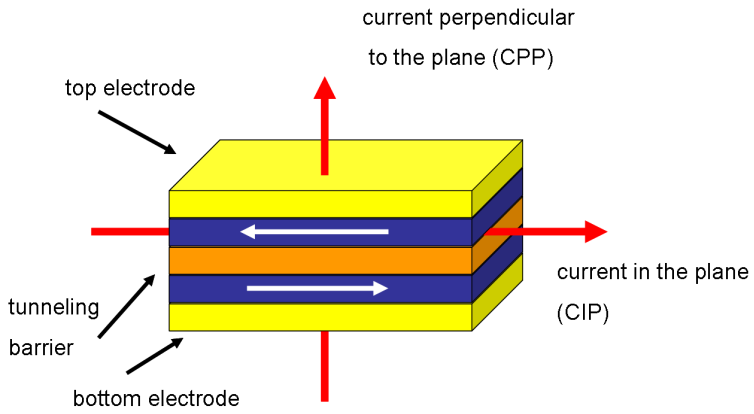

Figure 1.5: Typical multilayer geometry for the measurement of giant magnetoresistance. The arrows indicate the current-in-plane (horizontal) and current-perpendicular-to-plane (vertical) geometries.

Colossal Magnetoresistance (CMR)

In 1993, von Helmolt *et al.* [8], and soon followed by Jin *et al.* [9], discovered an even larger magnetoresistive effect in mixed valence manganese perovskites, the so-called colossal magnetoresistance (CMR). In general, the resistivity of a ferromagnetic bulk material is reduced at low temperatures (deviating from the resistivity curve of a non-magnetic metal). Near the Curie temperature, the resistivity increases due to the scattering of the conduction electrons by spin disorder. Scattering by spin fluctuations is usually a small effect and, in transition metals, resistance changes of only a few percent occur near the ferromagnetic ordering temperature. The magnitude of the CMR is not explained as being due to scattering of conduction electrons; it is the result of a metal to insulator transition in the manganites that depends on temperature. The most famous system, described in detail in Reference [10], is $LaMnO_3$.

Whereas the effect is large in manganites, both the sensitivity (MR ratio in small fields) and the temperature dependence (only a small effect at room temperature) are not satisfactory for applications.

Tunnel Magnetoresistance (TMR)

The use of half-metallic electrodes in spin valves or in magnetic tunnel junctions (MTJs) results in a pronounced increase in the magnetoresistance. As sketched in Figure 1.6, a tunnel junction is a device in which the pinned magnetic layer and the free magnetic layer are separated by a very thin insulating layer, commonly aluminium oxide. The effect is based on the tunnelling of electrons through the insulating barrier and is called the tunnel magnetoresistance (TMR) (for details see the review [11]). Early pioneering investigations on the problem of spin dependent tunnelling were performed in the 1970s by P. M. Tedrow and R. Meservey [12], by M. Jullire [13], and by S. Maekawa and U. Gfvert [14]. Twenty years later, however, the first large magnetoresistance in mag-

netic tunnel junctions was observed at room temperature by J. S. Moodera [15] and T. Miyazaki [16]. Following the Jullire model [13], the tunnelling magnetoresistance (TMR) ratio of a junction is related to the spin polarisation P of the electrodes according to:

$$\frac{\Delta R}{R_{TMR}} = \frac{2P_1P_2}{1+P_1P_2} \tag{1.3}$$

where P_1 is the polarisation of one electrode and P_2 is the polarisation of the second electrode. The spin polarisation P is defined by

$$P = \frac{N\uparrow - N\downarrow}{N\uparrow + N\downarrow} \tag{1.4}$$

$N\uparrow$ and $N\downarrow$ are the densities of the majority and the minority electrons at the Fermi energy.

The Jullire model is a simple approximation for the tunnel effect. However, the model is commonly used to estimate the spin polarisation of the electrodes. High spin polarisation is required for high TMR ratios. The largest ratio of 1,800% was measured by Fert's group in a tunnel junction with a manganite electrode. This corresponds to an electrode spin polarisation of at least 95%, but unfortunately only at 4 K [17]. Significant progress has recently been achieved with crystalline MgO barriers exhibiting very high TMR ratios of more than 400% at room temperature [18, 19, 20].

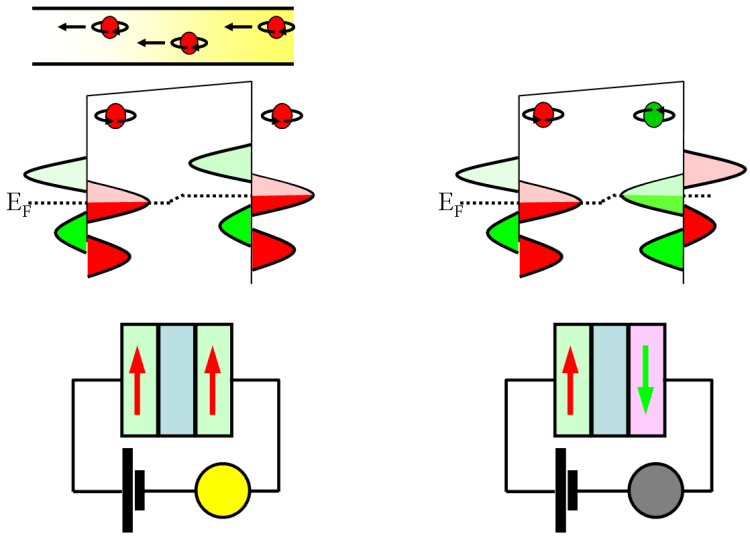

Figure 1.6: A typical tunnel magnetoresistance device (TMR).

Powder Magnetoresistance (PMR)

The powder magnetoresistance experiment is a variant of the tunnel magnetoresistance (TMR) experiment with point contacts between the grains of a powder of a half-metallic material. The experiment is rather easy to perform and a simple way for the material

scientist to determine half-metallicity [21]. In the experiment, a powder of a supposedly half-metallic material is compressed into a compact pellet. The magnetic orientation of the grains will be statistically random in the non-magnetised state and the resistance will be high. By applying an external magnetic field, the magnetic domains of the grains will be orientated along the direction of that field. This will lead to a decrease of the resistance. As shown in Figure 1.7, a typical butterfly magnetoresistance curve is traced out on cycling the field, with a maximum resistance at the coercive field. The contacts between the powder grains are typically a mixture of tunnel barriers and ballistic point contacts, and the resistance is determined by the most conductive paths through the maze. It is helpful to dilute the conducting magnetic powder with a non-conducting, non-ferromagnetic powder of similar particle size [21]. This extrinsic grain boundary magnetoresistance is observed in conducting oxides like CrO_2, pyrochlore $Tl_2Mn_2O_7$, magnetite Fe_3O_4, ordered double perovskites Sr_2FeMoO_6 [22] and $La_{2-2x}Sr_{1+2x}Mn_2O_7$ [23]. In addition, a PMR ratio of 30% was found in powder samples of $Co_2Cr_{0.6}Fe_{0.4}Al$ in low magnetic fields [24, 25].

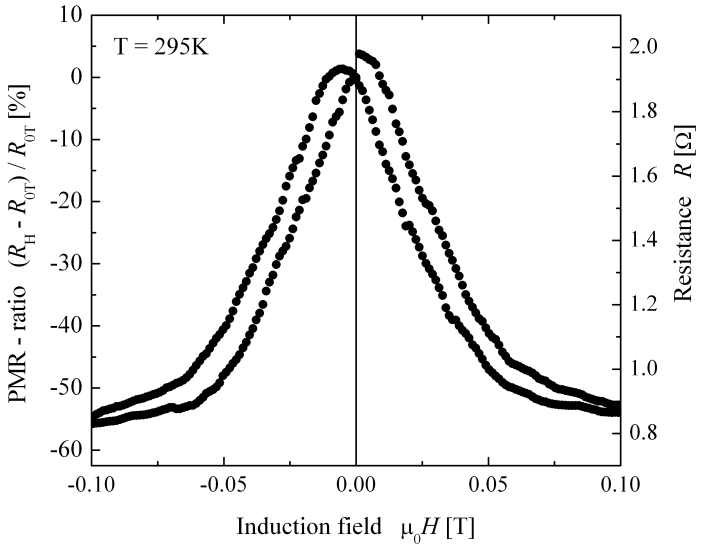

Figure 1.7: Powder magnetoresistance (PMR) of $Co_2Cr_{0.6}Fe_{0.4}Al$ + 15% Al_2O_3, measured at room temperature.

Granular Magnetoresistance

Granular magnetoresistance is observed in granular magnetic materials and is related to GMR [26]. A granular magnetoresistance material consists of a metallic matrix (Cu or Ag) with magnetic inclusions. This effect is also sometimes observed in ordered alloys with magnetic superstructures [27, 28]. In these systems, the magneto-resistance curve looks like the MR curve of a multi-layer GMR system; even in large fields however, no saturation can be achieved. The reason for this behaviour is the inhomogeneous particle size distribution of the ferromagnetic inclusions. For large particles (¿ 5 nm),

the magnetisation is easily changed, whereas it is difficult to change for small particles.

1.1.3 Spin Injection

Another possible spintronics application is based on the spin injection of a spin polarised current into a semiconductor system [29]. When electrons are injected from a ferromagnet into a non-magnetic material, they can retain their spin polarisation over a certain distance. The requirements for this to occur are successful spin injection, spin transport within the semiconductor with a spin diffusion length of many microns, spin lifetimes of more than 100 ns, and spin detection [30]. The best suited material would be a ferromagnetic semiconductor with a Curie temperature far above room temperature. Semiconductors doped with small amounts of magnetic impurities such as manganese exhibit room temperature ferromagnetism (dilute magnetic semiconductor, DMS). These materials exhibit both semiconducting and magnetic properties and are of high potential use in spintronics devices. Major progress in this field was achieved in particular by the H. Ohno [31, 32] and D. D. Awshalom [29] groups, both of which demonstrated that electrons can retain their spin polarisation over unexpectedly long times and distances [29, 33, 34]. Important devices based on DMS are spin polarised light emission diodes (spin-LED) and spin polarised field effect transistors (spin-FET) [30]. A spin FET is an FET in which the source and the drain are ferromagnetic materials that are intended for injecting and detecting spin polarised currents. The conduction depends on the spin orientation and can be controlled by the gate voltage. As shown in Figure 1.8, in a spin-LED, the spin polarised electrons are injected into a semiconductor. If the carriers retain their spin polarisation, the emitted light is circularly polarised.

1.2 Magnetic Materials

Since brief explanations of the different important effects in spintronics have been given above, the focus will now be on the materials themselves: half-metallic ferromagnets and ferromagnetic semiconductors.

1.2.1 Regular Ferromagnetic Metals

Most ferromagnetic materials are metals. The ferromagnetic transition metals are iron, cobalt, and nickel. All of these three elements exhibit high Curie temperatures (Fe: T_C = 1039 K; Co: T_C = 1394 K; Ni: T_C = 633 K); they are not however half-metallic. The rare earth metals Gd (T_C = 288 K), Dy, and Tb, as well as a large number of metallic alloys and compounds, also exhibit ferromagnetism. In general, half-metallic ferromagnets are rare because of their particular electronic structure.

To have only minority or majority electrons at (ϵ_F), it is necessary to reorder the $3d$ and $4s$ bands of the ferromagnetic transition element. As sketched in Figure 1.2, the DOS at EF must have a real gap in one spin direction to achieve half-metallic ferromagnetism. The occurrence of band gaps in the overall band structure may therefore be a prerequisite for a ferromagnetic half-metal.

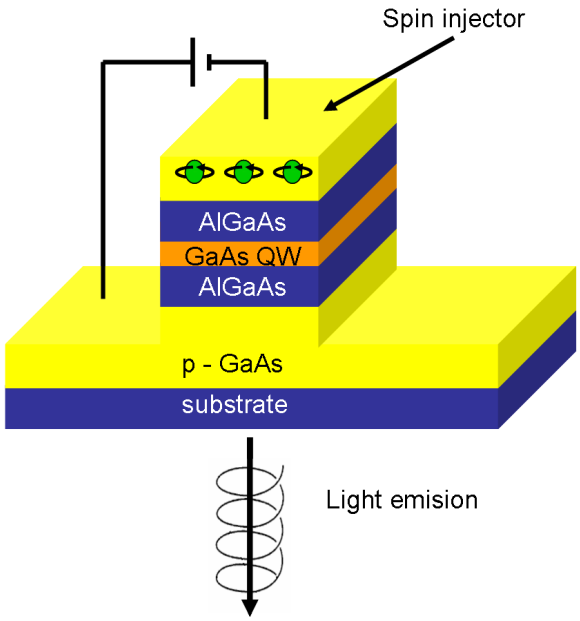

Figure 1.8: Schematic cross section of a spin polarised light emitting diode (spin-LED) based on spin injection. The device is constructed from a *AlGaAs–GaAs* quantum well multilayer system

These band gaps can be achieved by pushing the bottom of the $4s$ band up above (ϵ_F), or by depressing the Fermi level below the bottom of the $4s$ band (ionic half-metals). Alternatively, a hybridisation gap may be introduced at (ϵ_F) for one spin direction. Covalent intermetallic compounds exhibit hybridisation gaps in their electronic structure. In any case, it is necessary to go from a pure element to an alloy or compound; therefore, all half-metallic ferromagnets contain more than one element. Some ferromagnets are stoichiometric compounds, others are solid solutions. It should be noted that there is no relation between a half-metal and a semi-metal. Semi-metals, of which graphite or bismuth are textbook examples, have small and equal numbers of electrons and holes (0.01 per atom) that are due to a fortuitously small overlap between the valence and conduction bands. This leads to an anisotropy in the conductivity. On the other hand, a half-metal has a real gap in one spin direction and is metallic in the other.

1.2.2 The Slater-Pauling Rule

Slater [35] and Pauling [36] independently found that the magnetic moments m of the $3d$ elements and their binary alloys can be described by the mean number of valence electrons (n_V) per atom. Depending upon $m(n_V)$, the Slater-Pauling rule distinguishes between two regions. The first region with high valence electron concentration (close packed structures: fcc, hcp) is the range of itinerant magnetism ($n_V \geq 8$), and the second region (bcc) is the region of localised moments ($n_V \leq 8$). Fe is a borderline example of

the latter. As described by Kbler [37], a plot of m versus the average number of valence electrons $m(n_V)$ is called the Slater-Pauling curve. Figure 1.9 shows the Slater-Pauling curve for the transition metals and some of their alloys. The Heusler compound Co_2MnSi and the $C1_b$ compound NiMnSb are included for comparison.

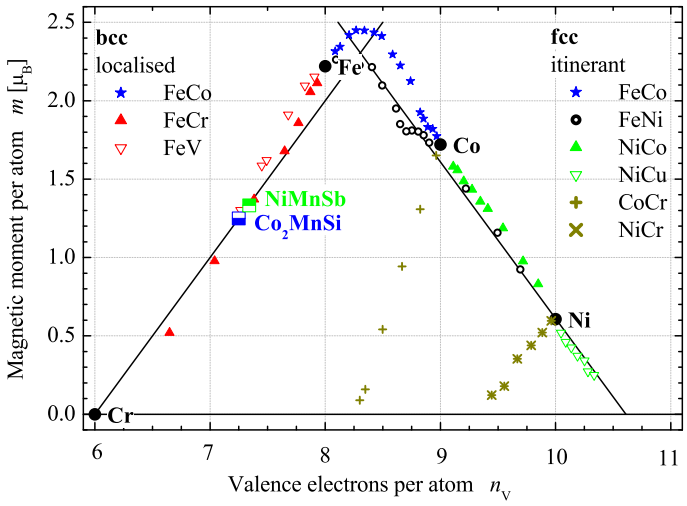

Figure 1.9: Slater-Pauling curve for 3*d* transition metals and their alloys. NiMnSb and Co_2MnSi are given for comparison.

From the definition of the magnetic moment ($m = n\uparrow$ - $n\downarrow$, in multiples of the Bohr magneton μ_B), and the number of valence electrons ($n_V = n\uparrow + n\downarrow$), it is easy to show that the Slater-Pauling rule for the part of the curve for describing itinerant magnetism is given by

$$m = 2n\uparrow - n_V = 2(n_d\uparrow + n_{sp}\uparrow) - n_V \tag{1.5}$$

For filled majority *d* bands (as e.g. in Nickel), one has $n_d\uparrow = 5$ and thus

$$m = 10 - n_V + 2n_{sp}\uparrow \tag{1.6}$$

Slater and Pauling found that the number of occupied sp states is approximately $n_{sp} = 2\ n_{sp}\uparrow \approx 0.6$, since the electrons are not polarised. This explains the itinerant part of the curve and, in particular, that the magnetic moment of Ni is $\approx 0.6\ \mu_B$. It appears that some alloys do not follow the expected curve (Co-Cr and Ni-Cr in Figure 1.9). It was shown by Malozemov *et al.* that the high valence concentration part of the curve can be generalised in such a way that the alloys under question still follow a similar rule [38], which also holds for alloys between transition metals and metalloids (Al, Si, Ga, etc.). For all of these cases, the magnetic moment is proportional to the average magnetic valence z_M and given by $m = z_M + 2\ n_{sp}\uparrow$ (for details, see Reference [37]).

In the context of this thesis, the localised part of the Slater-Pauling curve, where iron and the bcc-type alloys are found, is of greater interest. From the definitions given above, an alternative form for the magnetic moment in multiples of μ_B is easily found to be

$$m = n_V - 2n \downarrow \tag{1.7}$$

The minimum in the minority spin density constrains the number of occupied electrons in the minority d bands to be approximately 3. By neglecting the *sp* electrons, it is found that the magnetic moment in the localised part of the Slater-Pauling curve is approximately described by the rule

$$m \approx n_V - 6 \tag{1.8}$$

which indicates that the average magnetic moment per atom is simply given by subtracting 6 from the average number of valence electrons per atom.

Half-metallic ferromagnets are expected to exhibit a real gap in the minority density of states where the Fermi energy is pinned. The existence of this gap requires that the number of occupied minority states be integer. That is, the above given Slater-Pauling rule is strictly followed when $m_{HMF} = n_V$ - 6 [37, 39] In general, this rule may lead to non-integer numbers of the magnetic moment due to the averaging over the number of valence electrons. For well-ordered compounds, it may be more practical to use the total number N_V of valence electrons in the unit cell.

For $C1_b$ compounds with 3 atoms in the unit cell, the following valence electron rule is expected:

$$m_{C1_b} = N_V - 18 \tag{1.9}$$

In particular, the rule for Heusler compounds with 4 atoms in the unit cell is found to be

$$m_{L2_1} = N_V - 24 \tag{1.10}$$

where the magnetic moment in the unit cell is expressed in μ_B. N_V is the accumulated number of valence electrons in the unit cell.

Exceptions to those rules are found for conventional semiconductors or for zinc blende based half-metals that follow an 8 valence electron rule. Other than Heusler-like alloys however, such materials may not fulfil the symmetry requirements that are required of Slater-Pauling alloys.

It should be noted that complete disorder in the $L2_1$ Heusler compounds results in an $A2$ (bcc-type) structure. Thus, the ferromagnetic Heusler compounds are expected to behave like the alloys found on the localised part of the Slater-Pauling curve. This distinguishes the Heusler compounds from most of the other compounds reported upon in this thesis, the other compounds also perhaps having a linear dependence between the magnetic moments and the valence electron concentration but with a different symmetry of the crystalline structure.

1.2.3 Half-Metallic Ferromagnets

The dependence of spin polarisation as a function of temperature in half-metallic ferromagnets was recently investigated theoretically [40, 41] and experimentally [42]. The magnetisation of the usual ferromagnets is reduced at ambient temperature, supposed they have a high Curie temperature. In the same way, the minority density of states (DOS) f half-metallic ferromagnets becomes non-zero at finite temperatures due to spin-rotation. A reduction of the spin polarisation may also be caused by crystal imperfections, interfaces, and surfaces. These results are important for room temperature applications using half-metallic ferromagnets: very high Curie temperatures and stable structures are a prerequisite for a high magneto-resistance.

Covalent Half-Metals

A possible way of achieving a band gap in the overall band structure is by covalence. Silicon is a semiconductor because of the strong covalent bonding interaction between the silicon atoms. Silicon crystallises in the diamond structure in which one silicon atom is surrounded by four other silicon atoms. Each silicon atom is sp^3 hybridised with four fully occupied bonding bands, and a band gap separating the unoccupied antibonding bands from the bonding bands. Like GaAs, other semiconductors crystallise in the zinc blende structure. ZnS exhibits the same number of valence electrons (8 valence electrons or, if the ten d electrons are included, 18 valence electrons) and, in a first approximation, a similar band structure. All these semiconductors exhibit band gaps in their overall band structures. In Si, the energy gap (identical for both spins) is responsible for the semiconducting behaviour of the material. In half-metals, the gap in only one spin channel is just as important because it produces the blocking effect that prevents a spin flip since no spin-down states are available within the gap.

$C1_b$ compounds

The $C1_b$ compound NiMnSb was one of the early materials being predicted to be a HMF by electronic structure calculations [43]. Two alternative structural descriptions of the $C1_b$ structure (space group $F\,\bar{4}3m$, sometimes falsely called half-Heusler) are possible. The common description is that the $C1_b$ compounds of composition XYZ (X, Y=transition metals, Z=main-group element) consist of three interpenetrating fcc lattices. From the viewpoint of electronic structures, the most appropriate description of these compounds is a zinc-blende YZ lattice stuffed with X atoms (see Figure 1.10).

In 1984, Kübler found that the Slater-Pauling rule is useful for describing the magnetic properties of the $C1_b$ and $L2_1$ compounds [44]. Jung *et al* [45] recognized that many XYZ compounds can be thought of as comprising X^{n+} ions stuffed in a zinc-blende-type $[YZ]^{n-}$ sublattice, where the number of valence electrons associated with the $[YZ]^{n-}$ sublattice is 18 ($d^{10} + s^2 + p^6$). Such closed-shell 18-electron compounds are nonmagnetic and semiconducting [46, 47]. The prototype for a non ferromagnetic compound is CoTiSb.

Many attempts have been made to prepare semiconducting compounds that also have ferromagnetic properties. Mn-doped GaAs [48] was considered to be a suitable compound, but its Curie temperature is only about 150 K [49] and thus still far away from being suitable for application in electronic devices (see Reference [50] for a recent review). Other materials, like Mn-doped GaN (T_C = 228 to 370 K) [51], V-doped TiO_2 ($T_C \approx 400$ K) [52], p-(Ga,Ni)N ($T_C \approx 300$ K) [53], or Co-doped ZnO ($T_C > 300$ K) [54] come only close to room temperature or need special treatments (see References).

On the other hand, most of the magnetic and half-metallic $C1_b$ compounds contain manganese or a rare earth metal. This is not accidental because, as described by Kübler *et al*[55], the properties of the manganese ions in the Y position of the Heusler compounds must be taken into account. These manganese ions, which have an approximate Mn^{3+} configuration, have a highly localized moment in the order of 3 to 4 μ_B. The rare earth ions (RE) in $C1_b$ compounds (for example, RENiSb or REAuSn) also exhibit a charge of +3 and a magnetic moment corresponding to localized f states [56].

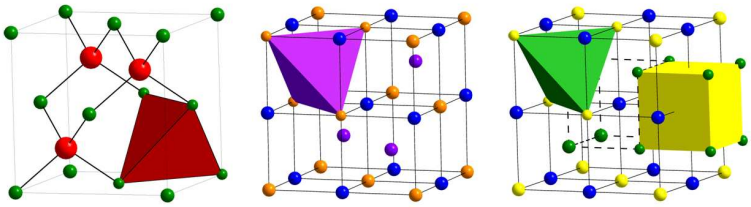

Figure 1.10: Structure of $B3$ (zinc-blende), $C1_b$ and $L2_1$ (Heusler) compounds.

$L2_1$ compounds

Heusler compounds - discovered in 1901 - have the chemical formula X_2YZ, with X and Y being transition metals and Z being a main group element [57, 58]. Ordered Heusler compounds crystallise in the $L2_1$ structure ($Fm\bar{3}m$) [59]. The additional X atom fills the remaining tetrahedral vacancy in the XYZ structure. However, this changes the symmetry of the crystal structure. The two X atoms occupy sites with T_d symmetry and the Y and Z atoms occupy sites with O_h symmetry.

In addition to the localised magnetic moment at the Y atom on the cubic site, the X atoms on the tetrahedral sites interact with each other, and this may lead to an additional itinerant magnetic interaction between the X atoms. In the case of 4 atoms per unit cell, as in Heusler compounds, 24 (six times the number of atoms) must be subtracted from the accumulated number of valence electrons N_V (s, d electrons for the transition metals and s, p electrons for the main group element) to find the magnetic moment per unit cell, i. e. $M_{HMF} = N_V$ - 24. This rule is strictly followed for half-metallic ferromagnets [60, 61]. Whereas $C1_b$ compounds mostly exhibit only a localised moment at the Y site, the magnetic interactions in Heusler compounds are more complicated because the additional X atom results in an additional magnetic interaction. For this reason, the variety of $L2_1$ compounds is much larger than the number of $C1_b$ compounds, and the possibility of achieving half-metallic ferromagnetism is greater as well.

Table 1.1: The classification of half-metals after Coey *et al.* [21]

Type	Density of states	Conductivity	↑ Electrons at ϵ_F	↓ Electrons at ϵ_F
IA	half-metal	metallic	itinerant	none
IB	half-metal	metallic	none	itinerant
IIA	half-metal	nonmetallic	localised	none
IIB	half-metal	nonmetallic	none	localised
IIIA	metal	metallic	itinerant	localised
IIIB	metal	metallic	localised	itinerant
IVA	semi-metal	metallic	itinerant	localised
IVB	semi-metal	metallic	localised	itinerant
VA	semiconductor	semiconducting	few, itinerant	none
VB	semiconductor	semiconducting	none	few, itinerant

1.2.4 Classification of Half-Metals

Coey has proposed a broad classification scheme for half-metallic ferromagnets [21]. The classification scheme and examples are given in Table 1.1.

A material exhibiting metallic conductivity and a spin moment with an integral number of Bohr magnetons per unit cell at $T = 0$ is the best indicator for a type I or type II half-metal. However, the integer spin moment criterion for stoichiometric compounds, or an extension of the criterion to include solid solutions, is a necessary but not a sufficient condition for half-metallicity.

Type IA half-metals are metallic for majority electrons but semiconducting for minority electrons, whereas the opposite is true for the type IB half-metals. Half-metallic oxides, in which the 4s states are pushed above ϵ_F, are of type IA when there are less than five d electrons, but half-metallic oxides with more than five d electrons are of type IB. Half-metallic Heusler alloys, with heavy p elements like Sb, tend to have the $3d$ levels depressed below the $4s$ band edge by hybridisation.

Examples of type IA half-metals are CrO_2 and Mn_2VAl, and examples of type IB half-metals are Sr_2FeMoO_6 and Co_2MnSi. In a second class of half-metals, which is designated as type II, the carriers at the Fermi level are in a band that is sufficiently narrow for them to be localised. Magnetite, a magnetic mineral, is a half-metal with a spin gap in the majority density of states, and localised states in the minority band [62]; it is a type IIB half-metal. A third class of half-metals, known as "transport half-metals", has localised majority states and delocalised minority states, or vice versa [63].

The density of states at ϵ_F does not vanish for either of the sub-bands, but the carriers in one band have a much larger effective mass than those in the other band. In regards to electronic transport properties, only one type of carrier contributes significantly to conduction. $(La_{0.7}Sr_{0.3})MnO_3$ is a type IIIA half-metal, with both spin states present at ϵ_F, but with very different mobilities for the two spins. $Tl_2Mn_2O_7$, a ferromagnetic pyrochlore structure oxide, has an unusual semi-metallic band structure, with approximately 0.01 electrons and holes per formula [64]. There are a small number of heavy

holes at the top of a narrow majority band of Mn(t_{2g}) character, and an equal number of minority electrons in a broad band of mixed Tl($6s$), O($2p$) and Mn($3d$) character, making this a type IVA half-metal. Diluted magnetic semiconductors (DMS) are included in the table as type V half-metals.

1.3 Investigations of this thesis

This work emphasizes the potential of Heusler compounds in a wide range of spintronic applications. Using electronic structure calculations it is possible to design compounds for specific applications. Examples for GMR and TMR applications, for spin injection into semiconductors, and for spin torque transfer applications will be shown. Chapter 5 reports about the investigation of new half-metallic compounds where the Fermi energy is tuned in the middle of the gap to result in more stable compounds. The bulk properties of the quaternary Heusler alloy $Co_2Mn_{1-x}Fe_xSi$ with the Fe concentration ranging from $x = 0$ to 1 will be reported. All samples, which were prepared by arc melting, exhibit $L2_1$ long range order over the complete range of Fe concentration. Structural and magnetic properties of $Co_2Mn_{1-x}Fe_xSi$ Heusler alloys were investigated by means of X-ray diffraction, high and low temperature magnetometry, Mößbauer spectroscopy, and differential scanning calorimetry. The electronic structure was explored by means of high energy photo emission spectroscopy at about 8 keV photon energy. This ensures true bulk sensitivity of the measurements. The magnetization of the Fe doped Heusler alloys is in agreement with the values of the magnetic moments expected for a Slater-Pauling like behavior of half-metallic ferromagnets. The experimental findings are discussed on the hand of self-consistent calculations of the electronic and magnetic structure. To achieve good agreement with experiment, the calculations indicate that on-site electron-electron correlation must be taken into account, even at low Fe concentration. The investigation focuses on searching for the quaternary compound where the half-metallic behavior is stable against outside influences. Overall, the results suggest that the best candidate may be found at an iron concentration of about 50%.

In $Co_2Mn_{1-x}Fe_xSi$ the transition metal carrying the localized moment is exchanged. This might lead to unexpected effects on the magnetic properties if the samples are not completely homogeneous. Therefore Chapter 6 reports about the optimization of the Heusler compounds for GMR and TMR applications. The structural and magnetic properties of the quaternary Heusler alloy $Co_2FeAl_{1-x}Si_x$ with varying Si concentration will be reported. The structure of the $Co_2FeAl_{1-x}Si_x$ solid solution was investigated by means of X-ray diffraction and differential scanning calorimetry. It is found that the alloys exhibit the $L2_1$ structure for $x \geq 0.4$. Depending on the Si concentration x, a structural phase transition is found at temperatures between 1000 K and 1200 K. The transition temperature decreases with increasing Si content x. The magnetic properties were studied using low temperature magnetometry. For $x \geq 0.4$, the magnetization of the compounds is in agreement with a Slater-Pauling like behavior and with the values obtained from ab-initio calculations. For $x \leq 0.4$ enlarged magnetic moments are found

due to disorder. From the combination of experimental (better order for high Si content) and theoretical findings (robust gap at $x \approx 0.5 \pm 0.25$) it is concluded that a compound with an intermediate Si concentration close to $x = 0.5 \ldots 0.7$ would be best suited for spintronic applications, especially for GMR and TMR applications.

Chapter 7 reports about a detailed investigation of diluted magnetic semiconductors with a very low lattice mismatch among each other. This makes this samples interesting for spintronics applications like Spin-LEDs or other spin injection devices. One could prepare thin film devices including these materials and it should be possible to grow them epitaxially with clean and smooth interfaces. If depositing layer by layer one can use the Co-planes to merge the different materials without any interface at all.

The diluted magnetic semiconductors were prepared by substituting titanium in the semiconducting compound CoTiSb by other 3d transition elements. The structural, electronic, and magnetic properties of the pure and doped materials were investigated. It was found that substitution of up to 10% Ti by Fe, Mn, Cr, and V does not affect the crystalline structure and the lattice mismatch is less than 0.5% among each other. Self consistent calculations of the electronic structure predict some of the materials to be half-metallic ferromagnets. The Curie temperature of the Fe substituted alloy is far above room temperature (> 700 K), thus making that material a serious candidate for future electronic applications, in particular for magnetoelectronics and spintronics.

Chapter 8 reports about a detailed investigation of the theoretically predicted half-metallic completely compensated-ferrimagnet Mn_3Ga as a suitable material for spin torque transfer applications. The electronic, magnetic, and structural properties of the tetragonal DO_{22} phase of Mn_3Ga were investigated. It has been found that the material is hard magnetic with an energy product of $H_c \times B_r = 52.5$ kJm^{-3} and an average saturation magnetization of about 0.25 Bohr magnetons per atom at 5 K. The saturation magnetization indicates a ferrimagnetic order with partially compensating moments at the Mn atoms on crystallographically different sites. The Curie temperature is above 730 K where the onset of decomposition is observed. The electronic structure calculations indicate a nearly half-metallic ferrimagnetic order with 88% spin polarization at the Fermi energy.

2 List of Publications

1. B. Balke, G. H. Fecher, H. C. Kandpal, C. Felser, K. Kobayashi, E. Ikenaga, J.-J. Kim, and S. Ueda
Properties of the quaternary half-metal-type Heusler alloy $Co_2Mn_{1-x}Fe_xSi$
Phys. Rev. B 74 (2006) 104405.

2. K. Kroth, B. Balke, G. H. Fecher, V. Ksenofontov, C. Felser, and H.-J. Lin
Diluted magnetic semiconductors with high Curie temperature based on $C1_b$ compounds: $CoTi_{1-x}Fe_xSb$
Appl. Phys. Lett. 89 (2006) 202509.

3. H. Schneider, G. Jakob, M. Kallmayer, H. J. Elmers, M. Cinchetti, B. Balke, S. Wurmehl, C. Felser, M. Aeschlimann, and H. Adrian
Epitaxial film growth and magnetic properties of Co_2FeSi
Phys. Rev. B 74 (2006) 174426.

4. M. Kallmayer, H. J. Elmers, B. Balke, S. Wurmehl, F. Emmerling, G. H. Fecher, and C. Felser
Magnetic properties of $Co_2Mn_{1-x}Fe_xSi$ Heusler alloys
J. Phys. D: Appl. Phys. 39 (2006) 786 - 792.

5. B. Balke, J. Winterlik, G. H. Fecher, and C. Felser
Mn_3Ga, a compensated ferrimagnet with high Curie temperature and low magnetic moment for spin torque transfer applications.
Appl. Phys. Lett. 90 (2007) 152504.

6. B. Balke, S. Wurmehl, G. H. Fecher, C. Felser, M. C. M. Alves, F. Bernardi, and J. Morais
Structural characterization of the Co_2FeZ (Z=Al, Si, Ga, and Ge) Heusler compounds by x-ray diffraction and extended x-ray absorption fine structure spectroscopy
Appl. Phys. Lett. 90 (2007) 172501.

7. B. Balke, G. H. Fecher, and C. Felser
Structural and magnetic properties of $Co_2FeAl_{1-x}Si_x$
Appl. Phys. Lett. 90 (2007) 242503.

8. B. Balke, H. C. Kandpal, G. H. Fecher, and C. Felser
The half-metallic ferromagnet $Co_2Mn_{0.5}Fe_{0.5}Si$
J. Magn. Magn. Mat. 310 (2007) 1823 - 1825.

9. C. Felser, G. H. Fecher, and B. Balke
Spintronics: A Challenge for Materials Science and Solid-State Chemistry
Angew. Chem. Int. Ed. 46 (2007) 668 - 699.

10. C. Felser, G. H. Fecher, and B. Balke
Spintronik: eine Herausforderung fr Materialwissenschaften und Festkrperchemie
Angew. Chem. 119 (2007) 680.

11. S. Wurmehl, J. T. Kohlhepp, H. Swagten, B. Koopmans, M. Wojcik, B. Balke, C.G.F. Blum, V. Ksenofontov, G. H. Fecher, and C. Felser
Probing the random distribution of Mn an Fe in half-metallic $Co_2Mn_{1-x}Fe_xSi$ Heusler alloys
Appl. Phys. Lett. 90 (2007) accepted.

12. M. Kallmayer, A. Conca, M. Jourdan, H. Schneider, G. Jakob, B. Balke, A. Gloskovskii, and H. J. Elmers
Correlation of local disorder and electronic properties in the Heusler alloy $Co_2Cr_{0.6}Fe_{0.4}Si$
J. Phys. D: Appl. Phys. 40 (2007) 1539 - 1543.

13. M. Kallmayer, H. Schneider, G. Jakob, H. J. Elmers, B. Balke, and S. Cramm
Interface magnetization of ultrathin epitaxial $Co_2FeSi(110)/Al_2O_3$ films
J. Phys. D: Appl. Phys. 40 (2007) 1552 - 1557.

14. A. Gloskovskii, J. Barth, B. Balke, G. H. Fecher, C. Felser, F. Kronast, R. Ovsyannikov, H. Dürr, W. Eberhard, and G. Schönhense
A spatially resolved investigation of the local, micro-magnetic domain structure of single and polycrystalline Co_2FeSi
J. Phys. D: Appl. Phys. 40 (2007) 1570 - 1575.

15. G. H. Fecher, B. Balke, S. Ouardi, C. Felser, G. Schönhense, E. Ikenaga, J.-J. Kim, S. Ueda, and K. Kobayashi
High energy, high resolution photoelectron spectroscopy of $Co_2Mn_{1-x}Fe_xSi$
J. Phys. D: Appl. Phys. 40 (2007) 1576 - 1581.

16. G. H. Fecher, A. Gloskowskii, K. Kroth, J. Barth, B. Balke, C. Felser, F. Schäfers, M. Mertin, W. Eberhardt, S. Mähl, and O. Schaff
Bulk sensitive photo emission spectroscopy of $C1_b$ compounds
J. Electron Spectrosc. Relat. Phenom. 156-158 (2007) 97.

3 Calculational Details

The self-consistent electronic structure calculations were carried out using the scalar-relativistic full potential linearized augmented plane wave method (FLAPW) as provided by Wien2k [65]. The exchange-correlation functional was taken within the generalized gradient approximation (GGA) in the parameterization of Perdew *et al* [66].

The calculation of mixed random alloys is not straight forward in the FLAPW as is used here. To verify that ordered compounds could be used instead of random alloys, the full relativistic Korringa-Kohn-Rostocker (KKR) method with the coherent potential approximation (CPA) was employed [67]. The exchange-correlation functional was parameterized by using the plain GGA. No significant differences in the integrated properties, such as the density of states or the magnetic moments, were found between the methods.

For the case of Co_2FeSi, it has recently been demonstrated that LSDA or GGA schemes are not sufficient for describing the electronic structure correctly. Significant improvement was found, however, when the LDA+U method [39, 68] was used and this computational scheme was used here as well. LDA+U, as described by Anisimov *et al* [69], adds an orbital dependent electron-electron correlation, which is not included in the plain LSDA or GGA schemes. It should be mentioned that the $+U$ was used in the FLAPW scheme with the GGA rather than the LSDA parameterization of the exchange-correlation functional. No significant differences were observed using either of these parameterizations.

In case of the dilluted magnetic semiconductors the calculations were performed using one of the most common parameterizations of the exchange-correlation functional as given by Vosco, Wilk, and Nussair [70, 71, 72]. Additionally, the generalized gradient approximation (GGA) was used in the form given by Perdew *et al* [73]. The CPA tolerance was set to 10^{-4} and the energy convergence criterion to 10^{-5}. f states were included in the basis of all atoms. 578 irreducible k-points based on a $22 \times 22 \times 22$ mesh were used for integration. The density of states was calculated for the same number of k-points from the Greens function by adding a small imaginary part of 2 mRy to the energy. For smaller values, the band gaps may become better visible, however, at the same time the DOS becomes much more noisy.

4 Experimental Details

All polycristalline samples were prepared by arc melting of stoichiometric amounts of the constituents in an argon atmosphere at 10^{-4} mbar. Care was taken to avoid oxygen contamination. This was ensured by evaporating Ti inside of the vacuum chamber before melting the compound as well as by additional purifying of the process gas. The polycrystalline ingots were then annealed in an evacuated quartz tube.

The cristallographic structure was investigated by X-ray powder diffraction (XRD) using excitation by Mo K_α (Bruker, AXS D8) in reflection geometry or Cu K_α radiation (Bruker, D500) in transmission geometry in a $\theta - \theta$ scanning mode.

Flat disks were cut from the ingots and polished for spectroscopic investigations of bulk samples. For powder investigations, the remainder was crushed by hand using a mortar. It should be noted that using a steel ball mill results in a strong perturbation of the crystalline structure.

X-ray photo emission (ESCA) was used to verify the composition and to check the cleanliness of the samples. After removal of the native oxide from the polished surfaces by Ar^+ ion bombardment, no impurities were detected with ESCA. The samples were afterwards capped in-situ by a 2 nm layer of Au at room temperature to prevent oxidation of the samples during transport in air.

Magneto-structural investigations were carried out using Mößbauer spectroscopy in transmission geometry using a constant acceleration spectrometer. For excitation, a ^{57}Co(Rh) source with a line width of 0.105 mm/s (5 neV) was used. The spectra from powder samples were taken at 290 K.

The magnetic properties were investigated by a super conducting quantum interference device (SQUID, Quantum Design MPMS-XL-5) using nearly punctual pieces of approximately 5 mg to 10 mg of the sample.

Differential scanning calorimetry (DSC) measurements (NETZCH, STA 429) were performed to detect phase transitions below the melting point. In particular, attempts were made to find the Curie temperature (T_C), but this turned out to be too high to be determined directly by the SQUID, which is limited to 775 K even in the high temperature mode.

The electrical transport property measurements were done with flat discs ($2\times3\times5$ mm) of the annealed samples. The electrical resistivity was measured using a Quantum Design Physical Properties Measurement System (PPMS) by the four contact method with silver contacts.

The electronic structure of the Co_2 based Heusler compounds was explored by means of high energy X-ray photo emission spectroscopy. The measurements were performed at the beamline BL47XU of the synchrotron SPring 8 (Hyogo, Japan). The photons are produced by means of a 140-pole in vacuum undulator and are further monochromized by a double double-crystal monochromator. The first monochromator uses Si(111) crystals and the second a Si(111) channel-cut crystal with 444 reflections (for 8 keV X-rays). The

energy of the photo emitted electrons is analyzed using a Gammadata - Scienta R 4000-12kV electron spectrometer. The ultimate resolution of the set up (monochromator plus analyzer at 50 eV pass energy using a 200 μm slit) is 83.5 meV at 7935.099 eV photon energy. For the here reported experiments, a photon energy of 7939.15 eV has been employed. Under the present experimental conditions an overall resolution of 250 meV has been reached. All values concerning the resolution are determined from the Fermi-edge of an Au sample. Due to the low cross-section of the valence states from the investigated compounds, the spectra had to be taken with $E_{pass} = 200$ eV and a 500 μm slit for a good signal to noise ratio. The polycrystalline samples have been fractured in-situ before taking the spectra to remove the native oxide layer. Core-level spectra have been taken to check the cleanliness of the samples. No traces of impurities were found. The valence band spectra shown in section 5.7 were collected over 2-4 h at about 100 mA electron current in the storage ring in the top-up mode. All measurements have been taken at a sample temperature of 20 K.

The temperaure dependent XRD measurements were performed at the X-ray powder diffraction (XPD) beamline at the bending magnet D10 at the Brazilian Synchrotron Light Laboratory (LNLS). For details about the characteristics of the beamline see, e.g. Reference [74]. The temperature was varied from 20 to 300 K using a closed cycle cryostat and resistive heating. The excitation energy was set to $h\nu = 7050$ eV corresponding to a photon wavelength $\lambda = 1.75886$ Å.

Details of the electronic structure of CoTiSb and $CoTi_{0.9}Fe_{0.1}Sb$ have been explored experimentally by means of photo emission spectroscopy. The hard X-ray photo emission spectroscopy (HAXPES) measurements have been performed at the KMC-1 beamline of the storage ring BESSY (Berlin, Germany). The photons are produced by means of a bending magnet. The photon beam is focused by a toroidal mirror and monochromatized by a double-crystal monochromator. In the present work the Si(111) crystal pairs were used which can be employed for photon energies up to ≈ 15 keV with a starting energy of 1.997 keV. The spot size of the beam is (0.4×0.6) mm^2 at the sample. The complete beamline is operated under oil-free UHV conditions ($< 5 \times 10^{-8}$ mbar at last valve). For details about the characteristics of the beamline see, e.g. Reference [75].

As electron analyzer, a recently developed hemispherical spectrometer with 225 mm radius has been used (Phoibos 225 HV). The analyzer is designed for high resolution spectroscopy at kinetic energies up to 15 keV. For the present study, a 2D detector has been employed for detection of the electrons. The analyzer is equipped for parallel 2D (energy and angle) and simultaneous spin-detection using a combination of a 2D-delay-line detector with a low energy Mott-detector. Typical spectra, as taken from a Au(100) single crystal are shown in Reference [75].

Under the experimental conditions an overall resolution of 240 meV at 2 keV photon energy has been reached (monochromator plus electron detector), as was determined from the Fermi edge of Au(100). Due to the low cross-section of the valence states from the investigated compounds, the spectra had to be taken with E_{pass} from 50 eV to

150 eV and a 1 mm entrance slit for a good signal to noise ratio.

The soft X-ray photo emission spectroscopy measurements have been performed at the UE52-SGM undulator beamline (former U49) of BESSY (Berlin) using the PHOIBOS 225 HV spectrometer (SPECS). The beamline provides the soft X-ray radiation in the energy range from 100 eV to 1600 eV. For the present measurements the exit slit was set to 100 μm for a nominal resolution of about 10^4 at 750 eV for the grating with 1200 lines per mm resulting in an energy resolution of better than 100 meV. For details about the characteristics of the beamline - flux and resolution - see, e.g. Reference [76].

For site specific magnetometry, X-ray Magnetic Circular Dichroism (XMCD) in photo absorption (XAS) was performed at the *First Dragon* beamline of NSRRC (Hsinchu, Taiwan) [77, 78]. The entrance and exit slits of the monochromator were set symmetrically in the range from 10 μm to 25 μm resulting in a resolution of about 50meV at the different absorption edges. The XAS spectrum was obtained by the TEY-method, measuring directly the sample current while scanning the photon energy. The helicity of the light was fixed while two spectra with opposite directions of the external field, defined as μ^+ and μ^-, were acquired consecutively. The magnetic field applied in situ to the sample (up to 0.8 Tesla) was aligned along the surface normal and at an angle of 30 degrees with respect to the incident photon direction.

Extended X-ray absorption fine structure (EXAFS) measurements have been performed at the XAFS1 beamline of the LNLS (Brazilian Synchrotron Light Laboratory) using a Si (111) channel-cut monochromator for additional structural investigation, in particular to explain the site specific short range order. The powders (20 μm) were additionally mixed with BN and pressed to thin pellets. Powder samples were investigated in transmission mode using two ion chambers. The EXAFS spectra were analyzed using the IFEFFIT analysis package [79]. The isolated-atom background function was removed from the experimental X-ray absorption coefficient data yielding the $\chi(k)$ signal. The Fourier transform (FT) was applied using a Hanning window with a k range of 8 Å^{-1}. The structural parameters were obtained from a least-squares fit to the data in r and k-space using phase shift and amplitudes obtained from the FEFF code [80]

5 Tuning the Fermi Energy in the Middle of the Gap

5.1 Introduction

Kübler *et al* [55] recognized that the minority-spin state densities at the Fermi energy nearly vanish for Co_2MnAl and Co_2MnSn. The authors concluded that this should lead to peculiar transport properties in these Heusler compounds because only the majority density contributes. The so called half-metallic ferromagnets have been proposed as ideal candidates for spin injection devices because they have been predicted to exhibit 100 % spin polarization at the Fermi energy (ϵ_F) [3]. From the applications point of view, a high Curie temperature for a half-metallic ferromagnet may be an important condition. For this reason, Heusler alloys with $L2_1$ structure have attracted great interest. Some of these alloys exhibit high Curie temperatures and, according to theory, should have a high spin polarization at the Fermi energy [81, 82, 83]. Calculations also show that anti-site disorder will destroy the high spin polarization [84], implying that precise control of the atomic structure of the Heusler alloys is required.

The Heusler alloy Co_2MnSi has attracted particular interest because it is predicted to have a large minority spin band gap of 0.4 eV and, at 985 K, has one of the highest Curie temperature, among the known Heusler compounds [85, 86]. Structural and magnetic properties of Co_2MnSi have been reported for films and single crystals [87, 88, 89, 90, 91, 92]. In accordance with theoretical predictions, bulk Co_2MnSi has been stabilized in the $L2_1$ structure with a magnetization of 5 μ_B per formula unit. From tunneling magneto resistance (TMR) data with one electrode consisting of a Co_2MnSi film Schmalhorst *et al* [93, 94] inferred a spin polarization of 61 % at the barrier interface. Although the desired spin polarization of 100 % was not reached, the experimental value of the spin polarization is larger than the maximum 55 % effective spin polarization of a variety of $3d$-transition metal alloys in combination with Al_2O_3 barriers [95]. However, the spin polarization of photoelectrons emerging from single crystalline Co_2MnSi films grown on GaAs by pulsed laser deposition indicate a quite low spin polarization at the Fermi level of only 12 % at the free surface [92]. Wang *et al* [91, 92] assumed that partial chemical disorder was responsible for this discrepancy with the theoretical predictions.

Photo emission spectroscopy is the method of choice to study the occupied electronic structure of materials. Low kinetic energies result in a low electron mean free path being only 5.2 Åat kinetic energies of 100 eV (all values calculated for Co_2FeSi using the TPP2M equations [96]) and a depth of less than one cubic Heusler cell will contribute to the observed intensity. The situation becomes much better at high energies. In the hard X-ray region of about 8 keV one will reach a high bulk sensitivity with an escape depth being larger than 115 Å(corresponding to 20 cubic cells). High energy photo emission (at about 15 keV excitation energy) was first performed as early as 1989 [97] using a ^{57}Co Mößbauer γ-source for excitation, however, with very low resolution only.

Nowadays, high energy excitation and analysis of the electrons become easily feasible due to the development of high intense sources (insertion devices at synchrotron facilities) and multi-channel electron detection. Thus, high resolution - high energy photo emission was recently introduced by several groups [98, 99, 100, 101, 102, 103] as a bulk sensitive probe of the electronic structure in complex materials. In the present work, this method has been used at $h\nu \approx 8$ keV to study the density of states of $Co_2Mn_{1-x}Fe_xSi$ with $x = 0, 1/2, 1$.

Recent investigations [39, 104, 105, 68] of the electronic structure of Heusler compounds indicate that on-site correlation plays an important role in these compounds and may serve to destroy the half-metallic properties of Co_2MnSi. In addition, if on-site correlation is considered in electronic structure calculations Co_2FeSi becomes a half-metallic ferromagnet with a magnetic moment of 6 μ_B.

The present investigation focuses on searching for a mixed compound in the series $Co_2Mn_{1-x}Fe_xSi$ where the half-metallic behavior is stable against the variation of on-site correlation and other outside influences.

$Co_2Mn_{1-x}Fe_xSi$ samples were prepared by arc melting then annealed in an evacuated quartz tube for 21 days.

5.2 Computational Details

The present work reports, besides experiments, on calculations of the electronic and magnetic properties of ordered Heusler compounds of the $Co_2(Mn_{(1-x)}Fe_x)Si$ type. The random alloys were treated as virtual crystals of the $Co_2Mn_{(1-i/4)}Fe_{i/4}Si$ type with $i = 0, 1, 2, 3, 4$. Non-rational values of x as well as random disorder (for examples see References [106, 107, 108]) will not be discussed here.

The self-consistent electronic structure calculations were carried out using Wien2k [65].

The properties of pure compounds containing Mn or Fe were calculated in $F\,m\bar{3}m$ symmetry using the experimental lattice parameter ($a = 10.658 a_{0B}$, $a_{0B} = 0.529177$ Å) determined by X-ray powder diffraction. Co atoms are placed on 8c Wyckoff positions, Mn or Fe on 4a and Si on 4b [1]. A structural optimization for the pure compounds showed that the calculated lattice parameter deviates from the experimental one only marginally.

The calculation of mixed random alloys is not straight forward in the FLAPW as is used here. However, the substitution of some Mn atoms of the $L2_1$ structure by Fe leads in certain cases to ordered structures that can be easily used for the calculations. Those ordered, mixed compounds have the general formula sum $Co_8(Mn_{(1-x)}Fe_x)_4Si_4$ and have integer occupation of Mn and Fe if $x = i/4$ where $i = 1, 2, 3$. (for more details see Ref.[108]). To verify that ordered compounds could be used instead of random alloys, the full relativistic KKR method with CPA was employed [67]. The exchange-correlation functional was parameterized by using the plain GGA. No significant differences in the

[1] Note that 4a and 4b positions are equivalent; for clarity we assume that Si is always on 4b.

integrated properties, such as the density of states or the magnetic moments, were found between the methods.

For the case of Co_2FeSi, it has recently been demonstrated that LSDA or GGA schemes are not sufficient for describing the electronic structure correctly. Significant improvement was found, however, when the LDA+U method [39, 68] was used and this computational scheme was used here as well. LDA+U, as described by Anisimov *et al* [69], adds an orbital dependent electron-electron correlation, which is not included in the plain LSDA or GGA schemes. It should be mentioned that the $+U$ was used in the FLAPW scheme with the GGA rather than the LSDA parameterization of the exchange-correlation functional. No significant differences were observed using either of these parameterizations.

5.3 Electronic and Magnetic Structure

The electronic structure of the substitutional series $Co_2Mn_{(1-i/4)}Fe_{i/4}Si$ with $i = 0, \ldots, 4$ was calculated using the LDA+U method. This method was used because it was found that plain GGA calculations are not sufficient to explain the magnetic moments in Co_2FeSi [39]. Using the impurity model of Anisimov and Gunnarsson [109] along with self consistent calculations, the effective Coulomb-exchange parameter U_{eff} was determined for the pure compounds containing Mn and Fe. Details of the procedure and the implementation of the constrained LDA calculations in FLAPW are reported by Madsen and Novak [110]. The values found in the present work are $U_{Co} = 0.30$ Ry and $U_{Mn} = 0.39$ Ry for Co_2MnSi, and $U_{Co} = 0.31$ Ry and $U_{Fe} = 0.32$ Ry for Co_2FeSi.

Comparing the semi-empirical values used in [68] to the values found here from the constrained LDA calculations, it is evident that the latter are too high to explain the magnetic moments. Additional calculations for the elemental $3d$ transition metals revealed that all values for U_{eff} found in the constrained LDA calculations are considerably too high to explain those metallic systems correctly. This is despite the fact that such calculations may result in reliable values for Mott insulators [111].

For these reasons, the semi-empirical values corresponding to 7.5 % of the atomic values (see Reference [68]) will be used and discussed here for the case of the FLAPW calculations. These values ensure that the calculated magnetic moments agree with the measured values over the entire range of the Fe concentration (compare Section 5.6). In particular, the values for U_{eff} were set to $U_{Co} = 0.14$ Ry, $U_{Fe} = 0.132$ Ry, and $U_{Mn} = 0.13$ Ry, independent of the iron concentration. These values are closer to the values for the Coulomb interaction U_{dd} for d electrons in the elemental $3d$ transition metals reported by Bandyopadhyay and Sarma [112] even before the LDA+U method itself was introduced.

The use of $Ueff = U - J$ suppresses multipole effects. That means, it neglects the non-spherical terms in the expansion of the Coulomb interaction. Additionally, full potential linearized muffin tin orbitals (FPLMTO) calculations were performed to check for the influence of the non-spherical terms. Differently, the LMTART 6.5 program provided by Savrasov [113] uses the Slater integrals $F^0 \ldots F^4$ for the calculation of the on-site

Table 5.1: $LDA + U$ parameter for $Co_2Mn_{1-x}Fe_xSi$. (All values are given in Ry.)

element	Ref.:[112] U_{dd}	constrained LDA U	FLAPW U_{eff}	FPLMTO F^0	F^2	F^4
Co	0.194	0.3(1)	0.140	0.185	0.085	0.053
Fe	0.171	0.32	0.132	0.175	0.081	0.050
Mn	0.148	0.39	0.130	0.164	0.076	0.047

correlation with $U = F^0$ and $J = (F^2 + F^4)/14$ (see also References [109, 69]).

As in FLAPW, the use of the U values from the constrained LDA calculations leads also in FPLMTO to much too large values for the magnetic moments compared to the experimental findings. In a next step, only reduced values for F^0 were used. Following the arguments of Reference[114], only F^0 should be effected by the screening in the solid state. However, the use of the atomic values for F^2 and F^4 as proposed in Reference[114] still did not lead to satisfactory values for the magnetic moments. Finally, the reduction of all Slater integrals to 10 % of their atomic values was leading to results being compatible to the measured magnetic moments. Moreover, nearly identical results as in FLAPW were obtained concerning not only the magnetic moments but also the band structures. The slightly higher values resulting in the most appropriate for FPLMTO are caused by the fact that these calculations used the U on top of the LDA exchange-correlation functional and not on top of the GGA parameterization. This behavior reveals that GGA includes some more correlation compared to pure LDA. It is also observed within the FLAPW scheme.

The different values for U, U_{dd}, U_{eff}, and $F^0 \ldots F^4$ are summarized in Table 5.1. The values according to Reference[112] where calculated for the d-state occupation as found from calculations using spherical potentials. The values for FLAPW are calculated from the Slater integrals reduced to 7.5% of the atomic values as calculated by Cowans program [115, 68] and the values for FPLMTO correspond to 10% of the atomic values. The use of these values leads to nearly identical results comparing FLAPW and FPLMTO.

In the following, only the results from the FLAPW calculations are discussed to allow for a better comparison with previous work. However, all results shown below are compatible and agree very well with those using LDA+U in FPLMTO calculations. Figure 5.1 shows the spin resolved band structure and the total density of states for the pure compounds Co_2MnSi and Co_2FeSi as calculated within the framework of the LDA+U. In all cases, the band structures are very similar and the gap in the minority bands is clearly revealed.

When explaining the Heusler half-metallic ferromagnets using simple rigid band-like or molecular orbital-like models, it is expected that the additional d electron of the Fe compound fills the majority states while not affecting the minority states. As may be seen from Figure 5.1, this is clearly a strong oversimplification. The additional electron must be absorbed in the strongly dispersing unoccupied d-bands seen in the Mn compound just above ϵ_F. Comparing the majority DOS, it can be seen that the high density d-states at

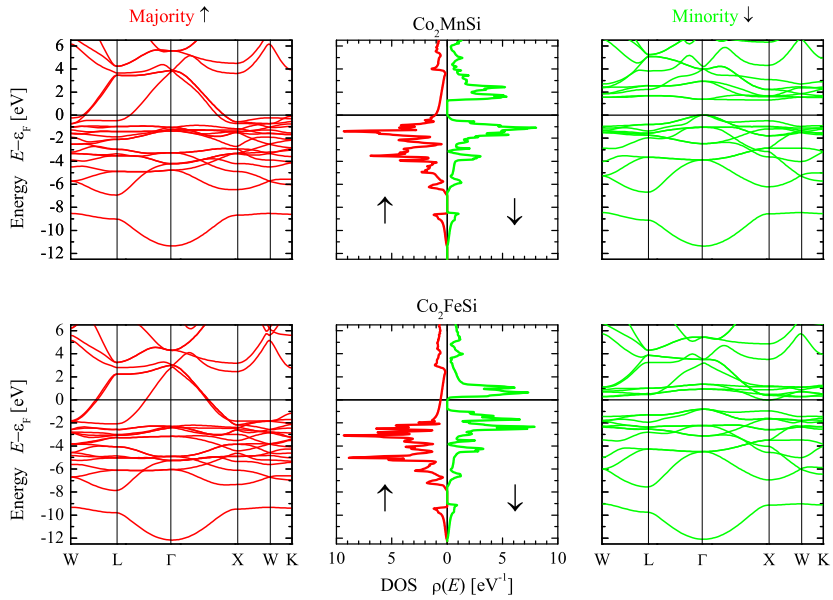

Figure 5.1: Band structure and density of states of Co_2MnSi and Co_2FeSi.

-1.4 eV (or -3.5 eV) in Co_2MnSi are shifted to approximately -3 eV (or -5 eV) in Co_2FeSi. Keeping the minority DOS fixed, this would imply an additional exchange splitting of about 1.6 eV, when compared to Co_2MnSi, between the majority and minority states in Co_2FeSi. This large and rather unphysical shift indicates that the rigid band model fails and that other alterations of the band structure must take place.

After inspecting the electronic structure in more detail, some particular changes are found. For example, the rather large shift of the occupied majority *d*-states is compensated by a shift of the occupied minority *d*-states, and this keeps the exchange splitting rather fixed. This then results in a shift and splitting of the occupied minority *d*-states (seen at -1 eV in the Mn compound and at -1.7 eV or -2.3 eV in the Fe compound) as well as a shift of the unoccupied minority *d*-states towards the Fermi energy. In addition, the splitting of the unoccupied minority *d*-states just above the gap is reduced from 0.7 eV in Co_2MnSi to 0.4 eV in Co_2FeSi. The most striking effect, however, is the shift of the Fermi energy from the top of the minority valence band to the bottom of the minority conduction band. These particular positions of the minority gap with respect to the Fermi energy make both systems rather unstable with respect to their electronic and magnetic properties. Any small change of a physically relevant quantity may serve to destroy the HMF character by shifting the Fermi energy completely outside of the minority gap. As long as the shift is assumed to be small, the magnetic moment may still be similar to the one expected from a Slater-Pauling behavior, even so, the minority gap is destroyed. For this reason, the magnetic moment may not provide evidence for a

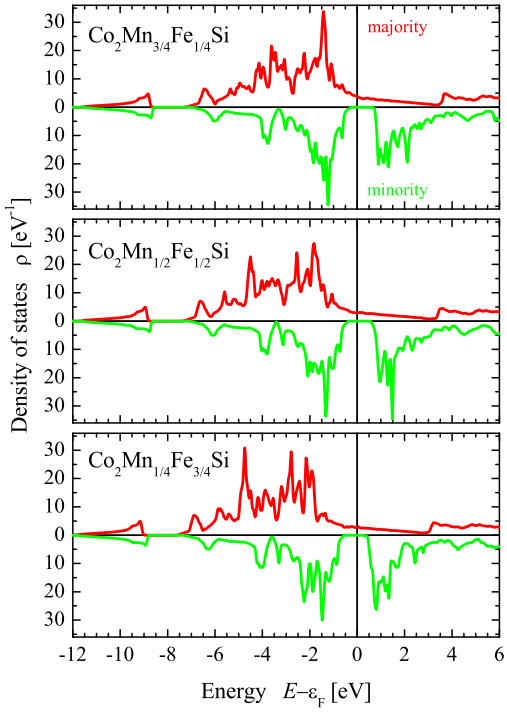

Figure 5.2: Spin resolved density of states of $Co_2Mn_{1-x}Fe_xSi$ for $x = 1/4, 1/2$, and $3/4$.

half-metallic state.

It is to be immediately expected that the situation improves in the mixed compounds containing both Mn and Fe. Figure 5.2 shows the spin resolved total density of states for the compounds with an intermediate Fe concentration ($x \neq 0, 1$). In all cases, the gap in the minority bands is kept.

The shift of the majority d-states with low dispersion away from the Fermi energy is clearly visible in Fig: 5.2. The additional charge (with increasing Fe concentration x) is filling the strongly dispersing d-states in the majority channel. At the same time, the minority DOS is shifted with respect to the Fermi energy such that ϵ_F moves from the top of the minority valence bands at low x to the bottom of the minority conduction bands at high x. In general, it can be concluded that the additional electrons affect both majority and minority states.

Table 5.2 summarizes the results for the gap in the minority states as found from LDA+U calculations. The largest gap in the minority states is found for Co_2MnSi. The size of the gap decreases with increasing Fe content x, and at the same time, the position of the Fermi energy is moved from the top of the valence band to the bottom of the conduction band. It is also seen that the compounds with $x = 0$ and 1 are on the borderline to half-metallic ferromagnetism, as the Fermi energy just touches the top of the valence band or the bottom of the conduction band. In both cases, a slight change

Table 5.2: Properties of the minority gap of ordered $Co_2Mn_{1-x}Fe_xSi$. Given are the extremal energies of the valence band maximum (VB_{max}), the conduction band minimum (CB_{min}), and the resulting gap (ΔE) in the minority states as found from LDA+U calculations. The extremal energies are given with respect to ϵ_F. All energies are given in eV.

x	VB_{max}	CB_{min}	ΔE
0	0.003	1.307	1.3
1/4	-0.181	0.970	1.15
1/2	-0.386	0.495	0.88
3/4	-0.582	0.181	0.86
1	-0.810	-0.028	0.78

of U_{eff} in the calculation is able to shift ϵ_F outside of the gap in the minority states.

For intermediate Fe concentration, the Fermi energy falls close to the middle of the gap in the minority states (see also Figure 5.2). This situation makes the magnetic and electronic properties of the compound very stable against external influences that will not be able to change the number of minority electrons. This applies both to the parameters in the theoretical calculations as well as the actual experimental situation. From this observation it can be concluded that $Co_2Mn_{1/2}Fe_{1/2}Si$ exhibits a very stable half-metallic character in this series of compounds, as well as those with a concentration close to $x = 0.5$.

If the Heusler alloys are half-metallic ferromagnets, then they will show a Slater-Pauling behavior for the magnetization, meaning that the saturation magnetization scales with the number of valence electrons [81, 83, 45]. The magnetic moment per unit cell (in multiples of the Bohr magneton μ_B) is given by:

$$m = N_V - 24, \tag{5.1}$$

with N_V denoting the accumulated number of valence electrons in the unit cell. For Co_2MnSi there is a total of $2 \times 9 + 7 + 4 = 29$ valence electrons in the unit cell and accordingly 30 for Co_2FeSi. for this reason the magnetic moment is expected to vary linearly from 5 μ_B to 6 μ_B with increasing iron concentration in $Co_2Mn_{1-x}Fe_xSi$.

The results found from the LDA+U calculations for the magnetic moments are summarized in Table 5.3 and compared to pure GGA calculations without the inclusion of the U type correlation. It is evident from Table 5.3 that the GGA derived values do not follow the Slater-Pauling curve (with the exception of Co_2MnSi), whereas the values from the LDA+U follow the curve closely. These results again indicate the loss of the minority gap - and thus the loss of half-metallicity - if the on-site correlation is not included.

Table 5.3: Total magnetic moments of ordered $Co_2Mn_{1-x}Fe_xSi$. All moments were calculated for the given super-cells. Their values are in μ_B and respect 4 atoms in the unit cell for easier comparison.

compound	x	GGA	LDA+U
Co_2MnSi	0	5.00	5.00
$Co_8Mn_3FeSi_4$	1/4	5.21	5.25
$Co_4MnFeSi_2$	1/2	5.44	5.50
$Co_8MnFe_3Si_4$	3/4	5.55	5.75
Co_2FeSi	1	5.56	6.00

5.4 Structural Properties

Structural characterization has been performed with X-ray diffraction (XRD) of powders as the standard method. Due to the small differences in the scattering factors between the 3d metals Mn, Fe and Co, structural information, other than a simple confirmation of a single cubic phase can only be gained by measuring the comparatively small (5 % of the (220)-peak) (111) and (200) superstructure peaks that are typical for the face centered cubic (fcc) lattice. The simulated powder diffraction pattern of Co_2MnSi shows the decisive (111) and (200) peaks for the defect-free structure. Both of these super-lattice peaks vanish for a random occupation of all lattice sites (4a, 4b, and 8c) resulting in the $A2$ structure. In the case of random occupation of 4a and 4b sites by Mn, Fe, and Si, only the (200) super-lattice peak of the $B2$ structure type would be seen, while the (111) peak would vanish.

Such types of disorder would close the gap in the minority DOS so that the material would no longer be a half-metallic ferromagnet [108, 105]. However, the magnetic moments may still follow a Slater-Pauling like behavior. The half-metallic character is also destroyed when only one of the Co atoms is exchanged by Mn/Fe (X structure [116] with symmetry $F\,\bar{4}3m$). This type of disorder shows up as a (111) super-lattice peak with higher intensity than the (200) peak.

As expected for the defect-free structure, the experimental data show both the (111) and (200) peaks with equal intensity for all Fe concentrations indicating the presence of a long range fcc structure for all samples (see Figure 5.3). Within the uncertainty of the experiment, the lattice parameter of 5.64 Å remains nearly independent of the Fe concentration .

Because the scattering factors of all three transition metals are very similar, X-ray diffraction cannot easily discern a disorder when the Mn and Fe are partially exchanged with Co atoms on both 8a positions (DO_3 like disorder). Because both have the same $Fm\bar{3}m$ symmetry, this leads to nearly identical diffraction patterns when going from the $L2_1$ to the DO_3 structure. As will be shown in the next section, this type of disorder can be ruled out by means of Mößbauer spectroscopy.

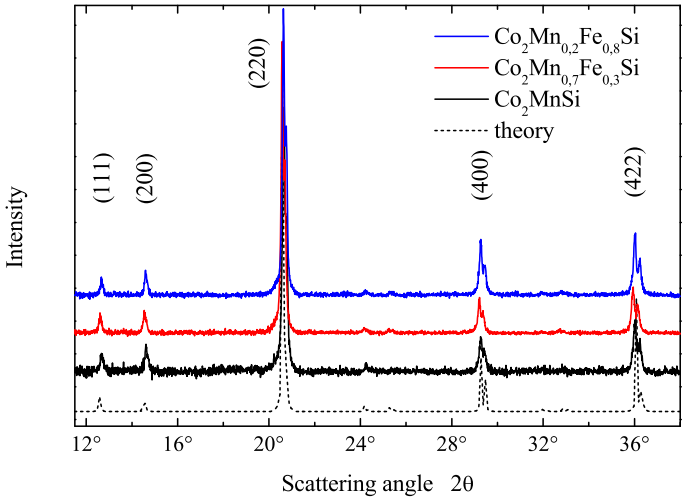

Figure 5.3: XRD spectra for Co_2MnSi and $Co_2Mn_{0.8}Fe_{0.2}Si$. The spectra were excited by Mo K_α radiation.

5.5 Magneto-structural Properties

^{57}Fe Mößbauer spectroscopy was performed to investigate the magneto-structural properties. The transmission spectrum of $Co_2Mn_{0.5}Fe_{0.5}Si$ is shown in Figure 5.4. Starting from 10 %, the spectra for the complete range of Fe concentration x are all similar and therefore not shown here. The observed sextet-like pattern is typical for a magnetically ordered system. The pattern is typical for the cubic symmetry and no asymmetric shift of the lines from a non-cubic quadrupole interaction is observed.

The spectrum shown in Figure 5.4 for 50 % Fe is dominated by an intense sextet. With Fe occupying the 4a sites with cubic symmetry (O_h), this sextet indicates on the high order of the sample. In addition to the sextet, a much weaker line at the center of the spectrum is visible. Depending upon the composition it can be explained as a singlet or doublet. Its contribution to the overall intensity of the spectrum is approximately 3.5 % at $x = 0.5$. The origin of the singlet or doublet may be caused by anti-site disorder leading to a small fraction of paramagnetic Fe atoms. The splitting of the paramagnetic line into a doublet is due to dynamic effects and, among others reasons, usually depends upon the size of the powder grains. The slight disorder arises most likely from surface regions of the sample that are destroyed when the sample is crushed to powder. A partial contamination of the relatively large surface area of the powder with oxygen can also not been excluded. The relative contribution of the doublet decreases exponentially from 9 % in low Fe-substituted $Co_2Mn_{0.9}Fe_{0.1}Si$ to 1.8 % in pure Co_2FeSi. As was also suggested by the photo absorption and ESCA measurements, this may indicate a larger probability for oxidation in the Mn rich part of the series.

The line width of the sextet is approximately (0.14 ± 0.01) mm/s (corresponding to

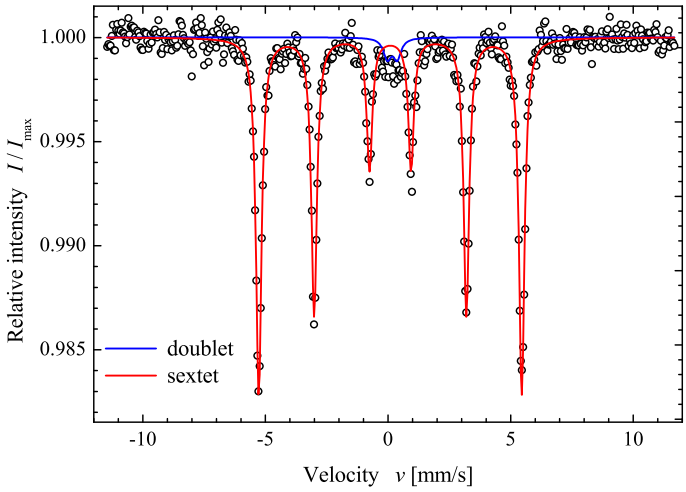

Figure 5.4: ^{57}Fe Mößbauer spectrum of $Co_2Mn_{0.5}Fe_{0.5}Si$. The spectrum was taken at 290K and excited by a ^{57}Co(Rh) source. Solid lines are results of a fit to determine the sextet and doublet contributions and to evaluate the hyperfine field.

6.7 neV) on average over the complete series of compositions. A pronouncedly higher line width of $\approx$ 0.19mm/s was found for the alloy with $x = 0.7$. This indicates a higher disorder in that sample and may also explain the slightly higher magnetic moment (compare Figure 5.8 in Section 5.6). The isomer shift increases linearly from 0.075 mm/s (3.6 neV) to 0.129 mm/s (6.2 neV) with increasing x, indicating the change in the environment of the Fe atoms, that appears here in the second nearest neighbor shell where the next Fe or Mn atoms are located. Despite this increase, the values suggest a Fe^{3+}-like character of the iron atoms in $Co_2Mn_{1-x}Fe_xSi$. The increase points on a slight decrease of the valence electron concentration close to the iron atoms. Table 5.4 summarizes the values for the isomer shift and the hyperfine field (H_{hff}) as function of the iron concentration.

The hyperfine field at the Fe sites amounts to 26.5×10^6 A/m in $Co_2Mn_{0.5}Fe_{0.5}Si$. This is the maximum value observed in the complete series with varying Fe concentration x. Overall, the hyperfine field varies non-linearly from 25.9×10^6 A/m at $x = 0.1$ to 25×10^6 A/m at $x = 1$ (see also: [2]). For low iron concentration, it increases with x and decreases from $x = 0.5$ to $x = 1$. It should be noted that the Mößbauer spectra taken at 85K from Co_2FeSi exhibited a considerably higher value (26.3×10^6 A/m) without additional singlet or doublet contributions. Therefore, thermally activated fluctuations or disorder can not be excluded here. The values of the hyperfine field at the Fe atoms are comparable to those found by Niculescu *et al* [117, 118] using spin-echo nuclear magnetic resonance (NMR). For $Co_{3-x}Fe_xSi$, these authors reported approximately 26.9×10^6 A/m

[2]Note that the Mößbauer data reported in Ref.[39] were taken at lower temperature (85K).

Table 5.4: Mößbauer data for iron in $Co_2Mn_{1-x}Fe_xSi$. Given are the measured and calculated values of the hyperfine field (H_{hff}) and the measured isomer shift (IS) for increasing Fe concentration x.

x	H_{hff} [10^6 A/m] Experiment	Calculation	IS [neV]
0.1	25.937		3.61
0.2	26.214		3.77
0.25	-	26.534	
0.4	26.412		4.18
0.5	26.466	26.629	4.34
0.6	26.417		4.75
0.7	26.259		4.90
0.75	-	26.962	
0.8	25.915		5.33
0.9	25.480		5.77
1	24.997	27.013	6.21

for iron on 4a sites. The values for partial occupancy of 8c sites, expected from NMR [118] ($\approx 16 \times 10^6$ A/m) for Co_2FeSi are considerably smaller. This is in agreement with calculations for Co and Fe on interchanged sites ($\approx 17 \times 10^6$ A/m). Therefore, a DO_3 type disorder can be excluded. The calculated hyperfine fields are, however, nearly independent of the Fe concentration. They decrease linearly with x by -0.7×10^6 A/m from 27.01×10^6 A/m for Co_2FeSi. A maximum in the $H_{hff}(x)$ dependence at $x = 1/2$ could not be verified. It was found neither for the ordered compounds using the FLAPW method with the LDA+U (see Table 5.4), nor for random alloys calculated using a KKR-CPA scheme in the GGA approximation [3].

Differential scanning calorimetry was used to find the high temperature phase transitions in the substitutional series. Figure 5.5 shows a typical result from DSC, which was used to investigate the expected phase transitions. The figure displays the change of the DSC signal as a function of the temperature using nominal heating and cooling rates of 20 K/min. A strong signal arising from a phase transition is easily detected at about 1000 K to 1050 K during both heating and cooling. The shift of the maxima is mainly due to an intrinsic hysteresis effect of the method and depends on the temperature rates and the actual amount of material. The length of the error bars in Figure 5.6 corresponds to this hysteresis.

A series of DSC measurements was performed with different scanning rates for heating and cooling, but it was not possible to distinguish the magnetic transition temperature because it was too close to the structural transition temperature of the $L2_1$ to the $B2$

[3] Note that these calculations need at present a rather unphysical enlargement of the lattice parameter in order to explain the magnetic moments and position of the minority gap correctly.

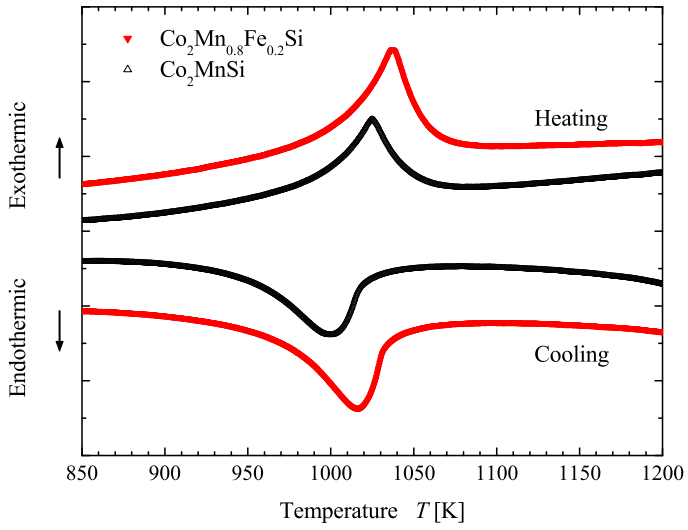

Figure 5.5: DSC results for Co_2MnSi and $Co_2Mn_{0.8}Fe_{0.2}Si$.

phase $T_t^{B2\leftrightarrow L2_1}$. To overcome the problem of nearby phase transitions of different kind, it would be necessary to obtain high temperature magnetization curves such as those that Kobayashi et al. [119] obtained in their examination of the series $Co_2Cr_{1-x}Fe_xGa$, or the difference in the transition temperatures should be more than 100 K.

Figure 5.6 displays the temperature dependence of the $L2_1 \leftrightarrow B2$ phase transition. It is nearly constant, increasing slightly, as the Fe content increases, from ≈ 1024 K for Co_2MnSi to ≈ 1031 K for Co_2FeSi. It is seen that the Curie temperatures of the end members of the substitutional series are slightly below or above the structural phase transition for the compound containing Mn or Fe, respectively. The Curie temperature is expected to increase with increasing x from $T_C(0) = 985$ K [120] to $T_C(1) = 1100$ K [39], while in $Co_2Mn_{1-x}Fe_xSi$ $T_t^{B2\leftrightarrow L2_1}$ hardly varies with increasing x, being around 1027 K for $x = 0.5$. It is therefore impossible here to unambiguously determine T_C by using the DSC technique, because of the relative weakness of the magnetic transition compared to the structural transition and the overlap of those two transitions in the DSC spectra. It is interesting to note that the Curie temperature of the compounds with high Fe concentration appears to be above the order-disorder phase transition.

5.6 Magnetic Properties

The Co_2-based Heusler alloys that are half-metallic ferromagnets show a Slater-Pauling like behavior for the magnetization. The saturation magnetization scales with the number of valence electrons [83] and the magnetic moment per unit cell is given by equation 5.1. A magnetic moment of:

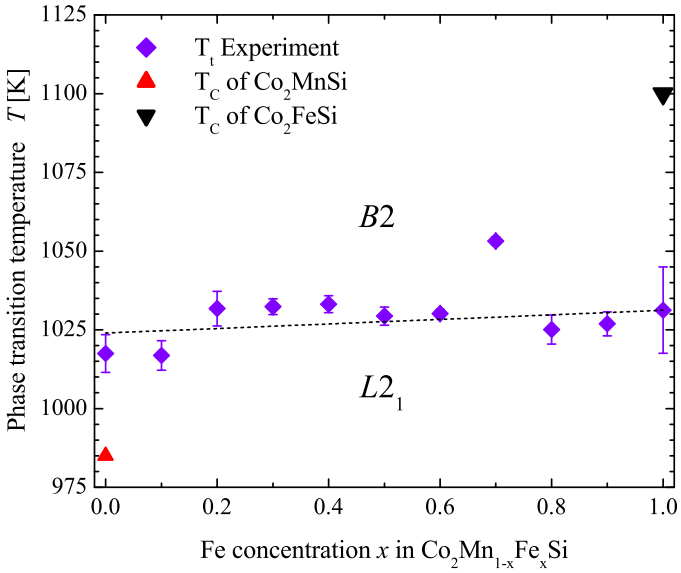

Figure 5.6: Phase transitions in $Co_2Mn_{1-x}Fe_xSi$. The straight line is the result of a linear fit of $T_t(x)$ as function of the Fe concentration. The given Curie temperatures are taken from References. [120] and [39] for Co_2MnSi and Co_2FeSi, respectively.

$$m(x) = (5 + x)\mu_B \tag{5.2}$$

is expected for $Co_2Mn_{1-x}Fe_xSi$.

Low temperature magnetometry was performed by means of the SQUID to check the calculated saturation moment. Selected results are shown in Figure 5.7. The increase of the saturation moment with the iron concentration is clearly visible. In addition, it is found that all $Co_2Mn_{1-x}Fe_xSi$ samples are soft magnetic with a small remanence and a small coercive field. Results for the element-specific magnetic moments from X-ray magnetic circular dichroism are reported elsewhere [121].

The total magnetic moments, measured at 5 K and in saturation, are $(4.97 \pm 0.05)\mu_B$ and $(5.97 \pm 0.05)\mu_B$ for the pure compounds Co_2MnSi and Co_2FeSi, respectively. The latter is in perfect agreement with the recent investigation reported in References[39, 104]. Figure 5.8 displays the dependence of the saturation moment as a function of the Fe concentration x. The series shows a nearly linear increase of m with increasing Fe concentration that closely fits the values expected from a Slater-Pauling like behavior.

Comparing the experimental results to the theoretical values as given in Table 5.3, it is evident that they closely agree with those from the LDA+U calculations. The agreement of the GGA result for Co_2MnSi may thus be seen as due to chance. The comparison also substantiates the use of correlation energies of about 0.135 Ry, as these can be used

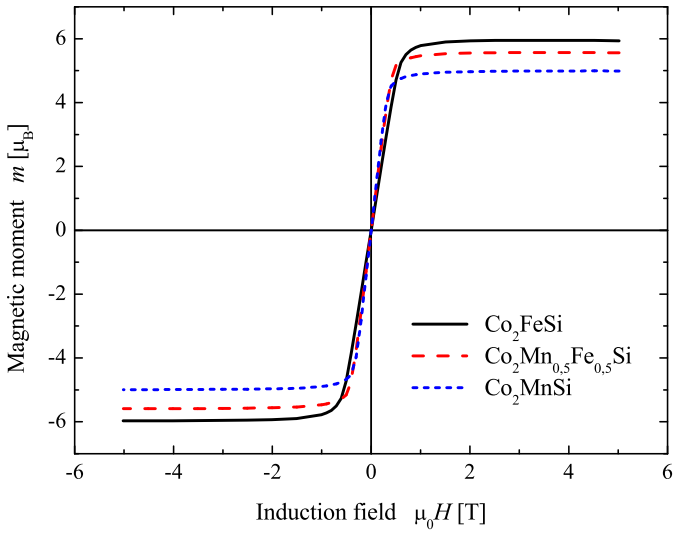

Figure 5.7: Magnetization of $Co_2Mn_{1-x}Fe_xSi$.
Displayed are the hysteresis curves for $x = 0, 0.5, 1$ taken at $T = 5$ K.

to predict the magnetic moment correctly over the entire range of Fe concentration x.

5.7 Electronic Properties

The results from high energy photo emission are shown in Figure 5.9 and compared to the total density of states calculated for $Co_2Mn_{1-x}Fe_xSi$ with $x = 0, 1/2, 1$). The calculated total DOS is the sum of the spin resolved majority and minority DOS shown in Figures 5.1 & 5.2 and convoluted with a Fermi-Dirac distribution using $T = 20$ K.

The spectra of all three compounds reveal clearly the low lying s-states at about -11 eV to -9 eV below the Fermi energy, in well agreement to the calculated DOS. These low lying bands are separated from the high lying d-states by the Heusler-typical hybridization gap being clearly resolved in the spectra as well as the calculated DOS. The size of this gap amounts typically to $\Delta E \approx 2$ eV in Si containing compounds.

Obviously, the emission from the low lying s-states is pronouncedly enhanced compared to the emission from the d-states. This can be explained by a different behavior of the cross sections of the s, p, and d states with increasing kinetic energy as was recently demonstrated by Panaccione *et al* for the case of the silver valence band [102]. In particular, the cross section for d-states decreases faster with increasing photon energy than the one of the s-states. This behavior influences also the onset of the d-bands at about -7 eV. Just at the bottom of those d-bands, they are hybridized with s, p-like states, leading to a high intensity in this energy region.

The structure of the spectra in the range of the d states agrees with the structures

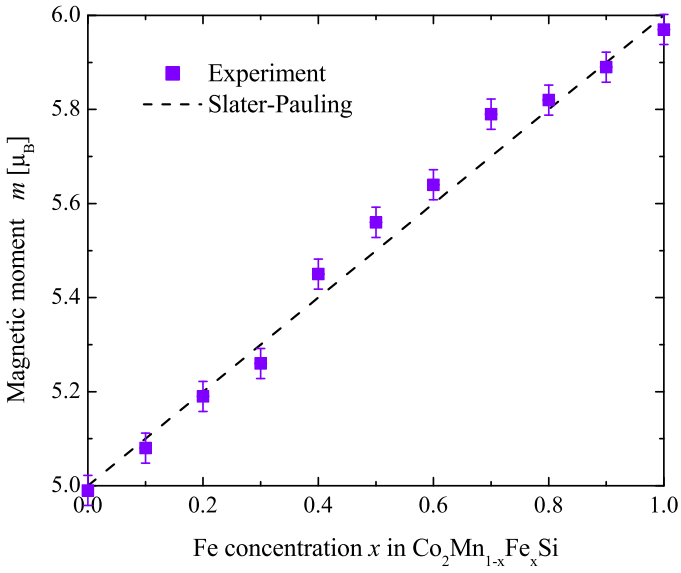

Figure 5.8: Concentration dependence of the magnetic moment in $Co_2Mn_{1-x}Fe_xSi$. All measurements were performed at $T = 5$ K.

observed in the total DOS. However, one has to account for lifetime broadening and the experimental resolution if comparing that energy range. The lowest flat band of the majority band structure (see Figure 5.1), accompanying the localized moment at the Y sites, results in a sharp peak in the DOS at about -3.5 eV and -5 eV for Mn and Fe, respectively (marked by arrows in Fig.5.9 a) and c). These peaks are shifted away from ϵ_F by the electron-electron correlation in the LDA+U calculation and would appear without U closer to the Fermi energy. Their energetic position corresponds to structures revealed in the measured spectra, thus they are a good proof for the use of the LDA+U scheme.

Most interesting is the behavior of the calculated DOS and the measured spectra close to ϵ_F as this might give an advice about the gap in the minority states. The majority band structure contributes only few states to the density at ϵ_F emerging from strongly dispersing bands. This region of low density is enclosed by a high density of states arising from flat bands at the upper and lower limits of the minority band gap. The onset of the minority valence band is clearly seen in the total DOS as well as the low majority density at the Fermi energy. The same behavior is observed in the measured valence band spectra. From the spectra, it can be estimated that the Fermi energy is in all three cases about 0.5 eV above the minority valence band. This gives strong evidence that all compounds of the $Co_2Mn_{1-x}Fe_xSi$ series exhibit really half-metallic ferromagnetism.

The values for U_{eff} used in section 5.3 are the borderline cases for the half-metallic ferromagnetism over the complete series $Co_2Mn_{1-x}Fe_xSi$. They were used being independent of the Fe concentration, what was suggested for Co from the constrained LDA

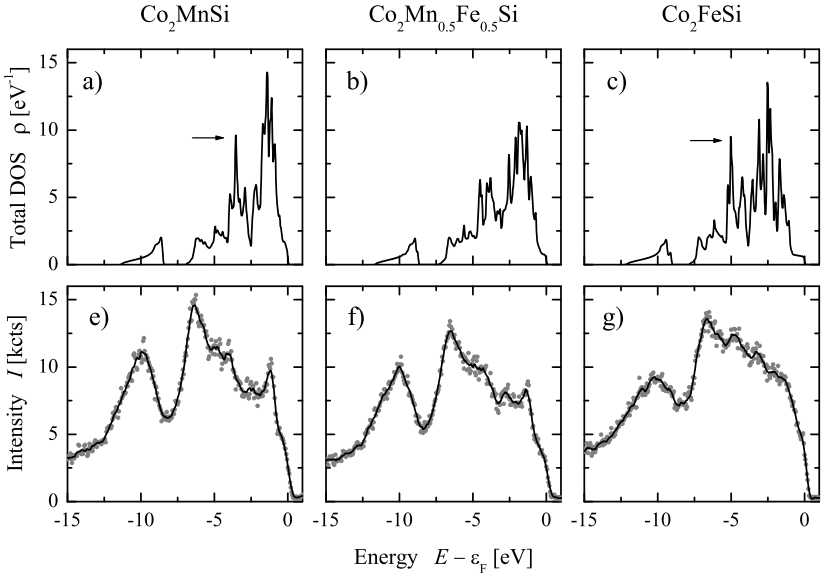

Figure 5.9: Valence density of $Co_2Mn_{1-x}Fe_xSi$ ($x = 0, 1/2, 1$).
The calculated total density of states (a, b, c) has been convoluted by a Fermi-Dirac distribution using $T = 20$ K. The photoelectron spectra (e, f, g) have been excited by $h\nu = 7.939$ keV.

calculations. However, the valence band spectra shown in Figure 5.9 indicate that the Fermi energy of both end members may fall inside of the minority gap rather than being located at the edges of the minority gap. This situation may be simulated by a variation of U. A comparison to the U-dependence of the minority gap shown in Reference [68] suggests smaller effective Coulomb exchange parameters for the Mn rich part and larger ones for the Fe rich part of the series. This might also explain the non-linearity reported in section 5.6 for the hyperfine field. A variation of those parameters for all contributing $3d$ constituents in the calculations was omitted here because it would not bring more insight into the nature of the problem, at present.

Overall, the measured photoelectron spectra agree well with the calculated density of states and principally verify the use of the LDA+U scheme. In particular, the shape of the spectra close to ϵ_F can be explained by the occurrence of a gap in the minority states and thus points indirectly on the half-metallic state of all three compounds investigated here by photo emission. For clarity about the gap, spin resolved photo emission spectroscopy at high energies would be highly desirable. However, this will make another step of improvement of the instrumentation necessary, for both photon sources as well as electron energy and spin analyzers, as the spin detection will need a factor of at least three to four orders of magnitude more intensity for a single energy channel at the same resolution as used here for the intensity spectra.

5.8 Summary and Conclusion

The substitutional series of the quaternary Heusler compound $Co_2Mn_{1-x}Fe_xSi$ was synthesized and investigated both experimentally and theoretically.

The results found from the LDA+U calculations for the magnetic moments $m(x)$ closely follow the Slater-Pauling curve. The shift of the minority gap with respect to the Fermi energy, from the top of the minority valence band for Co_2MnSi to the bottom of the minority conduction band for Co_2FeSi, makes both systems rather unstable with respect to their electronic and magnetic properties. The calculated band structures suggest that the most stable compound in a half-metallic state will occur at an intermediate Fe concentration. These theoretical findings are supported by the experiments.

All samples of the substitutional series exhibit an $L2_1$ order that is independent of the Fe concentration x. The observed structural order-disorder phase transition from $L2_1 \leftrightarrow B2$ is nearly independent of x and occurs at about 1030 K. Mößbauer measurements show only a negligible paramagnetic contribution confirming the high degree of order over the whole substitutional series. In agreement with the expectation from the Slater-Pauling curve, the magnetic moment increases linearly with x from 5 μ_B to 6 μ_B. True bulk sensitive, high energy photo emission bearded out the inclusion of electron-electron correlation in the calculation of the electronic structure and gave an indirect advise on the gap in the minority states. Both, valence band spectra and hyperfine fields indicate an increase of the effective Coulomb exchange parameters with increasing Fe concentration.

From both the experimental and computational results it is concluded that a compound with an intermediate Fe concentration of about 50% should be most stable and best suited for spintronic applications.

6 Optimization for GMR/TMR Applications

6.1 Introduction

Heusler compounds [57] have attracted scientific and technological interest for their potential use as materials for magnetoelectronic devices [122]. Reason is the exceptional electronic structure found in particular in the Co_2YZ Heusler compounds (Y = transition metal, Z = main group element). Kübler *et al.* [55] concluded from ab-initio calculations that Co_2 based compounds will have peculiar transport properties when they recognized that the minority-spin density at the Fermi energy ϵ_F vanishes in Co_2MnAl and Co_2MnSn. That means, those compounds exhibit a complete spin polarization at ϵ_F such that they behave like a metal for electrons of one spin direction and like an insulator for the other one. In particular, all Co_2 based Heusler compounds are half-metallic ferromagnets [3], as recently demonstrated in ab-initio calculations (see [123] and references there).

Besides the ternary Co_2YZ Heusler compounds, there exist also a large assortments of substitutional quaternary alloys. One of the early substitutional series that attracted interest as potential material for magnetoelectronics was $Co_2Cr_{1-x}Fe_xAl$ [124, 108]. Disadvantage of this series is that it is hard to be stabilized in the $L2_1$ structure. Mostly a mixture of atoms in Y and Z positions is observed leading to $B2$-like disorder [107]. However, the disorder destroys the half-metallic properties [105], despite that high tunneling magneto resistance (TMR) ratios have been observed for $Co_2Cr_{0.6}Fe_{0.4}Al$ [125]. The series $Co_2Mn_{1-x}Fe_xSi$ has also attracted particular interest because it exhibits the $L2_1$ order over the whole range of x [126] and the end member with $x = 1$ exhibits the highest Curie temperature of all Heusler compounds [104]. The end members of this series ($x = 0$ and 1) have been used for fabrication of magnetic tunnel junctions [127, 128, 129]. The tunnel magnetoresistance (TMR) ratios of 159% in the Mn compound at low temperature and 41% in the Fe compound at room temperature suggest that still an improvement with respect to the temperature stability of the TMR is necessary.

In $Co_2Mn_{1-x}Fe_xSi$ the transition metal carrying the localized moment is exchanged. This might lead to unexpected effects on the magnetic properties if the samples are not completely homogeneous. The situation is different in the iso-electronic series $Co_2FeAl_{1-x}Si_x$ where the main group element is substituted. Tezuka *et al.* [130, 131] reported about TMR junctions build from $Co_2FeAl_{0.5}Si_{0.5}$. The junctions exhibited TMR ratios of 76% at 300 K and 106% at 5 K for the $B2$ structure while the junctions with $L2_1$ structure showed 51% and 78% at 300 K and 5 K, respectively. The TMR ratio is 175% at 300 K for optimized junctions with $L2_1$ structure [131] and thus larger than the ones found for pure Co_2FeAl or Co_2FeSi electrodes.

Recent ab-initio calculations [132] indicated that the compound with 50% of the Al substituted by Si will lead to a situation where ϵ_F is located close to the middle of the

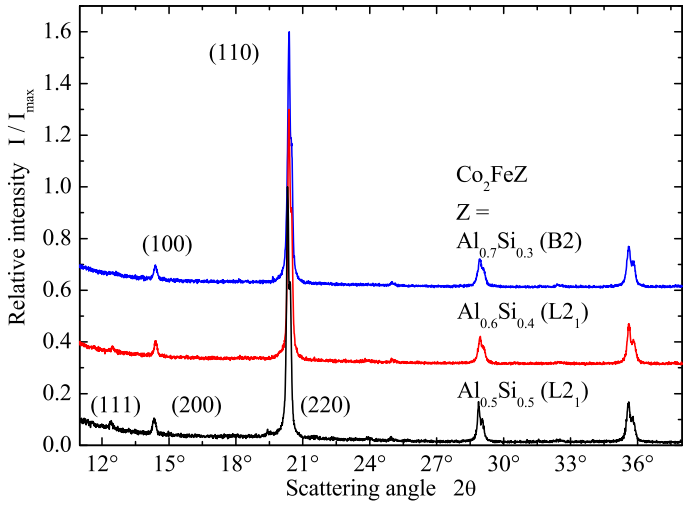

Figure 6.1: Powder diffraction of $Co_2FeAl_{1-x}Si_x$. Shown are the powder pattern measured with Mo K_α at room temperature for selected compositions with $x = 0.3$, 0.4, and 0.5. (Note that the indices of the reflections are different in the $L2_1$ and $B2$ structures due to the different symmetry of the lattices.

minority gap and thus should lead to an improved temperature stability of the spin polarization, in particular if quasi particle excitations are appearing close to the band edges. The present study is devoted to the bulk properties of $Co_2FeAl_{1-x}Si_x$ in order to find the most stable compound of the series with respect to the structural and magnetic properties and thus the most promising candidate for thin film devices using them in GMR and TMR applications.

6.2 Structural Properties

The $Co_2FeAl_{1-x}Si_x$ samples with varying x in steps of 0.1 were prepared by arc melting of stoichiometric amounts of the constituents in an argon atmosphere at 10^{-4} mbar, resulting in polycrystalline ingots. The as-cast samples (data not shown here) exhibit for $x > 0.5$ already the $L2_1$ structure and only samples with higher Al content exhibit a $B2$ structure. To improve the structural properties, the ingots were annealed at about 1000 K in an evacuated quartz tube for 7 days afterwards. This procedure resulted in samples exhibiting the $L2_1$ structure for $x \geq 0.4$ and the $B2$ structure for $x < 0.4$.

The crystalline structure was determined by X-ray powder diffraction (XRD) using excitation by Mo K_α radiation. Typical powder diffraction patterns are shown in Figure 6.1. The lattice parameter found from the Rietveld-refinement is $a = 5.665$ Å and almost independent of the Si concentration x. For compounds with $x \geq 0.4$, the (111) and (200) reflections being indicative for the $L2_1$ structure are clearly visible. At $x = 0.3$ the

(111) reflection is hardly detectable pointing on a $B2$ structure. The Rietveld-refinement points on a partial Fe-Z (Z=Al, Si) antisite-disorder that increases from about 5% to 20% with decreasing Si content ($0.9 \leq x \leq 0.5$).

6.3 Magnetic Properties

The magnetic properties were investigated by a super conducting quantum interference device (SQUID, Quantum Design MPMS-XL-5) using nearly punctual pieces of approximately 5 mg to 10 mg of the sample. In Figure 6.2a, the measured total magnetic moments (at 5 K and in saturation) are compared to the Slater-Pauling curve. The magnetic moments can be clearly distinguished in two regions for low and high Si content. In the high Si content region ($x \geq 0.4$), the saturation moments at 5 K decrease linearly with decreasing Si concentration from $5.98\mu_B$ for $x = 1$ to $5.42\mu_B$ for $x = 0.4$. In that region all samples exhibit the $L2_1$ structure and the measured magnetic moments follow the Slater-Pauling curve. Moreover, they fit almost perfectly to the predicted values obtained from LDA+U calculations as reported in [132]. The situation changes in the high Al content region. Below a Si concentration of 40% the magnetic moments are partially much higher than expected from the Slater-Pauling curve. These enlarged values indicate a mixture of the $A2$ and the $B2$ structure. Wurmehl *et al.* calculated the magnetic moments for different kinds of disorder of Co_2FeAl and reported a value of $5.46\mu_B$ for the $A2$ structure [105]. The increase of the magnetic moment in the disordered $A2$ structure emerges mainly from an increase of the magnetic moment of the Co atoms. At the same time the orbital moment is enhanced. The latter effect can be attributed to the loss of the local cubic environment in the disordered structure. It is worthwhile to note that the structural disorder destroys the half-metallic character and results in a dramatic decrease of the spin polarization [106].

Figure 6.2b displays the behavior of the gap in the minority states of $Co_2FeAl_{1-x}Si_x$ with increasing Si content. The minority gap is clearly visible in the calculated density of states as shown in Figure 6.2c for $Co_2FeAl_{0.5}Si_{0.5}$ as an example. Figure 6.2b compares the position of the extremal energies of the states involving the minority band gap that are the accompanied valence band maximum and conduction band minimum. Using LDA+U, the gap has a nearly constant width of 760 meV over the complete series from $x = 0$ to 1. From Figure 6.2b, it is seen that the end-members are just at the borderline to half-metallic ferromagnetism. Starting from $x = 0$, ϵ_F moves from the top of the valence band to the bottom of the conduction band for $x = 1$. For $Co_2FeAl_{0.5}Si_{0.5}$, ϵ_F is located close to the middle of the band gap in the minority states.

6.4 Phase transitions studied by DSC measurements

Differential scanning calorimetry (DSC) was used to find the high temperature phase transitions in the substitutional series. Figure 6.3 displays the dependence of the order-disorder transition temperature as a function of the Si concentration x. The insets display the change of the DSC signal as a function of the temperature using nominal

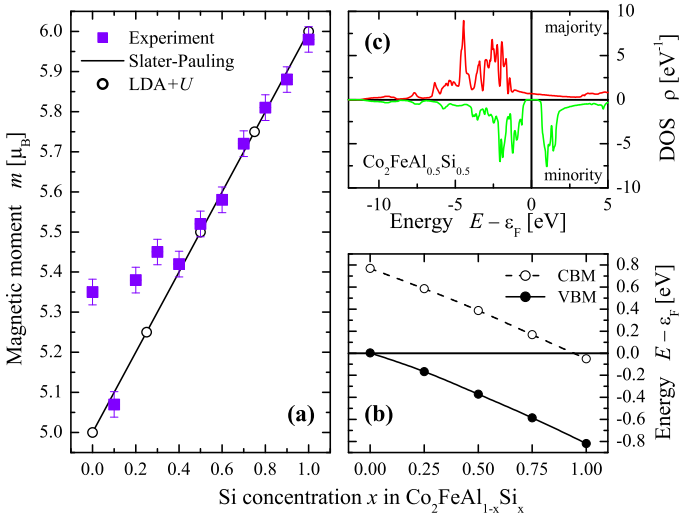

Figure 6.2: Electronic and magnetic structure of $Co_2FeAl_{1-x}Si_x$. **(a)** compares the measured magnetic moments (symbols) to the Slater-Pauling curve (line). **(b)** shows the gap in the minority states with respect to the Fermi energy ϵ_F. Compared are the positions of the valence band maximum (VBM) and the conduction band minimum (CBM). **(c)** shows the density of states (DOS) of $Co_2FeAl_{0.5}Si_{0.5}$ as calculated by means of LDA+U.

heating rates of 15 K min^{-1}. Depending on the temperature rates and the actual amount of material, a shift of the maxima is observed between heating and cooling curves (see also [126]) that is mainly due to an intrinsic hysteresis effect of the method. The length of the vertical bars in Figure 6.3 corresponds to the range of that hysteresis. The signal at the phase transition is rather high for $x > 0.4$ (Fig. 6.3a), that is for compounds exhibiting clearly the $L2_1$ structure. In that case the signal can be clearly attributed to an $L2_1 \leftrightarrow B2$ order-disorder phase transition as also observed in other quaternary Heusler compounds [107, 126]. For $x < 0.4$ the signal is much weaker. Here, XRD indicates mainly a $B2$ structure with a very low portion of $L2_1$ and in some cases a high portion of an $A2$ structure. Therefore, the signal at low x may be attributed either to a $L2_1 \leftrightarrow B2$ or to a $B2 \leftrightarrow A2$ phase transition. Overall, Figure 6.3 demonstrates that the structural transition temperature of the $L2_1$ to the $B2$ phase $T_t^{B2 \leftrightarrow L2_1}$ decreases almost linearly with increasing Si content at least for $x > 0.4$. The results from both, XRD and DSC, demonstrate the better structural stability of the compounds with high Si content. This is expected from the stronger hybridization between Co and Si in these compounds [132]. An important detail is that for $x > 0.5$ the as-cast samples exhibit the $L2_1$ which make the production of thin films much easier because it may avoid extensive heat treatment to achive the correct structure of the samples.

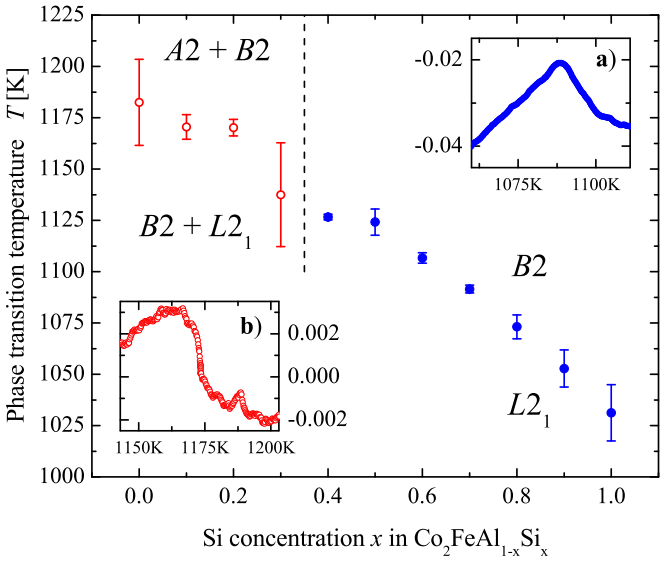

Figure 6.3: Phase transitions in $Co_2FeAl_{1-x}Si_x$. Shown is the composition dependence of the phase transition temperature. The length of the vertical bars corresponds to the experimental hysteresis (see text). The insets (a) and (b) display typical DSC curves in low (0.1) and high (0.7) Si content compounds, respectively.

6.5 Summary and Conclusion

In summary, it has been shown that the series $Co_2FeAl_{1-x}Si_x$ crystallizes for $x \geq 0.4$ in the $L2_1$ structure. This structure is essentially required for a high spin polarization resulting in high magnetoresistive effects. Both, structural and magnetic investigations suggest that the Si rich systems $x > 0.5$ are more stable with respect to the $L2_1$ structure, due to the stronger hybridization between Co and Si compared to Al. For $x \approx 0.5$, calculations predict that the Fermi energy is located in the middle of the gap of the minority states [132] while in Co_2FeSi ϵ_F is located at the bottom of the conduction band which can easily destroy the half-metalicity. This behavior will make $Co_2FeAl_{0.5}Si_{0.5}$ stable against temperature variations. From the combination of experimental (better order for high Si content) and theoretical findings (robust gap at $x \approx 0.5 \pm 0.25$) it is concluded that a compound with an intermediate Si concentration close to $x = 0.5 \ldots 0.7$ would be best suited for spintronic applications, especially for GMR and TMR applications.

7 Spin Injection into Semiconductors

7.1 Introduction

Over the last 40 years, the semiconductor industry has been able to continually shrink the size of electronic components on silicon chips, packing ever more performance into computers. The limits of the current technology are reached, when smaller component sizes are prevented by the fundamental physical laws. In the last decade, spintronics has developed as a new approach that has revolutionized the market for electronic devices. Some predicted advantages of this new technology are the non volatility of data storage, the increased speed of data processing, the high storage density, and the low energy consumption. To exploit the full potential of spintronics, the development of new magnetic materials, magnetic semiconductors, and half-metallic ferromagnets (HMF) is necessary [122]. Half-metallic ferromagnets meet all the requirements of spintronics, as a result of their exceptional electronic structure. These materials behave like metals with respect to the electrons of one spin direction and like semiconductors with respect to the electrons of the other spin direction.

The $C1_b$ compound NiMnSb was one of the early materials being predicted to be a HMF by electronic structure calculations [43]. Two alternative structural descriptions of the $C1_b$ structure (space group $F\bar{4}3m$) are possible. The common description is that the $C1_b$ compounds of composition XYZ (X, Y=transition metals, Z=main-group element) consist of three interpenetrating fcc lattices. From the viewpoint of electronic structures, the most appropriate description of these compounds is a zinc-blende YZ lattice stuffed with X atoms (see Figure 7.1).

In 1984, Kübler found that the Slater-Pauling rule is useful for describing the magnetic properties of the $C1_b$ and $L2_1$ compounds [44]. Jung *et al* [45] recognized that many XYZ compounds can be thought of as comprising X^{n+} ions stuffed in a zinc-blende-type $[YZ]^{n-}$ sublattice, where the number of valence electrons associated with the $[YZ]^{n-}$ sublattice is 18 ($d^{10} + s^2 + p^6$). Such closed-shell 18-electron compounds are nonmagnetic and semiconducting [46, 47]. The prototype for a non ferromagnetic compound is CoTiSb.

Many attempts have been made to prepare semiconducting compounds that also have ferromagnetic properties. Mn-doped GaAs [48] was considered to be a suitable compound, but its Curie temperature is only about 150 K [49] and thus still far away from being suitable for application in electronic devices (see Reference [50] for a recent review). Other materials, like Mn-doped GaN (T_C = 228 to 370 K) [51], V-doped TiO_2 ($T_C \approx 400$ K) [52], p-(Ga,Ni)N ($T_C \approx 300$ K) [53], or Co-doped ZnO ($T_C > 300$ K) [54] come only close to room temperature or need special treatments.

On the other hand, most of the magnetic and half-metallic $C1_b$ compounds contain manganese or a rare earth metal. This is not accidental because, as described by Kübler *et al*[55], the properties of the manganese ions in the Y position of the Heusler compounds

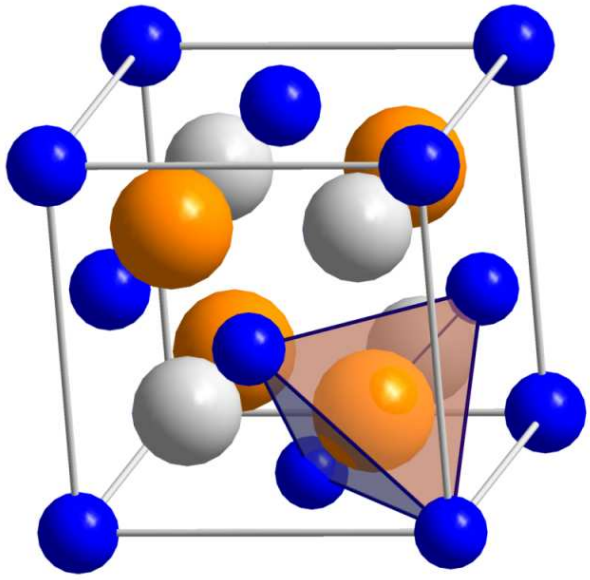

Figure 7.1: Crystal structure of $CoTi_{1-x}Y_xSb$. The Ti (or Y) atoms are placed in the centers of tetrahedra formed by Co.

must be taken into account. These manganese ions, which have an approximate Mn^{3+} configuration, exhibit a highly localized moment in the order of 3 to 4 μ_B. The rare earth ions (RE) in $C1_b$ compounds (for example, RENiSb or REAuSn) also exhibit a charge of +3 and a magnetic moment corresponding to localized f states [56].

This work focuses on the search of suitable compounds that bridge both semiconducting and ferromagnetic properties in almost one material. Therefore samples based on the semiconducting CoTiSb were prepared and investigated both theoretically and experimentally.

7.2 Computational Details

The electronic structure has been calculated for pure and doped $CoTi_{1-x}Y_xSb$ (where Y = Sc, V, Cr, Mn, or Fe) in order to examine their electronic and magnetic properties. Self consistent calculations have been performed by means of the full-relativistic, spin polarized Korringa-Kohn-Rostocker (KKR) method in combination with the coherent potential approximation (CPA) [67, 133]. CPA allows electronic structure calculations for systems with random distribution of the atoms as is here the case where Y substitutes partially Ti.

For the ordered, substitutional compounds, the CPA method has been used to model the statistic distribution of the Y atoms and Ti on a common site of the $C1_b$ crystalline structure. The Co atoms are placed on the 4a Wyckoff position, the Ti atoms are placed together with the Y atoms on the 4c position, and the main group element Sb is finally placed on the 4d position of the cell with $F\,\bar{4}3m$ symmetry. The disordered CoTiSb

Table 7.1: Models for disordered CoTiSb. Given are the site occupation numbers for the four different Wyckoff positions in the $F\,\bar{4}3m$ lattice. The top 3 lines give the swapped and lines 4 to 6 the access or lack structures. The occupancy of the positions by the vacancy ($\diamond$) is always chosen such that the sum of the occupancies is 1.

	4a	4b	4c	4d
Co-Vc	0.9 Co	0.1 Co	Ti	Sb
Ti-Vc	Co	0.1 Ti	0.9 Ti	Sb
Sb-Vc	Co	0.1 Sb	Ti	0.9 Sb
Co access	Co	0.05 Co	Ti	Sb
TiSb lack	Co	$\diamond$	0.95 Ti	0.95 Sb
access / lack	Co	0.05 Co	0.95 Ti	0.95 Sb

compound also has been treated using the CPA method by placing vacancies on regular sites and simultaneously the swapped or accessed part on the 4b Wyckoff position. Six different kinds of disorder have been respected as summarized in Table 7.1.

The calculations have been performed using one of the most common parameterizations of the exchange-correlation functional as given by Vosco, Wilk, and Nussair [70, 71, 72]. Additionally, the generalized gradient approximation (GGA) has been used in the form given by Perdew *et al* [66]. The CPA tolerance has been set to 10^{-4} and the energy convergence criterion to 10^{-5}. f states are included in the basis of all atoms. 578 irreducible k-points based on a $22 \times 22 \times 22$ mesh have been used for integration. The density of states is calculated for the same number of k-points from the Greens function by adding a small imaginary part of 2 mRy to the energy. For smaller values, the band gaps may become better visible, however, at the same time the DOS becomes much more noisy.

7.3 Electronic and Magnetic Structure

The electronic structure has been calculated for pure and doped $CoTi_{0.9}Y_{0.1}Sb$ where Y = Sc, V, Cr, Mn, and Fe using the the full-relativistic, spin polarized Korringa-Kohn-Rostocker (KKR) method in combination with coherent potential approximation (CPA) [67, 133]. CPA allows electronic structure calculations for systems with random distribution of the atoms as is here the case where Y substitutes partially Ti.

The calculated density of states (DOS) are shown in Figure 7.2 and Figure 7.3. For a better comparison the minority states are shown on a negative scale. As predicted by Tobola *et al* [134], CoTiSb is a semiconductor with a gap at the Fermi energy for both spin directions. All calculated densities show principally the same structure. Low lying s states at about 11 eV to 9 eV below the Fermi energy which are separated from the high lying d states by the $C1_b$-typical hybridization gap. The size of this gap amounts typically to $\Delta E \approx 3 \ldots 4$ eV in Sb containing compounds. It indicates the strong covalent bonding between the Ti or Y atoms and the Sb atoms.

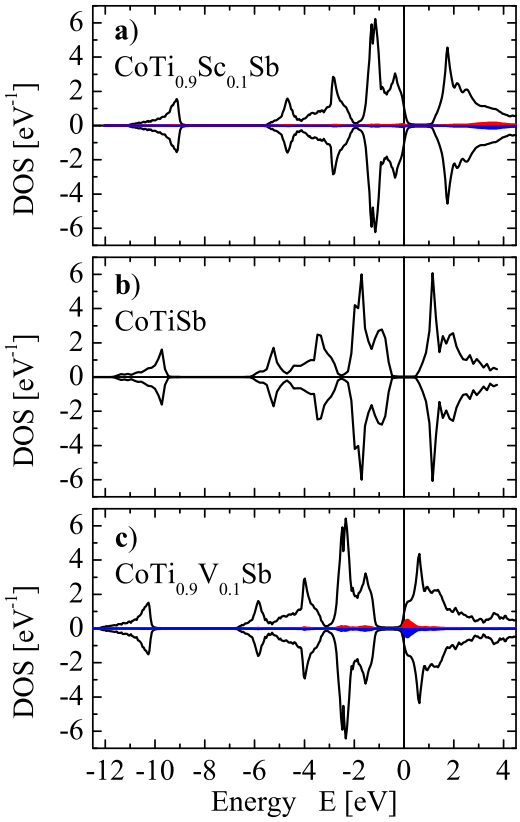

Figure 7.2: Spin resolved density of states of $CoTi_{0.9}Sc_{0.1}Sb$ (a), CoTiSb (b), and $CoTi_{0.9}V_{0.1}Sb$ (c). The additional DOS arising from the Y atom is shown in red (majority) and blue (minority).

While the calculations for $CoTi_{0.9}Sc_{0.1}Sb$ and $CoTi_{0.9}V_{0.1}Sb$ result in semiconducting behavior the calculations show a half-metallic behavior for $CoTi_{0.9}Cr_{0.1}Sb$, $CoTi_{0.9}Mn_{0.1}Sb$, and $CoTi_{0.9}Fe_{0.1}Sb$. Figure 7.2 compares the spin resolved density of states (DOS) of $CoTi_{0.9}Sc_{0.1}Sb$ (a), CoTiSb (b), and $CoTi_{0.9}V_{0.1}Sb$ (c). For CoTiSb the Fermi energy (ϵ_F) is located in the middle of the semiconducting gap. In the case of doping 10% Sc on the Ti position the gap shifts with respect to the Fermi energy to the top of the valence band like in p-type semiconductors. On the other hand if the Ti position is doped with 10% V the gap shifts with respect to the Fermi energy to the bottom of the conduction band like in n-type semiconductors.

The situation changes if doping CoTiSb with more d electrons. Partial replacement of titanium by Cr, Mn, or Fe (10%) has the result that the semiconductor is converted into a HMF: The DOS at the Fermi energy is clearly different from zero for only one spin direction, while remaining zero for the other (see Figure 7.3). An interesting observation is that the half-metallicity has different reasons in the three different cases. In the $CoTi_{0.9}Cr_{0.1}Sb$ case the Cr $3d$ states fill up directly the gap at ϵ_F in the majority

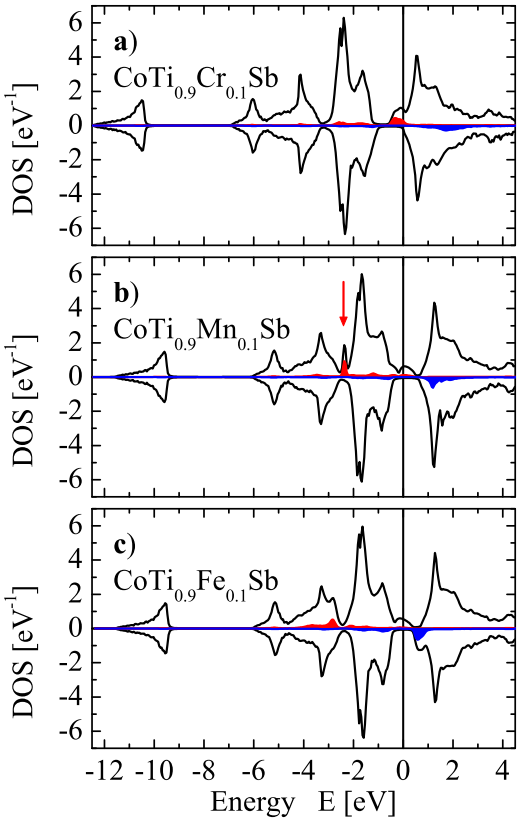

Figure 7.3: Spin resolved density of states of $CoTi_{0.9}Cr_{0.1}Sb$ (a), $CoTi_{0.9}Mn_{0.1}Sb$ (b), and $CoTi_{0.9}Fe_{0.1}Sb$ (c). The additional DOS arising from the Y atom is shown in red (majority) and blue (minority).

channel while in the $CoTi_{0.9}Mn_{0.1}Sb$ case the localized Mn $3d$ states fill the band gap at approximately 2.5 eV below ϵ_F in the majority channel. This Mn $3d$ states shift the Co states from the valence band into the gap. If doping CoTiSb with 10% Fe the calculation shows a similar result. The Fe $3d$ states are localized at approximately 3 eV below ϵ_F - note that the Fe $3d$ states are not filling up the band gap like the Mn states in $CoTi_{0.9}Mn_{0.1}Sb$ - and therefore the Co states are shifted into the gap. In all three cases the doping does not effect the minority band gap. In the minority channel the additional states are located well above ϵ_F which results in a clear and stable band gap.

A further, important result of the calculations is that only those Fe atoms replacing Ti contribute to the total magnetic moment of the compound. Fe atoms on Co positions or in vacant tetrahedral holes do not contribute to the magnetic moment at all. This was verified by X-ray magnetic circular dichroism measurements as reported in [135]. The calculated value of the magnetic moment per iron atom in the Ti position changes slightly with increasing Fe concentration from 3.4 μ_B (at 5%) to 3.7 μ_B (at 10%).

Figure 7.4 compares the calculated number of d-electrons on the Y-site form $CoTi_{0.9}Y_{0.1}Sb$

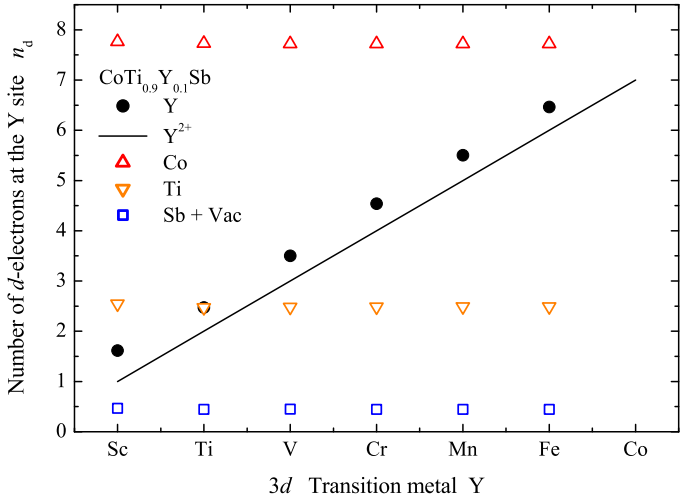

Figure 7.4: Number of d-electrons on the Y-site of $CoTi_{0.9}Y_{0.1}Sb$ where Y = Sc, Ti, V, Cr, Mn, and Fe.

where Y = Sc, Ti, V, Cr, Mn, and Fe. The results show no dependence in the number of d-electrons on the doping element for Co, Ti, Sb, and the vacancy position. On the Co-site there are formally 7.75 d-electrons while there are 2.5 and 0.45 d-electrons on the Ti-site and the Sb-site including the vacancy, respectively. The number of d-electrons on the Y site increases indeed linearly with the 3d transition metal Y. There are approximately 0.5 d-electrons more on the Y-site than expected from a Y^{2+} ion. This results exclude charge-transfer effects and point certainly on localized moments on the Y-sites. This is obvious, in particular for Mn (see Figure 7.3 (b)), where a sharp feature appears in the minority states.

7.4 Structural Properties

$CoTi_{1-x}Y_xSb$ (Y = V, Cr, Mn, or Fe) samples have been prepared and it was carefully proved that the Y atom occupies the Ti positions and not an other vacant site. For that purpose, the X-ray powder diffraction patterns of the substituted compounds were compared to that of pure CoTiSb. It was observed that no additional diffraction reflexes appear up to 10% Y-doping. This confirms that the structure remains the same as of pure CoTiSb, that is $C1_b$. The diffraction patterns of pure and 10% Fe and Mn and 5% Cr and V doped samples are compared in Figure 7.5. The change of th lattice parameter $a = 5.886$ Å for CoTiSb is small ($\approx 0.2\%$) if 10% of Ti is replaced by any of the Y atoms as expected due to the similar radii of the $3d$ transition metals. This is a very important result if thinking about preparing thin film devices including these materials due to their very low lattice mismatch among each other. It should be possible to grow them epitaxially with clean and smooth interfaces. If depositing layer by layer one can use

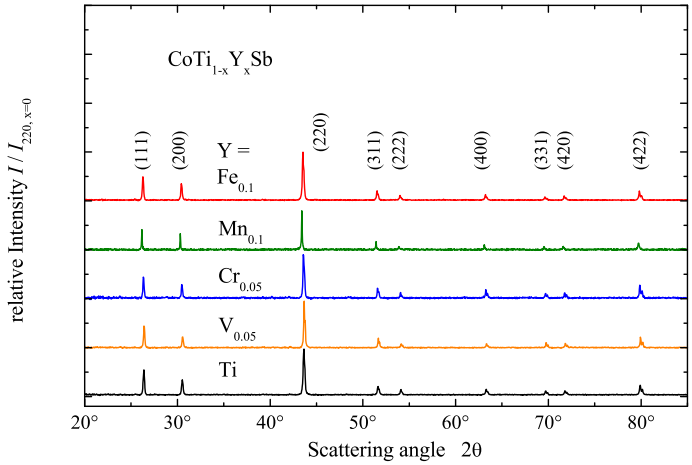

Figure 7.5: XRD spectra for $CoTi_{1-x}Y_xSb$ where Y = Ti, V, Cr, Mn, and Fe. The spectra were excited by Cu K_α radiation

the Co-planes to merge the different materials without any interface at all.

The R values for the best fits in the Rietveld refinement are $R_i = 6\%$ and $R_p = 11\%$ confirming the high degree of site order of the samples. It should be noted that the structure was hardly stabilized in the correct $C1_b$ structure for Mn substitution.

The structural parameter of CoTiSb has been investigated in dependence of the temperature between 20 K and 300 K. Figure 7.6 shows the temperature dependency of the cell volume $V = a^3$ of the cubic cell. The Volume decreases by about 0.5% if the temperature is lowered from room temperature to 20 K. The change of the cell volume with temperature is clearly non-linear and evidence is given that the volume increases with an approximate T^2 law.

Further, iron doped $CoTi_{0.9}Y_{0.1}Sb$ samples were investigated by means of transmission electron microscopy (TEM) in order to prove the homogeneity of the sample. Uniform TEM images were observed and, in particular, no Fe clusters were detectable. Figure 7.7 shows a typical diffraction pattern taken at 120 keV exhibiting the cubic structure of the compound.

7.5 Magneto-structural Properties

^{57}Fe Mößbauer spectroscopy was performed in transmission geometry using powder samples. The Mößbauer spectrum (see Figure 7.8) of the sample with $x = 0.1$ comprises a small singlet line (yellow) and a more intense magnetic sextet (blue). The ferromagnetic sub-spectrum is explained by Fe atoms on Ti positions of the $C1_b$ structure in accordance with the electronic structure calculations. It exhibits an isomer shift of about 0.1 mms^{-1}. The low intense, singlet corresponds to Fe atoms occupying either voids or

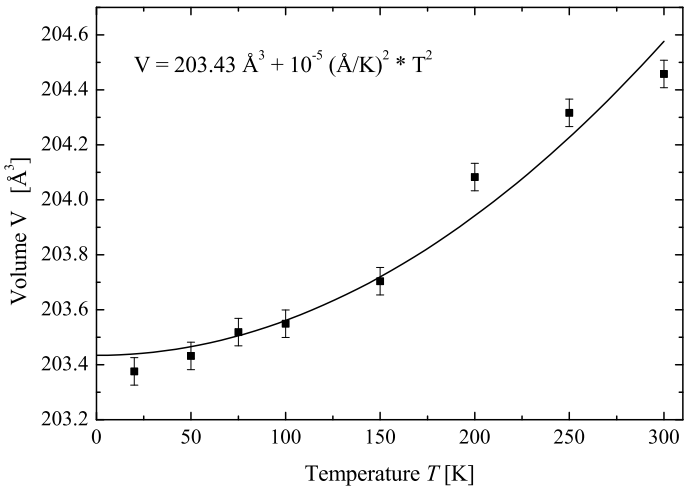

Figure 7.6: Temperature dependency of the cubic cell volume V for CoTiSb. The fit of the data to a T^2 dependence is shown as a full line.

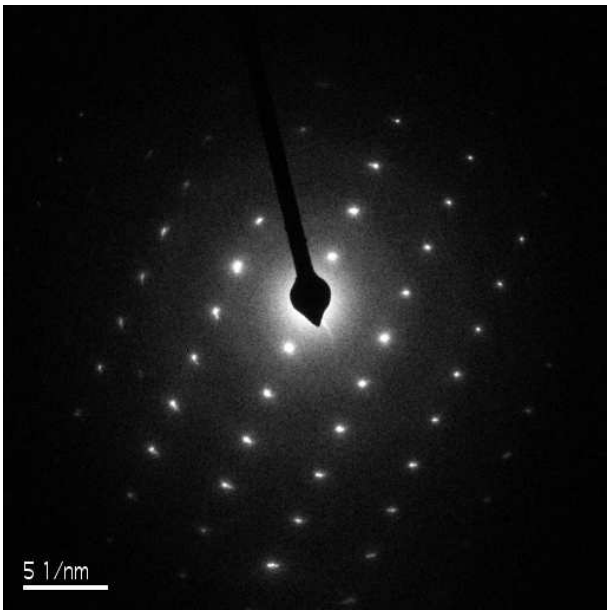

Figure 7.7: Transmission electron microscopy image of $CoTi_{0.9}Y_{0.1}Sb$. The TEM diffraction pattern shows the cubic symmetry of the sample

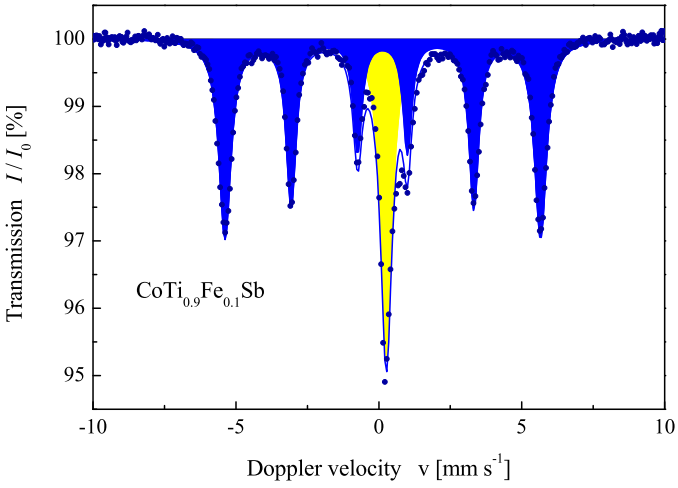

Figure 7.8: Mößbauer spectrum of iron in $CoTi_{1-x}Fe_xSb$.

Co positions. Overall, Mößbauer spectroscopy gave clear evidence that the Fe atoms occupy Ti sites and do not form a separate Fe phase. The observed hyperfine field (H_{hff} = 27.53 MAm^{-1} at 4.2 K for 10% Fe substitution) exceeds clearly the value of α-Fe (26.85 MAm^{-1}), such that the appearance of Fe clusters can be excluded. T he values at lower iron concentrations of 1% and 5% are 27.07 MAm^{-1} and 27.24 MAm^{-1}, respectively. The hyperfine field is lowered by about 2% if the temperature is raised from 4.2 K to 300 K in agreement to the high Curie temperature of the alloy.

7.6 Magnetic Properties

If the $C1_b$ compounds are half-metallic ferromagnets, then they will show a Slater-Pauling behavior for the magnetization, meaning that the saturation magnetization scales with the number of valence electrons [81, 83, 45]. The magnetic moment per unit cell (in multiples of the Bohr magneton μ_B) is given by:

$$m = N_V - 18, \tag{7.1}$$

with N_V denoting the accumulated number of valence electrons in the unit cell. For CoTiSb there is a total of $9 + 4 + 5 = 18$ valence electrons in the unit cell which results in no magnetic moment at all.

Low temperature magnetometry has been performed by means of the SQUID to investigate the dependence of the dopants on the magnetic properties and to compare the results with the calculated saturation moments. Selected results are shown in Figure 7.9.

The total magnetic moments, measured at 5 K and in saturation, are 0.32 μ_B, 0.30 μ_B, and 0.02 μ_B for $CoTi_{0.9}Fe_{0.1}Sb$, $CoTi_{0.9}Mn_{0.1}Sb$, and $CoTi_{0.9}Cr_{0.1}Sb$ respectively for

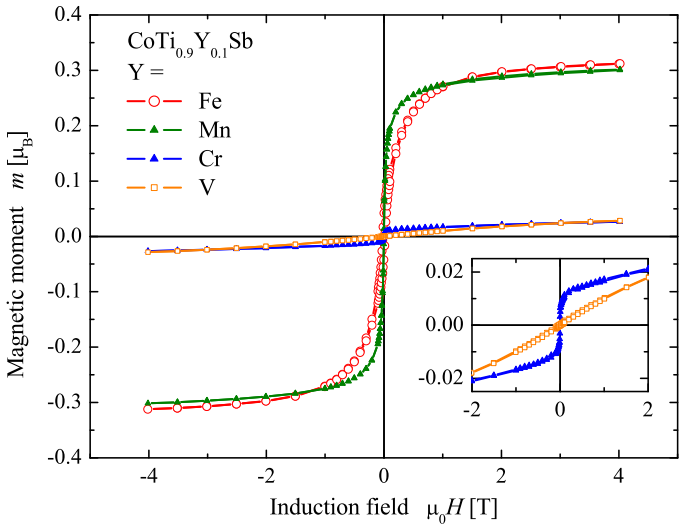

Figure 7.9: Magnetic moments for $CoTi_{1-x}Y_xSb$ where Y = V, Cr, Mn, and Fe. The data for the Cr and V doped samples are shown in the inset on an enlarged scale.

the ferromagnetic samples. The pure CoTiSb shows a diamagnetic behavior while the V doped sample is paramagnetic. Figure 7.10 displays the dependence of the saturation moment as a function of the Y atom and compares the calculated moments with the experimental results.

The experiments confirm the calculations which result in ferromagnetic samples in the case of $CoTi_{0.9}Fe_{0.1}Sb$, $CoTi_{0.9}Mn_{0.1}Sb$, and $CoTi_{0.9}Cr_{0.1}Sb$ but remain non-magnetic for $CoTi_{0.9}V_{0.1}Sb$, and $CoTi_{0.9}Sc_{0.1}Sb$. To distinguish the Curie temperatures of the compounds high temperature magnetometry has been performed up to 800K. The Curie temperature of $CoTi_{0.9}Fe_{0.1}Sb$ is higher than 700 K, where the onset of decomposition of the alloy has been observed (see Reference [135]) while the transition temperature in the Cr doped compound is around 60K.

For site specific magnetometry, X-ray Magnetic Circular Dichroism (XMCD) in photo absorption spectroscopy was performed at the *First Dragon* beamline of NSRRC (Hsinchu, Taiwan). Figure 7.11 proofs that a XMCD signal was only detectable at the Fe $L_{2/3}$ edges in agreement with the theoretical predictions. It should be noted that the sample magnetization was not saturated in the XMCD measurement due to limitations of the experimental setup. The spin magnetic moment, as determined from a sum-rule analysis, amounts to $m_s = 0.68\ \mu_B$ under the experimental conditions ($T = 300$ K, $\mu_0 H = 0.36$ T). The orbital to spin magnetic moment ratio amounts to $m_l/m_s = 0.09$. This value is in good agreement with calculations for Fe atoms substituting Ti atoms.

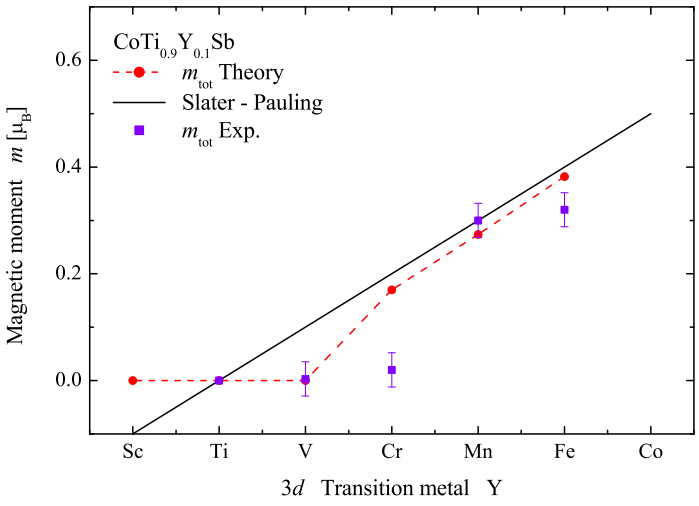

Figure 7.10: The calculated and measured magnetic moments of $CoTi_{0.9}Y_{0.1}Sb$ where Y = Sc, Ti, V, Cr, Mn, and Fe. The Slater-Pauling expect is shown for comparison.

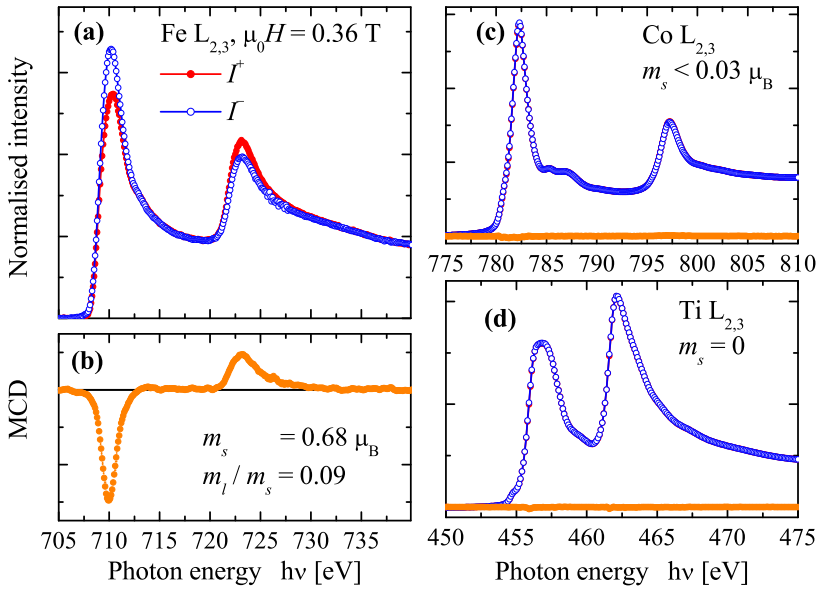

Figure 7.11: Magnetic properties of $CoTi_{0.95}Fe_{0.05}Sb$. Shown are the X-ray absorption spectra taken with opposite magnetization and fixed photon helicity at the Fe $L_{2,3}$ (a), Co $L_{2,3}$ (c), and Ti $L_{2,3}$ (d) edges and the consequential magnetic circular dichroism for Fe (b).

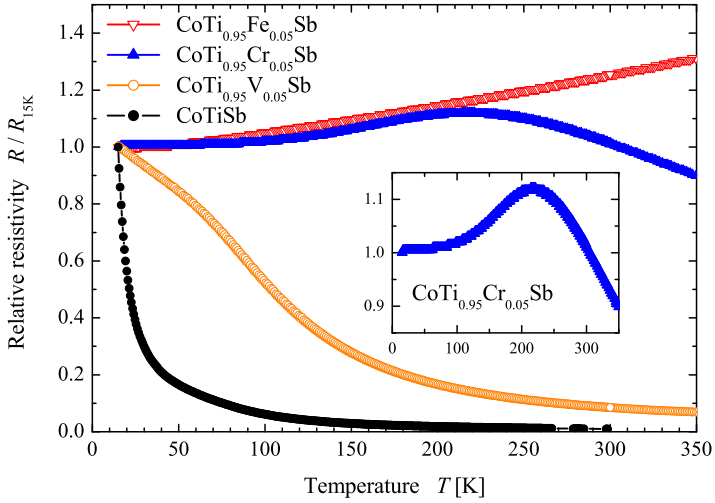

Figure 7.12: Temperature dependence of the resistivity for CoTiSb, $CoTi_{0.95}V_{0.05}Sb$, $CoTi_{0.95}Cr_{0.05}Sb$, and $CoTi_{0.95}Fe_{0.05}Sb$. The inset shows the result for $CoTi_{0.95}Cr_{0.05}Sb$ on an enlarged scale.

7.7 Electric Properties

To approve the predictions from the electronic structure calculations measurements of the resistivity were done. Figure 7.12 displays the temperature dependence of the resistivity for pure CoTiSb, $CoTi_{0.95}V_{0.05}Sb$, $CoTi_{0.95}Cr_{0.05}Sb$, and $CoTi_{0.95}Fe_{0.05}Sb$ from 15 K to 350 K. The pure CoTiSb and $CoTi_{0.95}V_{0.05}Sb$ show semiconducting behavior while $CoTi_{0.95}Fe_{0.05}Sb$ is metallic and $CoTi_{0.95}Cr_{0.05}Sb$ undergoes a metal to semiconductor transition with a transition temperature of $T_t \approx 210\ K$.

This observations can be explained if considering the number of d-electrons which were doped in the semiconducting CoTiSb. If doping just 5% Vanadium instead of Titanium there are not enough d-electrons to obtain a conducting sample. But if doping 5% Iron instead of Titanium there are now enough d-electrons to end up in a metallic behavior. In the Cr-doped sample there is an intermediate situation. The sample is metallic at low temperature and becomes semiconducting at about $T_t \approx 210\ K$.

From the measurements one can estimate the semiconducting gap ΔE from

$$ln(\sigma) = C - \Delta E/2k_B \times 1/T, \tag{7.2}$$

where σ is the conductivity and C a constant. The calculation for CoTiSb results in a gap of $\Delta E \approx 9\ meV$. This value is the same as reported recently by Stadynk *et al* [136]. For $CoTi_{0.95}V_{0.05}Sb$ a gap of $\Delta E \approx 3\ meV$ has been calculated.

One possibility of the small size of the gap might be the occurrence of structural defects being related to the vacancy of one of the positions in the unit cell. To explain the discrepancy between the calculated gap with a size of $\approx 1\ eV$ and the one obtained from the resistivity measurements, the electronic structure was re-calculated assuming

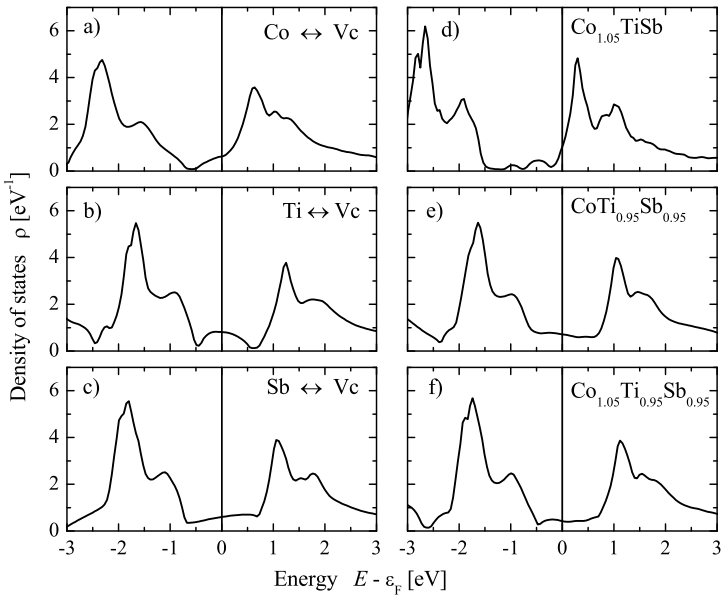

Figure 7.13: Density of states for different kind of disorder of CoTiSb. The panels a) to c) show the DOS for the swapped structures and panels d) to f) for access or lack structures. The site occupation numbers are given in Table 7.1.

different kinds of disorder. Six different kinds of disorder have been respected as summarized in Table 7.1. Figure 7.13 shows the results of those calculations. If assuming disorder between Ti (Figure 7.13 (b) or Sb (Figure 7.13 (c)) and the vacancy position or lack of Ti and Sb (Figure 7.13 (e) and (f)) the gap is completely smeared out which would result in metallic behavior of the sample. In case of assuming disorder between Co (Figure 7.13 (a) and the vacancy position or an access of Co (Figure 7.13 (d) the remaining gap is filled up with states and shifted with respect to the Fermi energy. From this calculations the most probable type of disorder to explain the small band gap is the access of Co atoms on the vacancy position. This agrees with the XRD data where this type of disorder is the only possibility to enhance the quality of the Rietveld refinement.

7.8 Photo Emission Spectroscopy

Using photo emission spectroscopy one obtains information about the occupied electronic states. The dispersion of the bands may be studied by spin and angular resolved UPS. This needs, however, well ordered surfaces of single crystals. For the interpretation one has to take into account that usually the kinetic energy of the photo emitted electrons is in a range where the mean free path is only a few Å and the method therefore mainly shows electronic bands very close to the surface layer.

Using higher photon energy for excitation (and thus kinetic energies of the photo electrons), it is possible to study the density of states, in particular for polycrystalline

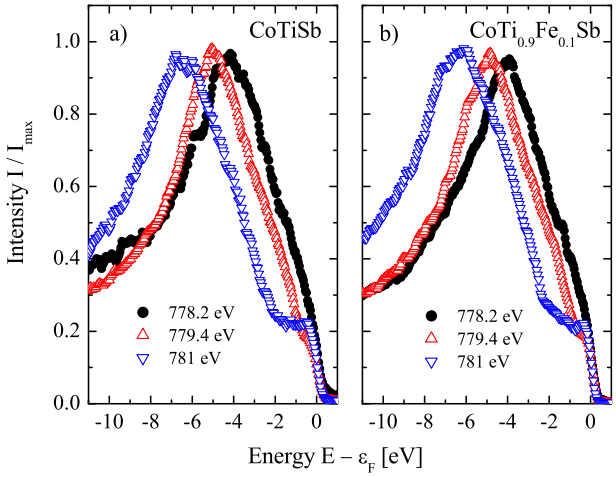

Figure 7.14: Valence band spectra taken at different excitation energies around the Co L_3 edges of CoTiSb (a) and $CoTi_{0.9}Fe_{0.1}Sb$ (b).

samples. Making use of resonant excitation one expects to become more bulk sensitive [137] and may be able to distinguish the site specific contributions.

Figure 7.14 shows the energy dependence of the valence band photo emission spectra taken with photon energies close to the Co L_3 edge for CoTiSb (Figure 7.14(a)) and for $CoTi_{0.9}Fe_{0.1}Sb$ (Figure 7.14(b)). The spectra are normalized to the photon flux. The photon energies correspond to the onset of the absorption (778.2 eV), the maximum of the Co L_3 white line (779.4 eV), and the trailing edge of the Co L_3 absorption (781 eV). For the complete absorption spectrum see Reference [135].

The most prominent feature seen in the spectra is the Co Auger electron emission. The L_3VV Auger electron emission is observed just when the onset of the Co L_3 absorption edge is reached. It can be clearly identified from its linear energy dependence (see Figure 7.14). On a kinetic energy scale it stays fixed. Due to the intrinsic width of the Auger transition it is difficult to observe details of the valence band structure.

Nevertheless, comparing the valence band spectra of CoTiSb and $CoTi_{0.9}Fe_{0.1}Sb$ (see Figure 7.15(a)) in detail a slightly higher Auger transition intensity is observed for CoTiSb in comparison to the Fe doped sample. Figure 7.15(b) shows the spectra of CoTiSb and $CoTi_{0.9}Fe_{0.1}Sb$ close to the Fermi level for a better comparison on a larger scale. The Ag Fermi edge as used for the energy calibration of the spectrometer is shown for comparison. Close to the Fermi energy a slightly higher intensity for the Fe doped sample in comparison to the pure CoTiSb is observed. This behavior is compatible with the electronic band structure calculations which predict a higher density close to the Fermi level for $CoTi_{0.9}Fe_{0.1}Sb$. Indeed, the valence band spectra hint on a metallic like characteristic for both samples. If present, a semiconducting gap with a width of below 100 meV can not be excluded. Antimony is a well known surfactant, therefore the metallic like character may also be explained by a few monolayer thick, conducting

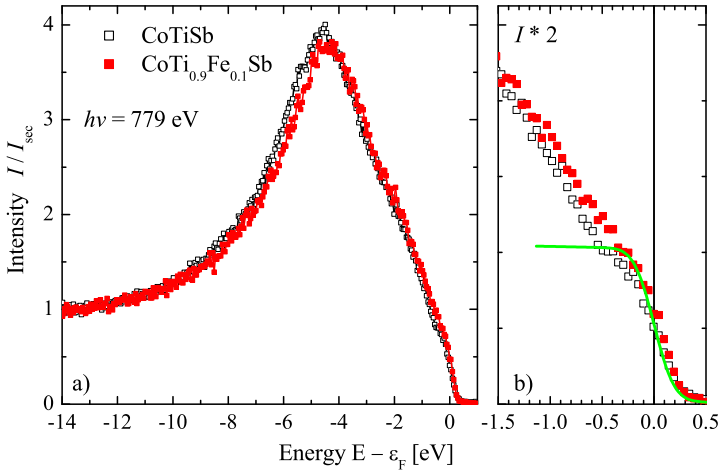

Figure 7.15: Valence band spectra of CoTiSb and $CoTi_{0.9}Fe_{0.1}Sb$ at 779 eV excitation energy. Panel (a) shows the complete spectra while panel (b) shows an enlarged view of the area around the Fermi energy. The spectra are shown in comparison to the fitted Ag Fermi level (dotted line).

Sb layer on top of the surface. The occurrence of a very narrow gap is, however, also supported by the conductivity measurements (see Section 7.7).

Due to the high intense Auger transition governing the spectrum an additional analysis is needed. Therefore, hard X-ray photo emission spectroscopy with high bulk sensitivity has been performed.

The partial, atomic resolved (p) and the orbital (l) resolved densities of states for $CoTi_{0.9}Fe_{0.1}Sb$ (see Figure 7.16 (a) and (b)) and the energy and l dependence of the cross section of the valence states of atomic Co, Ti, Fe, and Sb were calculated to compare the measurement with calculations. The p-DOS of the vacancy as well as the l-DOS for higher angular momenta (l) are omitted as they contribute only very few to the total density of states. The main contribution to states close to the Fermi energy are d states being located at the Co site.

The peak in the density at about 3 eV below ϵ_F is due to the contribution of the Fe $3d$ states. The smaller peak at about -5 eV is due to $s-p$ hybridization. The orbital momentum and site resolved cross sections are displayed in Figure 7.16 (c)-(f). The calculations were performed for atomic valence states using a modified full relativistic Dirac-solver based on the computer programs of Salvat and Mayol [138, 139]. The radial integrals for the various transitions have been computed using the dipole length-form. In particular, the cross section for d states decreases faster with increasing photon energy than the ones of the s or p states.

Both measured high energy spectra reveal clearly the low lying s states at about 11 eV to 9 eV below the Fermi energy, in well agreement to the calculated DOS, see Figure 7.17. These low lying bands are separated from the high lying d states by the $C1_b$-typical

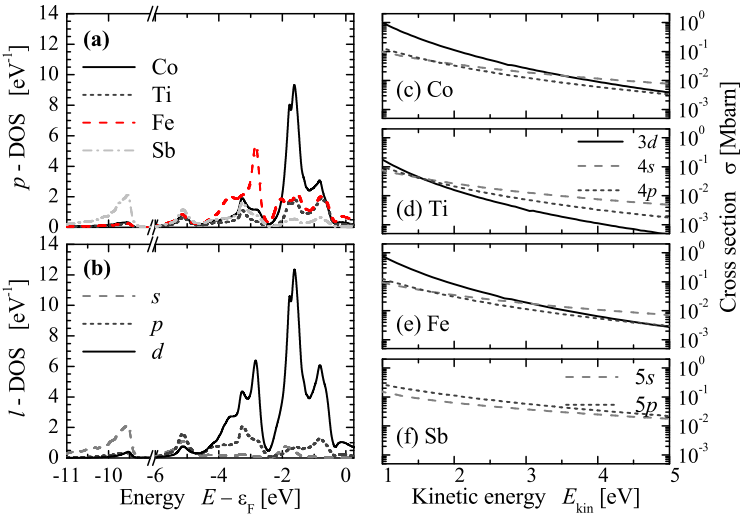

Figure 7.16: Partial and orbital recall for $C1_b$ compounds with T_d symmetry, one finds a strong bonding interaction between transition metal d states (t_{2g}) with Sb p-solved densities of states and photo emission cross sections. Shown are the atomic resolved p-DOS in (a) and the orbital momentum resolved l-DOS in (b). (Note the axis break between -9 eV and -6 eV that was used to bridge the low lying hybridization gap.) Panels (c)-(f) show the calculated energy and l dependence of the cross section of the valence states of atomic Co, Ti, Fe, and Sb.

hybridization gap being clearly resolved in the spectra as well as the calculated DOS. The size of this gap amounts typically to $\Delta E \approx 3 \ldots 4$ eV in Sb containing compounds.

The structure of the high energy spectra in the range of the d states agrees roughly with the structures observed in the total DOS although the high density at -5 eV and -3 eV is not well resolved. Overall the emission from the d states covers a larger energy range compared to the calculated DOS, what gives advice on an underestimation of correlation effects in the local density approximation. However, one also has to account for lifetime broadening and the experimental resolution if comparing that energy range. At 2.5 keV excitation energy, the emission is still dominated by the high dense d states at about -1.5 eV.

The big difference in the measured valence band between the pure CoTiSb and the Fe doped sample is obviously the additional peak at around 3 eV below the Fermi energy. This peak can only be explained with the additional Fe 3d states in this region of the valence band as shown in Figure 7.16 (a) and as well in Figure 7.17 where the calculated DOS of $CoTi_{0.9}Fe_{0.1}Sb$ for a better comparison with the experiment is weighted by the partial photo emission cross sections of 2.5 keV excitation energy and additionally broadened by a Gaussian of 0.25 eV width to account roughly for the experimental resolution at 2.5 keV excitation energy. However, a semiconducting band gap of CoTiSb within a width of 100 meV can not be detected at the given energy resolution of the

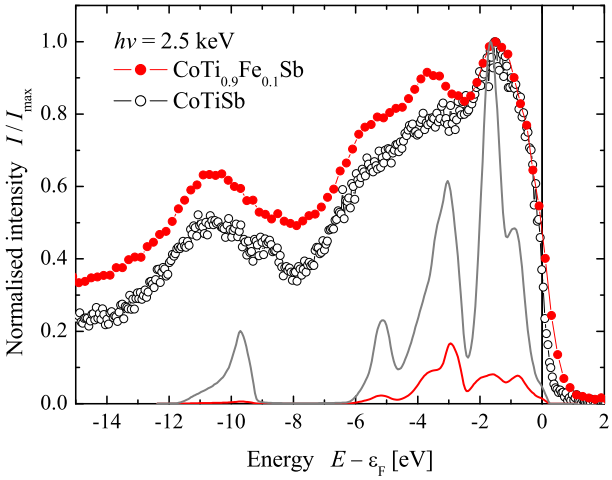

Figure 7.17: High energy valence band spectra of CoTiSb and $CoTi_{0.9}Fe_{0.1}Sb$. Shown are spectra taken at 2.5 keV excitation energy (symbols) and the DOS of $CoTi_{0.9}Fe_{0.1}Sb$ weighted by the photo emission cross section (lines). The additional DOS arising from the Fe atom is shown in red.

spectra.

7.9 Summary and Conclusion

The pure and doped $C1_b$ compounds $CoTi_{1-x}Y_xSb$ where Y = Sc, Ti, V, Cr, Mn, and Fe were synthesized and investigated both experimentally and theoretically. The band structure calculations predicted for $CoTi_{0.9}Sc_{0.1}Sb$ and $CoTi_{0.9}V_{0.1}Sb$ semiconducting behavior and half-metallic behavior for $CoTi_{0.9}Cr_{0.1}Sb$, $CoTi_{0.9}Mn_{0.1}Sb$, and $CoTi_{0.9}Fe_{0.1}Sb$. The measurements of the electric resistivity approved this predictions. The pure CoTiSb and $CoTi_{0.95}V_{0.05}Sb$ show semiconducting behavior while $CoTi_{0.95}Fe_{0.05}Sb$ is metallic and $CoTi_{0.95}Cr_{0.05}Sb$ undergoes a metal to semiconductor transition with a transition temperature of $T_t \approx 210\ K$. The XRD data verified the $C1_b$ structure for all samples and show a very low lattice mismatch among each other. This result makes this doping series interesting for spintronics applications like Spin-LEDs or other spin injection devices. One could prepare thin film devices including these materials and it should be possible to grow them epitaxially with clean and smooth interfaces. If depositing layer by layer one can use the Co-planes to merge the different materials without any interface at all.

The electronic structure of the CoTiSb and $CoTi_{0.9}Fe_{0.1}Sb$ has been investigated by means of photo emission spectroscopy. In particular the HAXPES spectra agree with the calculated density of states and show the difference between the pure compound and the Fe-doped compound. The additional Fe $3d$ states could observed at around 3 eV below the Fermi energy.

8 Spin Torque Transfer Application

8.1 Introduction

In the quest for creating magnetic random access memory following the semiconductor roadmap ($\approx$ 20 nm node in 2010), spin momentum transfer is considered to be the likely mechanism for switching the magnetization of the so-called free magnetic layers storing the bit information in each storage cell [140]. In 1996, Berger [141] and Slonczewski [142] predicted the possibility of current induced magnetic switching processes. A few years after the theoretical predictions several groups verified the effect experimentally and started initial investigations of those processes in GMR-devices [143, 144, 145, 146, 147]. Later, spin transfer switching was also observed in magnetic tunnel junctions (MTJ) [148, 149]. MTJs are suggested to be better suited for devices than GMR-elements based on metallic multilayers because of a large tunneling magnetoresistance (TMR) ratio and a small spin transfer switching current.

One of the critical issues for applications is the current density needed for stable switching using the spin transfer torque mechanism. At present, this current density is order of 2-3 MAcm^{-2} [150, 151]. New materials are needed to achieve a stable switching at significant lower values. Such materials must have a high spin polarization, a high Curie temperature and a low magnetic moment. Furthermore, the direction of the magnetization must be thermally stable at room temperature. It is evident that compensated ferrimagnets are suitable materials. They exhibit a high stability against thermal switching at moderate coercitive fields. Ochiai *et al.* [152] have demonstrated that a synthetic antiferromagnetic layer used for exchange biasing of the free layer is able to reduce the critical current density. In principal, the result is a local (layer-wise) ferrimagnetic order. A reduction of the the switching current density by one order of magnitude was also observed if applying exchange biasing to the fixed layer [153]. Both effects suggest that an enhancement of the spin transfer effect may also be reached in real ferrimagnets, although the situation of the spin moments may be more complicated [154].

The Mn-Ga alloys show a manifold of stable phases and $Mn_{75}Ga_{25}$ (corresponding to Mn_3Ga) was reported to exist in a cubic face centered structure [155]. Wurmehl *et al.* [156] predicted that Mn_3Ga becomes a half-metallic completely compensated-ferrimagnet in the cubic DO_3 Heusler-type phase. However, in experiments it turned out that the cubic phase of Mn_3Ga is not stable. In 1970, Kren and Kadar [157] synthesized the hexagonal high temperature DO_{19} phase of $Mn_{2.85}Ga_{0.15}$ and investigated the crystal and magnetic structure by neutron diffraction. With annealing at 750 K of this triangular anti-ferromagnetic structure they observed a tetragonal DO_{22} phase which is ferrimagnetic with magnetic moments of -2.8 μ_B for Mn_I and 1.6 μ_B for Mn_{II}. Niida *et al.* [158] investigated the complete series $Mn_{3-\delta}Ga$ but single phase DO_{22}-type samples could only be obtained for a composition range of $0.15 \leq \delta \leq 1.16$. With a new

approach of ab initio electronic structure calculations Kübler [159] calculated the Curie temperature of Mn_3Ga in the tetragonal DO_{22} structure to be $T_C = 762$ K.

In the following, details of the electronic, magnetic, and structural properties of Mn_3Ga will be reported. First, the electronic and magnetic structure as calculated by ab-initio methods will be discussed. Afterwards, the experimental results will be presented and the structural and magnetic properties will be discussed.

8.2 Computational Details

Self-consistent electronic structure calculations have been performed to explain the electronic and magnetic properties of the compound. The calculations have been carried out by means of the (FLAPW) method as provided by Wien2k [65]. The exchange-correlation functional was taken within the GGA in the parametrization of Perdew *et al* [66]. A base, $25 \times 25 \times 25$ mesh was used for integration. The mesh corresponds to 1183 k-points in the irreducible wedge of the Brillouin zone. The properties of Mn_3Ga were calculated in $I\,4/mmm$ symmetry using optimized lattice parameters. In this structure type, the Mn atoms occupy two different positions. The first (Mn_I) with the multiplicity one is located at (0,0,1/2) and the second (Mn_{II}) with multiplicity two at (0,1/2,1/4). The Ga atom is positioned at (0,0,0). The structural optimization has been done by variation of the volume as well as the c/a ratio. The structural parameters minimizing the total energy were found to be: $a = 3.77$ Åand $c = 7.16$ Å. No essential changes of the electronic and magnetic structure were obtained when the calculations were performed for the experimental lattice parameter as reported below.

8.3 Electronic Structure

The calculations result in a ground state with ferrimagnetic order. The spin magnetic moments found in the calculations are -2.896 μ_B for Mn_I and 2.355 μ_B for Mn_{II}. Including the interstitial space and the Ga sites, this results in a total moment of 1.77 μ_B in the primitive cell due to the partial compensation of the moments from the Mn atoms on the two different sites.

Figure 8.1 shows the spin resolved band structure and density of states (DOS) for Mn_3Ga. In the majority states, few valence states are above the Fermi energy ϵ_F close to the high symmetry points (Γ, X) and just one d-band crosses (ϵ_F) in the Γ-A direction. This band is strongly dispersing and contributes mainly to the small density in the pseudo-gap of the majority states. The situation is different in the minority channel. Several flat d-bands are located close to ϵ_F and cross it in all high symmetry direction. This particular behavior suggests that there is a strong difference in the conductivity for the minority and the majority electrons. Following the classification of Coey *et al.* [21], the tetragonal Mn_3Ga is a type III half-metal, where the electron current will be carried through itinerant majority and localized minority electrons. The calculated spin polarization at the Fermi level amounts to 88 %, and is comparably higher than the one calculated for $Fe_{1-x}Co_x$ alloys.

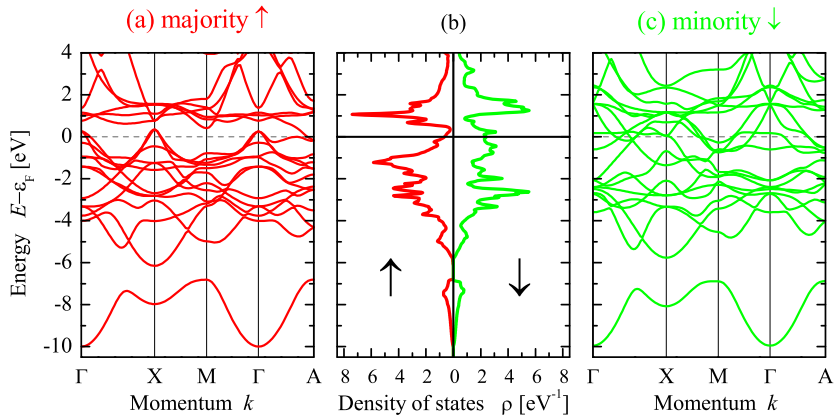

Figure 8.1: Electronic structure of Mn_3Ga. Shown are the band structures for the minority (a) and majority (c) electrons together with the spin resolved density of states (b).

8.4 Structural Properties

Mn_3Ga samples were prepared by arc melting and annealed at 673 K in an evacuated quartz tube for 7 days. This procedure resulted in samples exhibiting the DO_{22} structure (space group: $I\,4/mmm$). The crystalline structure was determined by X-ray powder diffraction (XRD) using excitation by Mo K_α radiation. The lattice parameters found from a Rietveld-refinement are $a = 3.90416$ Å and $c = 7.08820$ Å (see Figure 8.2). These values result in an about 5% larger cell volume compared to the calculated one.

The crystal structure of Mn_3Ga was additionally investigated in dependence of the temperature at the D10B-XPD beamline of the Brazilian Synchrotron facility LNLS (Campinas). The crystal structure was recorded in a temperature range from 25 K to 300 K using excitation by radiation of a wavelength of 1.75866 Å. Figure 8.3 shows the temperature dependency of the lattice parameter a, the volume of the tetragonal unit cell V and the c/a ratio.

The lattice parameter a and the cell volume V decrease linearly with decreasing temperature. The lattice parameter c, which is not shown in Figure 8.3, exhibits also a linear decrease upon reduction of the temperature. However, the c/a ratio increases with decreasing temperature (see Figure 8.3 (c)) due to the fact that the lattice parameter c grows stronger than the lattice parameter a, with decreasing temperature. This means that the tetragonal unit cell of Mn_3Ga becomes more cubic with increasing temperature.

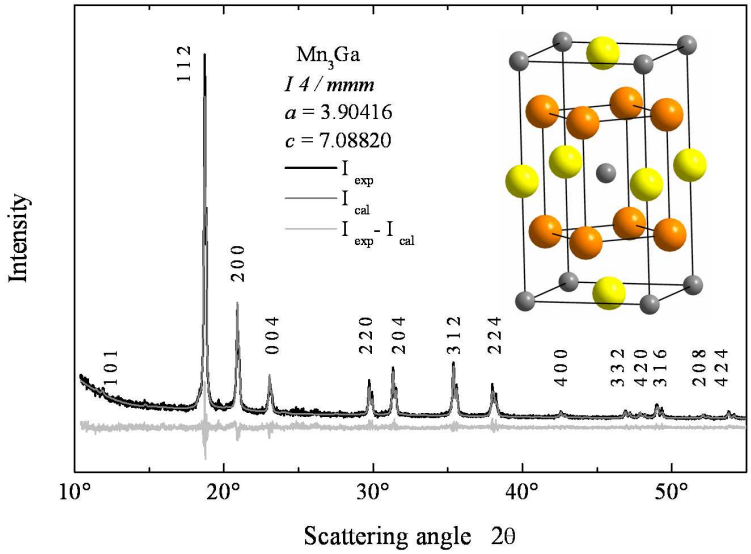

Figure 8.2: Powder diffraction of Mn_3Ga. Shown is the measured spectrum compared to the fit from a Rietveld-refinement. The spectra were excited by Mo K_α radiation. The picture shows the crystal structure. Mn atoms are drawn in yellow and orange and Ga atoms in gray. The Mn_I atoms (yellow) are located at the base and center planes, the Mn_{II} atoms (orange) are found in the inner cage drawn around the center Ga atom.

8.5 Magnetic Properties

The results of the magnetization measurements are displayed in Figure 8.4. The samples exhibit hard-magnetic behavior as is seen from the hystereses measured at 5 K as well as at room temperature. The values of the coercitive field are $H_c = 359$ kAm^{-1} and $H_c = 289$ kAm^{-1} for 5 K and 300 K, respectively. The corresponding values of the remanence are $B_r(5K) = 0.146$ T and $B_r(300K) = 0.145$ T. The resulting energy product is $E = H_c \times B_r = 52.5$ kJm^{-3} at 5 K. This value is comparable to the one of other hard-magnetic materials like Alnico 6 but at a four times higher coercitivity. The relatively low saturation magnetization, due to the ferrimagnetic order, makes the material comparable to ferrites and related materials. The energy products from a direct integration of the magnetization loops are about three times larger. The integrated values are E =163 kJm^{-3} and 140 kJm^{-3} for 5 K and 300 K, respectively.

The magnetization at an induction field of 5 T and 5 K corresponds to a magnetic moment of about 1.1 μ_B in the unit cell or in average 1/4 μ_B per atom. However, under that conditions the magnetization is still not completely saturated what may explain the lower value compared to the calculated one. The value at room temperature is only slightly lower. Additional investigations have shown that the DO_{22} structure is stable under variation of the composition. It turned out that the magnetic moment is tunable between near zero and 1 μ_B by changing the Mn to Ga ratio in the concentration range

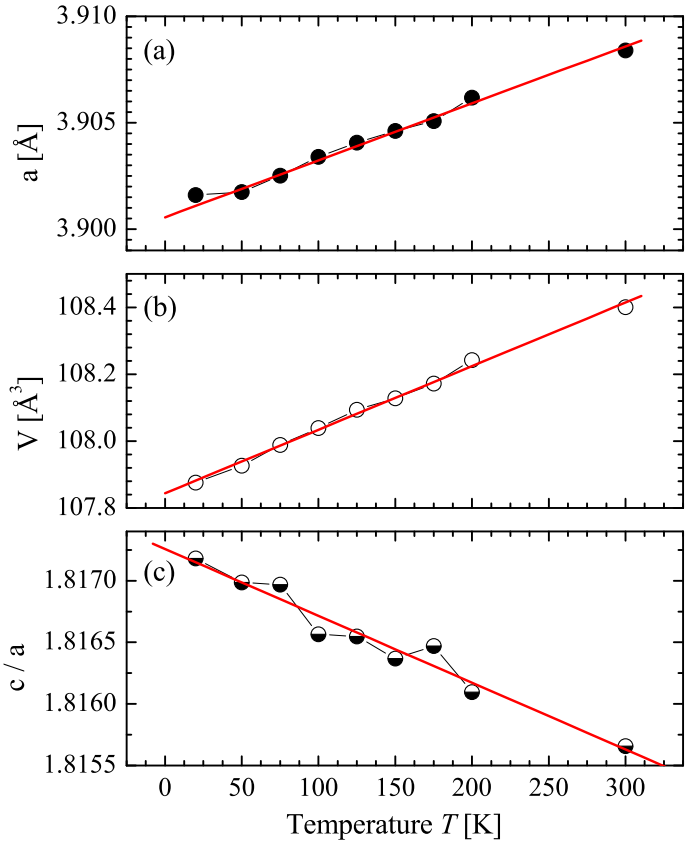

Figure 8.3: Temperature dependence of the Mn_3Ga lattice. Panels (a) and (b) show the temperature dependence of the lattice parameter a and the cell Volume V, respectively. Panel (c) shows the corresponding c/a ratio.

from $Mn_{2.85}Ga$ to Mn_3Ga.

The temperature dependence of the magnetization is shown in the inset of Figure 8.4. The measurements were performed in remanence, that means in zero field after magnetizing the sample in an induction field of $\mu_0 H = 5$T. The cause of the dramatic decrease of the magnetization at $T_S \approx 730$ K is a structural transition from the tetragonal to the hexagonal phase [155, 157]. The phase transition is easily detected using differential scanning calorimetry. The occurrence of the structural phase transition makes it impossible to determine the Curie temperature of the tetragonal phase of Mn_3Ga. The structural phase transition takes place at temperatures below the expected magnetic phase transition. Nevertheless, this should not be a problem for the design of devices using this material because it is very stable in the temperature range up to 700 K and thus well suited for applications at and above room temperature.

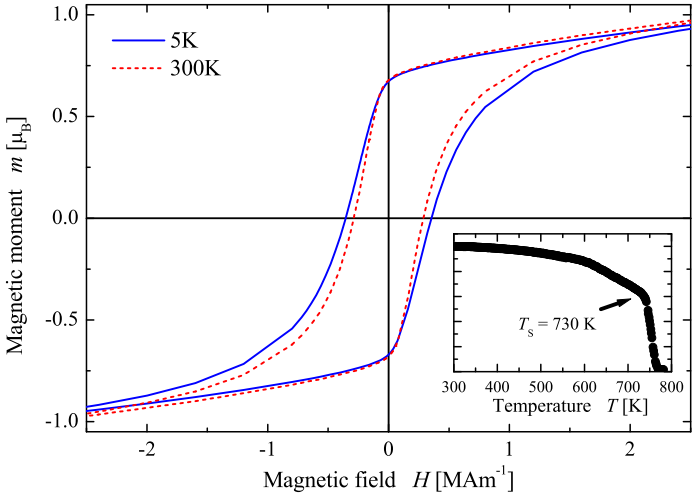

Figure 8.4: Magnetization of Mn_3Ga. Displayed are the hysteresis curves taken at $T = 5$ K and $T = 300$ K. The magnetization as a function of the temperature is shown in the inset.

8.6 Summary and Conclusion

In summary, it has been shown that the DO_{22} phase of Mn_3Ga is a suitable material for spin torque transfer applications. The material is hard magnetic with an energy product of 52.5 kJm^{-3} at 5 K. The saturation magnetization is in average about 1/4 μ_B per atom. The Curie temperature is above the decomposition temperature of about 730 K. The electronic structure calculation indicate a ground state with ferrimagnetic order and 88% spin polarization at the Fermi energy. To achieve the necessary MTJ structure one may grow thin films of Mn_3Ga epitaxially for example on $SrTiO_3(100)$ or Pd(100) substrates. Depending on the substrate, it should be possible to grow films with the magnetic easy axis in plane or perpendicular to the plane.

9 Summary and Outlook

9.1 Summary

This work emphasizes the potential of Heusler compounds in a wide range of spintronic applications. Using electronic structure calculations it is possible to design compounds for specific applications. Examples for GMR and TMR applications, for spin injection into semiconductors, and for spin torque transfer applications were shown.

Chapter 5 reported about the investigation of new half-metallic compounds where the Fermi energy is tuned in the middle of the gap to result in more stable compounds for GMR and TMR applications.

The bulk properties of the quaternary Heusler alloy $Co_2Mn_{1-x}Fe_xSi$ with the Fe concentration ranging from $x = 0$ to 1 were reported. The electronic structure was explored by means of high energy photo emission spectroscopy at about 8 keV photon energy. This ensures true bulk sensitivity of the measurements. The magnetization of the Fe doped Heusler alloys is in agreement with the values of the magnetic moments expected for a Slater-Pauling like behavior of half-metallic ferromagnets. The experimental findings were discussed on the hand of self-consistent calculations of the electronic and magnetic structure. To achieve good agreement with experiment, the calculations indicate that on-site electron-electron correlation must be taken into account, even at low Fe concentration. Overall, the results suggest that the best candidate for applications may be found at an iron concentration of about 50%.

Due to the effect that in the $Co_2Mn_{1-x}Fe_xSi$ series the transition metal carrying the localized moment is exchanged and this might lead to unexpected effects on the magnetic properties if the samples are not completely homogeneous chapter 6 reports about the optimization of the Heusler compounds for GMR and TMR applications. The structural and magnetic properties of the quaternary Heusler alloy $Co_2FeAl_{1-x}Si_x$ with varying Si concentration were reported. It was shown that the alloys exhibit the $L2_1$ structure for $x \geq 0.4$. Depending on the Si concentration x, a structural phase transition is found at temperatures between 1000 K and 1200 K. The transition temperature decreases with increasing Si content x. For $x \geq 0.4$, the magnetization of the compounds is in agreement with a Slater-Pauling like behavior and with the values obtained from ab-initio calculations. For $x \leq 0.4$ enlarged magnetic moments are found due to disorder. From the combination of experimental (better order for high Si content) and theoretical findings (robust gap at $x \approx 0.5 \pm 0.25$) it is concluded that a compound with an intermediate Si concentration close to $x = 0.5 \ldots 0.7$ would be best suited for spintronic applications, especially for GMR and TMR applications.

In chapter 7 the detailed investigation of compounds for spin injection into semiconductors was reported. It was shown that the diluted magnetic semiconductors based on CoTiSb with a very low lattice mismatch among each other are interesting materials for spintronics applications like Spin-LEDs or other spin injection devices. One could

prepare thin film devices including these materials and it should be possible to grow them epitaxially with clean and smooth interfaces. If depositing layer by layer one can use the Co-planes to merge the different materials without any interface at all.

The diluted magnetic semiconductors were prepared by substituting titanium in the semiconducting compound CoTiSb by other 3d transition elements. The structural, electronic, and magnetic properties of the pure and doped materials were investigated. It was found that substitution of up to 10% Ti by Fe, Mn, Cr, and V does not affect the crystalline structure and the lattice mismatch is less than 0.5% among each other. Self consistent calculations of the electronic structure predict some of the materials to be half-metallic ferromagnets. The Curie temperature of the Fe substituted alloy is far above room temperature (> 700 K), thus making that material a serious candidate for future electronic applications, in particular for magnetoelectronics and spintronics.

Chapter 8 refered about a detailed investigation of the theoretically predicted half-metallic completely compensated-ferrimagnet Mn_3Ga as a suitable material for spin torque transfer applications. The electronic, magnetic, and structural properties of the tetragonal DO_{22} phase of Mn_3Ga were investigated. It has been found that the material is hard magnetic with an energy product of $H_c \times B_r = 52.5$ kJm^{-3} and an average saturation magnetization of about 0.25 Bohr magnetons per atom at 5 K. The saturation magnetization indicates a ferrimagnetic order with partially compensating moments at the Mn atoms on crystallographically different sites. The Curie temperature is above 730 K where the onset of decomposition is observed. The electronic structure calculations indicate a nearly half-metallic ferrimagnetic order with 88% spin polarization at the Fermi energy.

9.2 Outlook

The two most important challenge for a further optimization of Heusler compounds for spintronic application are the correct crystallographic structure of the samples and the determination of their electronic structure to demonstrate the half metallicity.

Most of the X_2YZ Heusler compounds used for the production of TMR devices are based on $3d$ transition metals like Co for the X element and Cr, Mn, Fe, or mixtures of those for the Y element. The main group element (Z) is usually taken from the 3^{rd} row (Al, Si) or from the 4^{th} row (Ga, Ge) of the periodic system of elements. The detection of the correct structure, as a necessary prerequisite for a half-metallic character, by regular X-ray diffraction (XRD) is difficult in particular if all 3 elements in the compound are from the 4^{th} row. In that case, the scattering factors of all three elements are very similar for excitation by standard laboratory sources (for example: Cu K_α or Mo K_α).

The situation changes if one approaches with the photon energy close to the absorption edges of the constituents as then the anomalous scattering factors play an important role. The complete scattering factors of the atoms with ordinal number N are described by:

$$f_N = f_0(N, \theta, E) + (f'(N, E) + if''(N, E)), \tag{9.1}$$

where $f'(N, E)$ and $f''(N, E)$ are the real and imaginary part of the anomalous scat-

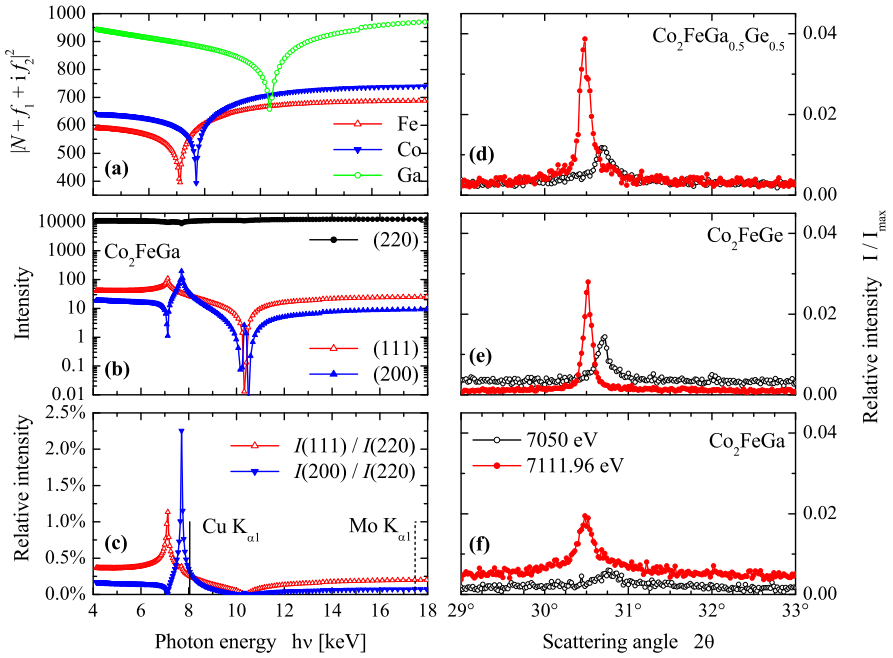

Figure 9.1: Panel (a) shows the anomalous scattering factors of Co, Fe, and Ga. Panel (b) shows the calculated anomalous XRD intensities for Co_2FeGa. The energies for excitation by typical laboratory sources are assigned by vertical lines in (c) Panels (d)-(f) show XRD measurements taken with the excitation energy of the Fe K-edge (7111.96 keV) and below that energy.

tering factor. These factors do not depend on the scattering geometry but only on the photon energy (E) and the material (N).

Figure 9.1(a) displays the calculated anomalous scattering factors of Co, Fe, and Ga. Panel (b) and (c) displays the calculated anomalous scattering intensities for Co_2FeGa. The enhancement of the (111) reflexion, being indicative for the $L2_1$ structure, at energies close to the Fe K-edge is clearly visible.

The associated anomalous XRD experiments have been performed at the XPD beamline of the LNLS (Brazilian Synchrotron Light Laboratory). The results for Co_2FeGa, Co_2FeGe, and $Co_2FeGa_{0.5}Ge_{0.5}$ are displayed in panels (d)-(f) of Figure 9.1. For a better comparision the measurements were taken with the excitation energy of the Fe K-edge (7111.96 eV) and an energy below this edge (7050 eV). As predicted from the theory a clear enhancement of the (111) reflexion at energies close to the Fe K-edge is observed.

From this very recent results it is expected that anomalous XRD may also help for a better understanding of the structure of thin films in order to improve the quality of TMR - junctions.

On the other hand - as show in the previous chapters - hard X-ray photo emission

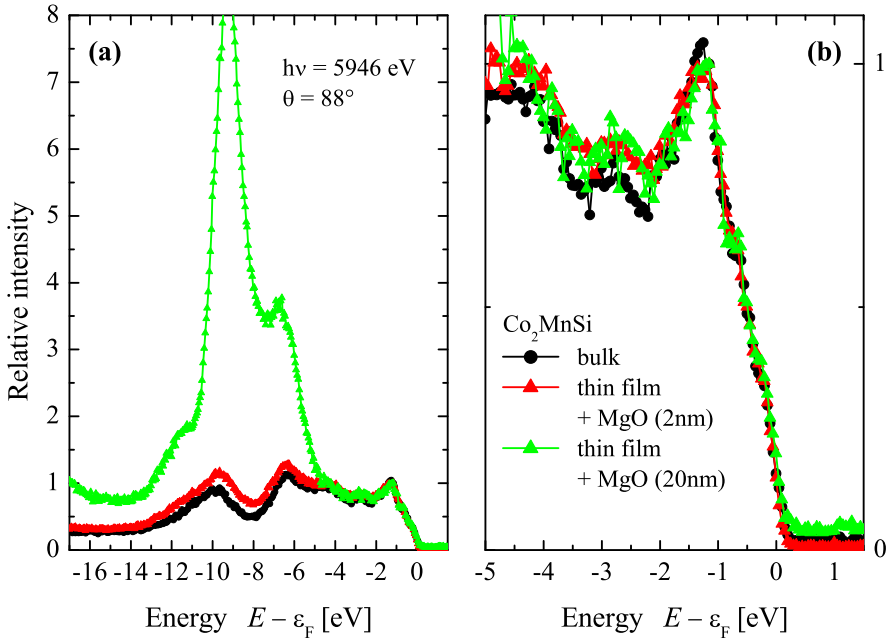

Figure 9.2: High energy valence band spectra of Co_2MnSi. Shown is the comparision between Co_2MnSi thin films capped with 2 nm and 20 nm MgO and the bulk sample. Panel (a) shows the complete spectra while panel (b) shows an enlarged view of the area around the Fermi energy.

spectroscopy (HAXPES) with high bulk sensitivity is the best methods to study bulk properties of new materials and devices due to the large mean free path of the photoelectrons compared to conventional photoemission spectroscopy.

Very recent results measured at the NIMS (Natinal Institue for Material Science) beamline BL 15 XU at SPring8 in Japan show the high bulk sensitivity and a huge mean free path of the photoelectrons from Co_2MnSi trough a MgO barrier.

We investigated the valence band of Co_2MnSi thin films capped with 2 nm and 20 nm MgO and compared them with the the bulk sample. Figure 9.2 displays the results from the HAXPES measurements. Panel (a) shows the complete spectra while panel (b) shows an enlarged view of the area around the Fermi energy and it is obvious and certainly surprising that it is possible to investigate the valence band of Co_2MnSi through a 20 nm thick layer of MgO. Moreover the observed valence band spectra is complete identical around the Fermi energy compared to the one measured from the bulk sample (see Figure 9.2 (b)). And only this electrons near the Fermi energy are important for the behavior and the properties of the devices.

However, for magnetic materials such as spintronics devices the measurement of the spin and charge is necessary for fully understanding of these materials. Therefore it is

necessary to develop spin polarized high resolution HAXPES.

With the spin dependent measurement one can investigate the spin diffusion length of the materials depending on the barrier and spacer layer material and thickness. The observation if and how the spin polarisation of the bottom electrode is retained trough the MTJs and GMR devices will be possible with this technique.

In summary, this means that spin polarized high resolution HAXPES is a powerful and necessary tool to investigate different materials for tunneling barriers and spacer layers to optimize the structure, configuration and composition of the MTJs and the GMR devices to achieve sophisticated properties and results.

Bibliography

[1] I. Zutic, J. Fabian, and S. Das Sarma. *Rev. Mod. Phys.*, 76:323, 2004.

[2] P. Sharma. *Science*, 307:513, 2005.

[3] R. A. de Groot, F. M. Müller, P. G. van Engen, and K. H. J. Buschow. *Phys. Rev. Lett.*, 50:2024, 1983.

[4] W. Thomson. *Proc. R. Soc. London*, A8:546, 1857.

[5] G. Binasch, P. Grünberg, F. Saurenbach, and W. Zinn. *Phys. Rev. B*, 39:4828, 1989.

[6] M. N. Baibich, J. M. Brote, A. Fert, N. Nyugen Van Dau, F. Petroff, P. Eitenne, G. Creuzet, A. Friederich, and J. Chazelas. *Phys. Rev. Lett.*, 61:2472, 1988.

[7] P. Ball. *Nature*, 404:918–920, 2000.

[8] R. von Helmolt, J. Wecker, B. Holzapfel, L. Schultz, and K. Samwer. *Phys. Rev. Lett.*, 71:2331, 1993.

[9] S. Jin, T. H. Tiefel, M. McCormack, R. A. Fastnacht, R. Ramesh, and L. H. Chen. *Science*, 264:413, 1994.

[10] C. N. R. Rao, A.K. Cheetham, and R. Mahesh. *Chem Mater*, 8:2421, 1996.

[11] J. S. Moodera, J. Nassar, and G. Mathon. *Annu. Rev. Mater. Sci.*, 29:381, 1999.

[12] P. M. Tedrow and R. Meservey. *Phys. Rev. B*, 7:318, 1973.

[13] M. Jullire. *Phys. Lett*, 54A:225, 1975.

[14] S. Maekawa and U. Gäfvert. *IEEE Trans. Magn.*, 18:707, 1982.

[15] J. S. Moodera, L.R. Kinder, T.M. Wong, and R. Meservey. *Phys. Rev. Lett.*, 74:3272, 1995.

[16] T. Miyazaki and N. Tezuka. *J. Magn. Magn. Mater.*, 139:L231, 1995.

[17] M. Bowen, M. Bibes, A. Barthelemy, J.-P. Contour, A. Anane, Y. Lemaitre, and A. Fert. *Applied Physics Letters*, 82(2):233–235, 2003.

[18] S.S. P. Parkin, C.Kaiser, A.Panchula, P.M. Rice, B.Hughes, M.Samant, and S.-H. Yang. *Nature Materials*, 3:862, 2004.

[19] S.Yuasa, T.Nagahama, A.Fukushima, Y.Suzuki, and K.Ando. *Nature Materials*, 3:868, 2004.

[20] S.Yuasa, A.Fukushima, T.Nagahama, K.Ando, and Y. Suzuki. *Jpn. J. Appl. Phys.*, 43:L588, 2004.

[21] J. M. D. Coey, M. Venkatesan, and M. A. Bari. Half-Metallic Ferromagnets. In C. Berthier, L. P. Levy, and G. Martinez, editors, *Lecture Notes in Physics*, volume 595, pages 377 – 396. Springer-Verlag, Heidelberg, 2002.

[22] K.-I. Kobayashi, T. Kimura, H. Sawada, K. Terakura, and Y. Tokura. *Nature*, 395:677, 1998.

[23] C. Felser and R. Seshadri. *International Journal of Inorganic Materials*, 2:677, 2000.

[24] T. Block, C. Felser, G. Jakob, J. Ensling, B. Mühling, P. Gütlich, V. Beaumont, F. Studer, and R. J. Cava. *J. Solid State Chem.*, 176:646, 2003.

[25] T. Block, S. Wurmehl, J. Windeln, and C. Felser. *Appl. Phys. Lett.*, page accepted, 2006.

[26] A. E. Berkowitz, J. R. Mitchell, M. J. Carey, A. P. Young, S. Zhang, F. E. Spada, F. T. Parker, A. Hutten, and G. Thomas. *Phys. Rev. Lett.*, 68:3745, 1992.

[27] V.A. Ivanov, T.G. Ivanov, V.M. Aminov Novotortsev, and V. T. Kalinnikov. *Russian Chemical Bulletin, International Edition*, 53(11):2357–2405, 2004.

[28] H. Munekata, H. Ohno, S. von Molnar, A.Segmller, L. L. Chang, and L. Esaki. *Phys. Rev. Lett.*, 63:1849, 1989.

[29] J. M. Kikkawa, I. P. Smorchkova, N. Samarth, and D. D. Awschalom. *Science*, 277:1284, 1997.

[30] B.T. Jonker, S.C. Erwin, A.Petrou, and A.G.Petukhov. *MRS Bulletin*, October 2003:740, 2003.

[31] H. Ohno. *Science*, 281:951, 1998.

[32] H. Ohno, D. Chiba, F. Matsukura, T. Omiya, E. Abe, T. Dietl, Y. Ohno, and K. Ohtani. *Nature*, 408:944, 2000.

[33] J. A. Gupta, R. Knobel, N. Samarth, and D. D. Awschalom. *Science*, 292:2458, 2001.

[34] I. Malajovich, J. J. Berry, N. Samarth, and D. D. Awschalom. *Nature*, 411:770, 2001.

[35] J. C. Slater. *Phys. Rev.*, 49:537, 1936.

[36] L. Pauling. *Phys. Rev.*, 54:899, 1938.

[37] J. Kübler. *Theory of Itinerant Electron Magnetism*. Oxford University Press, Oxford, New York, 2000.

[38] A. P. Malozemoff, A. R. Williams, and V. L. Moruzzi. *Phys. Rev. B*, 29:1620, 1984.

[39] S. Wurmehl, G. H. Fecher, H. C. Kandpal, V. Ksenofontov, C. Felser, H.-J. Lin, and J. Morais. *Phys. Rev. B*, 72:184434, 2005.

[40] M. Lezaic, Ph. Mavropoulos, J. Enkovaara, G. Bihlmayer, and S. Blügel. *Phys. Rev. Lett.*, 97:026404, 2006.

[41] R. Skomski and P. A. Dowben. *Europhys. Lett.*, 58(4):544, 2002.

[42] K. Ghosh, C. J. Lobb, R. L. Greene, S. G. Karabashev, D. A. Shulyatev, A. A. Arsenov, and Y. Mukovskii. *Phys. Rev. Lett.*, 81:4740, 1998.

[43] R. A. de Groot. *Phys. Rev. Lett.*, 50:2024, 1983.

[44] J. Kübler. *Physica B*, 127:257, 1984.

[45] D. Jung, H. J. Koo, and M. H. Whangbo. *J. Molec. Struct. Theochem.*, 527:113–119, 2000.

[46] J. Pierre, R. V. Skolozdra, Y. K. Gorelenko, and M. A. Kouacou. *J. Magn. Magn. Mater.*, 134:95, 1994.

[47] J. Tobola, J. Pierre, S. Kaprzyk, R. V. Skolozdra, and M. A. Kouacou. *J. Phys. Condens. Matter*, 10:1013, 1998.

[48] H. Ohno, A. Shen, F. Matsukura, A. Oiwa, A. Endo, S. Katsumoto, and Y. Iye. *Appl. Phys. Lett.*, 69:363, 1996.

[49] K. W. Edmonds, K. Y. Wang, R. P. Campion, A. C. Neumann, N. R. S. Farley, B. L. Gallagher, and C. T. Foxon. *Appl. Phys. Lett.*, 81:4991, 2002.

[50] A. H. MacDonald, P. Schiffer, and N. Samarth. *Nature Materials*, 4:195, 2005.

[51] M. L. Reed, N. A. El-Masry, H. H. Stadelmaier, M. K. Ritums, M. J. Reed, C. A. Parker, J. C. Roberts, and S. M. Bedair. *Appl. Phys. Lett.*, 79:3473, 2001.

[52] N. H. Hong, J. Sakai, and A. Hassini. *Appl. Phys. Lett.*, 84:2602, 2004.

[53] R.-T. Huang, C.-F. Hsu, J.-J. Kai, and F.-R. Chen. *Appl. Phys. Lett.*, 87:202507, 2005.

[54] X. Wang, J. B. Xu, N. Ke, J. Yu, J. Wang, Q. Li, H. C. Ong, and R. Zhang. *Appl. Phys. Lett.*, 88:223108, 2006.

[55] J. Kübler, A. R. Williams, and C. B. Sommers. *Phys. Rev. B*, 28:1745, 1983.

[56] H. C. Kandpal, C. Felser, and R. Seshadri. *J. Phys. D: Appl. Phys.*, 39:776, 2006.

[57] Fr. Heusler. *Verh. Dtsch. Phys. Ges.*, 12:219, 1903.

[58] Fr. Heusler, W. Starck, and E. Haupt. *Verh. d. DPG*, 5:220, 1903.

[59] A. J. Bradley and J. W. Rodgers. *Proc. Royal Soc. A*, 144:340 – 359, 1934.

[60] G. H. Fecher, S. Wurmehl, H. C. Kandpal, G. Schönhense, and C. Felser. *J.Appl.Phys.*, 99:08J106, 2006.

[61] I. Galanakis. *J. Phys.: Condens. Matter*, 14:6329 – 6340, 2002.

[62] M. Penicaud, B. Silberchiot, C.B. Sommers, and J. Kübler. *J. Magn. Magn. Mater.*, 103:212, 1992.

[63] B. Nadgorny, I. I. Mazin, M. Osofsky, R. J. Soulen Jr., P. Broussard, R. M. Stroud, D. J. Singh, V. G. Harris, A. Arsenov, and Y. Mukovskii. *Phys. Rev. B*, page 18 4433, 2001.

[64] D. J. Singh. *Phys. Rev. B*, 55:313, 1997.

[65] P. Blaha, K. Schwarz, G. K. H. Madsen, D. Kvasnicka, and J. Luitz. *WIEN2k, An Augmented Plane Wave + Local Orbitals Program for Calculating Crystal Properties*. Karlheinz Schwarz, Techn. Universitaet Wien, Wien, Austria, 2001.

[66] J. P Perdew, K. Burke, and M. Ernzerhof. *Phys. Rev. Lett*, 77:3865, 1996.

[67] H. Ebert. Electronic structure and physical properties of solids - fully relativistic band structure calculations for magnetic solids - formalism and application. In H. Dreysse, editor, *Lecture Notes in Physics*, volume 535, pages 191–246. Springer Verlag, 1999.

[68] H. C. Kandpal, G. H. Fecher, and C. Felser. *Phys. Rev. B*, 73:094422, 2006.

[69] V. I. Anisimov, F. Aryasetiawan, and A. I. Lichtenstein. *J. Phys. Condens. Matter*, 9:767, 1997.

[70] L. Wilk and S. H. Vosko. *Phys. Rev. A*, 15:1839, 1977.

[71] S. H. Vosko, L. Wilk, and M. Nusair. *Can. J. Phys.*, 58:1200, 1980.

[72] S. H. Vosko and L. Wilk. *Phys. Rev. B*, 22:3812, 1980.

[73] J. P. Perdew, J. A. Chevary, S. H. Vosko, K. A. Jackson, M. R. Pederson, D. J. Singh, and C. Fiolhais. *Phys. Rev. B*, 46:6671, 1992.

[74] F. F. Ferreira, Eduardo Granado, Wilson Carvalho Jr., Stefan W. Kycia, Daniele Bruno, and Roosevelt Droppa Jr. *J. Synchrotron Rad.*, 13:46–53, 2006.

[75] G. H. Fecher, A. Gloskowskii, K. Kroth, J. Barth, B.Balke, C.Felser, F. Schäfers, M.Mertin, W. Eberhardt, S. Mähl, and O. Schaff. *J. Electron Spectrosc. Relat. Phenom.*, 156-158:97, 2007.

[76] F. Senf, F. Eggenstein, U. Flechsig, R. Follath, S. Hartlaub, H. Lammert, T. Noll, J.S. Schmidt, G. Reichardt, O. Schwarzkopf, M. Weiss, T. Zeschke, and W. Gudat. *Nuclear Instruments and Methods in Physics Research A*, 467 - 468:474 – 478, 2001.

[77] C. T. Chen. *Nucl. Instrum. Methods Phys. Res. Sect. A*, 256:595, 1987.

[78] C. T. Chen and F. Sette. *Rev. Sci. Instrum.*, 60:1616, 1989.

[79] M. Newville. *J. Synchrotron Rad.*, 8:322, 2001.

[80] S. I. Zabinsky, J. J. Rehr, A. Ankudinov, R. C. Albers, and M. J. Eller. *Phys. Rev. B*, 52:2995, 1995.

[81] I. Galanakis, P. H. Dederichs, and N. Papanikolaou. *Phys. Rev. B*, 66:174429, 2002.

[82] S. Picozzi, A. Continenza, and A. J. Freeman. *Phys. Rev. B*, 66:094421, 2002.

[83] G. H. Fecher, H. C. Kandpal, S. Wurmehl, and C. Felser. *J. Appl. Phys.*, 99:08J106, 2006.

[84] S. Picozzi, A. Continenza, and A. J. Freeman. *Phys. Rev. B*, 69:094423, 2004.

[85] S. Fuji, S. Sugimura, S. Ishida, and S. Asano. *J. Phys.: Condens. Matter*, 2:8583 – 8589, 1990.

[86] P. J. Brown, K.-U. Neumann, P. J. Webster, and K. R. A. Ziebeck. *J. Phys.: Condens. Matter*, 12:1827 – 1835, 2000.

[87] M. P. Raphael, B. Ravel, Q. Huang, M. A. Willard, S. F. Cheng, B. N. Das, R. M. Stroud, K. M. Bussmann, J. H. Claassen, and V. G. Harris. *Phys. Rev. B*, 66:104429, 2002.

[88] U. Geiersbach, A. Bergmann, and K. Westerholt. *J. Magn. Magn. Mater.*, 240:546 – 549, 2002.

[89] S. Kämmerer, S. Heitmann, D. Meyners, D. Sudfeld, A. Thomas, A. Hütten, and G. Reiss. *J. Appl. Phys.*, 93:7945, 2003.

[90] L. J. Singh, Z. H. Barber, Y. Miyoshi, Y. Bugoslavsky, W. R. Branford, and L. F. Cohen. *Appl. Phys. Lett.*, 84:2367, 2004.

[91] W. H. Wang, M. Przybylski, W. Kuch, L. I. Chelaru, J. Wang, F. Lu, J. Barthel, H. L. Meyerheim, and J. Kirschner. *Phys. Rev. B*, 71:144416, 2005.

[92] W. H. Wang, M. Przybylskia, W. Kuch, L. I. Chelaru, J. Wang, Y. F. Lu, J. Barthel, and J. Kirschner. *J. Magn. Magn. Mat.*, 286:336 – 339, 2005.

[93] J. Schmalhorst, S. Kammerer, M. Sacher, G. Reiss, A. Hütten, and A. Scholl. *Phys. Rev. B*, 70:024426, 2004.

[94] J Schmalhorst, S Kammerer, G Reiss, and A Hütten. *Appl. Phys. Lett.*, 86:052501, 2005.

[95] P LeClair, H. J. M. Swagten, J. T. Kohlhepp, and W. J. M. de Jonge. *Appl. Phys. Lett.*, 76:3783–3785, 2000.

[96] S. Tanuma, C. J. Powell, and D. R. Penn. *: Surf. Interf. Anal.*, 21:165, 1993.

[97] W. Meisel. *Hyperfine Interact.*, 45:73 – 90, 1989.

[98] K. Kobayashi, M. Yabashi, Y. Takata, T. Tokushima, S. Shin, K. Tamasaku, D. Miwa, T. Ishikawa, H. Nohira, T. Hattori, Y. Sugita, O. Nakatsuka, A. Sakai, and S. Zaima. *Appl. Phys. Lett.*, 83:1005, 2003.

[99] A. Sekiyama and S. Suga. *J. Electron Spectrosc. Relat. Phenom.*, 137-140:681 – 685, 2004.

[100] S. Thiess, C. Kunz, B. C. C. Cowie, T.-L. Lee, M. Reniera, and J. Zegenhagen. *Solid State Comm.*, 132:589, 2004.

[101] K. Kobayashi. *Nucl. Instrum. Methods Phys. Res., Sect. A*, 547:98, 2005.

[102] G. Panaccione, G. Cautero, M. Cautero, A. Fondacaro, M. Grioni, P. Lacovig, G. Monaco, F. Offi, G. Paolicelli, M. Sacchi, N. Stojic, G. Stefani, R. Tommasini, and P. Torelli. *J. Phys.: Condens. Matter*, 17:2671, 2005.

[103] P. Torelli, M. Sacchi, G. Cautero, M. Cautero, B. Krastanov, P. Lacovig, P. Pittana, R. Sergo, R. Tommasini, A. Fondacaro, F. Offi, G. Paolicelli, G. Stefani, M. Grioni, R. Verbeni, G. Monaco, and G. Panaccione. *Rev. Sci. Instrum.*, 76:023909, 2005.

[104] S. Wurmehl, G. H. Fecher, H. C. Kandpal, V. Ksenofontov, C. Felser, and H.-J. Lin. *Appl. Phys. Lett.*, 88:032503, 2006.

[105] S. Wurmehl, G. H. Fecher, K. Kroth, F. Kronast, H. A. Dürr, Y. Takeda, Y. Saitoh, K. Kobayashi, H.-J. Lin, G. Schönhense, and C. Felser. *J. Phys. D: Appl. Phys.*, 39:803 – 815, 2006.

[106] Y. Miura, K. Nagao, and M. Shirai. *Phys. Rev. B*, 69:144413, 2004.

[107] K. Kobayashi, R. Y. Umetsu, R. Kainuma, K. Ishida, T. Oyamada, A. Fujita, and K. Fukamichi. *Appl. Phys. Lett.*, 85:4684, 2004.

[108] G. H. Fecher, H. C. Kandpal, S. Wurmehl, J. Morais, H.-J. Lin, H.-J. Elmers, G. Schönhense, and C. Felser. *J. Phys. Condens. Matter*, 17:7237 – 7252, 2005.

[109] V. I. Anisimov and O. Gunnarson. *Phys. Rev. B*, 43:7570, 1991.

[110] G. K. H. Madsen and P. Novak. *Europhys. Lett.*, 69:777 – 783, 2005.

[111] V. I. Anisimov, J. Zaanen, and O. K. Andersen. *Phys. Rev. B*, 44:943, 1991.

[112] T. Bandyopadhyay and D. D. Sarma. *Phys. Rev. B*, 39:3517, 1989.

[113] S. Y. Savrasov. *Phys. Rev. B*, 54:16470, 1996.

[114] V. I. Anisimov, I. V. Solovyev, M. A. Korontin, M. T. Czyzyk, and G. A. Sawatzky. *Phys. Rev. B*, 48:16929, 1993.

[115] R. D. Cowan. *The Theory of Atomic Structure and Spectra*. University of California Press, Berkeley and Los Angeles, 1981.

[116] G. E. Bacon and J. S. Plant. *J. Phys. F: Met. Phys.*, 1:524 – 532, 1971.

[117] V. Niculescu, T. J. Burch, K. Rai, and J. I. Budnick. *J. Magn. Magn. Mater.*, 5:60, 1977.

[118] V. Niculescu, J. I. Budnick, W. A. Hines, K. Rajt, S. Pickart, and S. Skalski. *Phys. Rev. B*, 19:452, 1979.

[119] K. Kobayashi, R. Y. Umetsu, A. Fujita, K. Oikawa, R. Kainuma, K. Fukamichi, and K. Ishida. *J. All. Comp.*, 399:60 – 63, 2005.

[120] P. J. Webster. *J. Phys. Chem. Solids*, 32:1221 – 1231, 1971.

[121] M. Kallmayer, H. J. Elmers, B. Balke, S. Wurmehl, F. Emmerling, G. H. Fecher, and C. Felser. *J. Phys. D: Appl. Phys.*, 39:786, 2006.

[122] C. Felser, G. H. Fecher, and B. Balke. *Angew. Chem. Int. Ed.*, 46:668 – 699, 2007.

[123] H. C. Kandpal, G. H. Fecher, and C. Felser. *J. Phys. D: Appl. Phys.*, 40:1507, 2007.

[124] H.-J. Elmers, G. H. Fecher, D. Valdaitsev, S. A. Nepijko, A. Gloskovskii, G. Jakob, G. Schönhense, S. Wurmehl, T. Block, C. Felser, P.-C. Hsu, W.-L. Tsai, and S. Cramm. *Phys. Rev. B*, 67:104412, 2003.

[125] T. Marukame, T. Ishikawa, S. Hakamata, K.-i. Matsuda, T. Uemura, and M. Yamamoto. *Appl. Phys. Lett.*, 90:012508, 2007.

[126] B. Balke, G. H. Fecher, H. C. Kandpal, and C. Felser. *submitted to Phys. Rev. B*, 2006.

[127] K. Inomata, S. Okamura, A. Miyazaki, M. Kikuchi, N. Tezuka, M. Wojcik, and E. Jedryka. *J Phys. D: Appl. Phys.*, 39:816, 2006.

[128] M. Oogane, Y. Sakuraba, J. Nakata, H. Kubota, Y. Ando, A. Sakuma, and T. Miyazaki. *J Phys. D: Appl. Phys.*, 39:834, 2006.

[129] D. Ebke, J. Schmalhorst, N.-N. Liu, A. Thomas, G. Reiss, and A. Hütten. *Appl. Phys. Lett.*, 89:162506, 2006.

[130] N. Tezuka, N. Ikeda, A. Miyazaki, S. Sugimoto, M. Kikuchi, and K. Inomata. *Appl. Phys. Lett.*, 89:112514, 2006.

[131] N. Tezuka, N. Ikeda, S. Sugimoto, and K. Inomata. *Appl. Phys. Lett.*, 89, 2006.

[132] G. H. Fecher and C. Felser. *J Phys. D: Appl. Phys.*, 40:1582, 2007.

[133] H. Ebert. *The Munich SPR-KKR package, Version 3.6 , http://olymp.cup.uni-muenchen.de/ak/ebert/SPRKKR.* 2005.

[134] J. Tobola and J. Pierre. *J. Alloys Compd.*, 296:243, 2000.

[135] K. Kroth, B. Balke, G. H. Fecher, V. Ksenofontov, C. Felser, and H.-J. Lin. *Appl. Phys. Lett.*, 89:202509, 2006.

[136] Y. Stadnyk, V.A. Romaka, M. Shelyapina, Y. Gorelenko, L. Romaka, D. Furchart, A. Tkachuk, and V. Chekurin. *J. Alloys Compd.*, 421:19–23, 2006.

[137] A. Sekiyama, T. Iwasaki, K. Matsuda, Y. Saitoh, Y. Onuki, and S. Suga. *Nature*, 403:396, 2000.

[138] F. Salvat and R. Mayol. *Comp. Phys. Commun.*, 62:65, 1991.

[139] F. Salvat and R. Mayol. *Comp. Phys. Commun.*, 74:358, 1993.

[140] J. M. Rabaey. *CRA Conference*, 2002.

[141] L. Berger. *Phys. Rev. B*, 54:9353, 1996.

[142] J. C. Slonczewski. *J. Magn. Magn. Mater.*, 159:L1, 1996.

[143] M. Tsoi, A. G. M. Jansen, J. Bass, W.-C. Chiang, M. Seck, V. Tsoi, and P. Wyder. *Phys. Rev. Lett.*, 80:4281, 1998.

[144] E. B. Myers, D. C. Ralph, J. A. Katine, R. N. Louie, and R. A. Buhrman. *Science*, 285:867, 1999.

[145] K. Bussmann, G. A. Prinz, S.-F. Cheng, and D. Wang. *Appl. Phys. Lett.*, 75:2476, 1999.

[146] J. A. Katine, F. J. Albert, R. A. Buhrman, E. B. Myers, and D. C. Ralph. *Phys. Rev. Lett.*, 84:3149, 2000.

[147] J. Grollier, V. Cros, A. Hamzic, J. M. George, H. Jaffres, A. Fert, G. Faini, J. Ben Youssef, and H. Le Gall. *Appl. Phys. Lett.*, 78:3663, 2001.

[148] Y. Huai, F. Albert, P. Nguyen, and T. Valet. *Appl. Phys. Lett.*, 84:3118, 2004.

[149] G. D. Fuchs, N. C. Emley, I. N. Krivorotov, P. M. Braganca, E. M. Ryan, S. I. Kiselev, J. C. Sankey, D. C. Ralph, R. A. Buhrman, and J. A. Katine. *Appl. Phys. Lett.*, 85:1205, 2004.

[150] Z. Diao, D. Apalkov, M. Pakala, Y. Ding, A. Panchula, and Y. Huai. *Appl. Phys. Lett.*, 87:232502, 2005.

[151] Y. Huai, M. Pakala, Z. Diao, and Y. Ding. *Appl. Phys. Lett.*, 87:222510, 2005.

[152] T. Ochiai, Y. Jiang, A. Hirohata, N. Tezuka, S. Sugimoto, and K. Inomata. *Appl. Phys. Lett.*, 86:242506, 2005.

[153] H. Y. T. Nguyen, H. Yi, S.-J. Joo, K.-H. Shina, K.-J. Lee, and B. Dieny. *Appl. Phys. Lett.*, 89:094103, 2006.

[154] C. Heide, P. E. Zilberman, and R. J. Elliott. *Phys. Rev. B*, 63:064424, 2002.

[155] H.-G. Meißner and K. Schubert. *Zeitschrift für Metallkunde*, 56:523, 1965.

[156] S. Wurmehl, H. C. Kandpal, G. H. Fecher, and C. Felser. *J. Phys.: Condens. Matter*, 18:6171 – 6181, 2006.

[157] E. Kren and G. Kadar. *Solid State Comm.*, 8:1653 – 1655, 1970.

[158] H. Niida, T. Hori, H. Onodera, Y. Yamaguchi, and Y. Nakagawa. *J. Appl. Phys.*, 79:5946, 1996.

[159] J. Kübler. *J. Phys.: Condens. Matter*, 18:9795 – 9807, 2006.